Electric Discharges in Laser Produced Plasmas

Enrique Sterling

A Thesis presented for the degree of
Doctor of Philosophy

School of Physics
Trinity College Dublin
Ireland
March 2010

soli Deo gloria

Declaration

The work in this thesis is based on research carried out at the University of Dublin, Trinity College, Ireland. No part of this thesis has been submitted elsewhere for any other degree or qualification and it all my own work unless referenced to the contrary in the text.

I agree to allow the library of Trinity College Dublin to copy or lend a section or this entire thesis on request.

Electric Discharges in Laser Produced Plasmas

Enrique Sterling

Submitted for the degree of Doctor of Philosophy
March 2010

Summary

This thesis describes the results of an investigation of the effects of a medium voltage (0.1-1 kV), low-inductance discharge in a laser produced plasma. Discharging was done in vacuum using coaxial discharge cells of different geometries.

The expansion dynamics of the plasma were analysed using various experimental techniques, such as Langmuir ion probes, time-resolved imaging, time- and space-resolved spectroscopy, ion energy spectrum analysis and thin film deposition. A novel technique was used to manipulate ion probe signals, in order to infer the ion density profiles at different times after ablation.

This work is separated into two parts: in the first, a laser produced plasma is formed inside the charged coaxial cell, and as the plume expands, electric current begins to flow within the plasma. The effects of this current on the expansion dynamics, ion energy, electron temperature and deposition rate were studied using two discharge cell geometries: open-ended and conical.

The second part of this work consisted of driving an electric discharge through a thin plasma column in order to obtain a Z-pinch. An aperture was used to select a portion of the ablation plume in order to control parameters important for pinching (e.g. column diameter and ion line density). Results such as the time to pinch, the final radius after compression and ion line density are compared with current Z-pinch models.

Acknowledgements

I am indebted to my supervisor, James Lunney, for his great support, for the constant flow of ideas and invaluable suggestions, and especially for giving me the opportunity to be here.

I would like to thank my fellow group members Tony Donnelly, Clelia Pagano and Inam Mirza for their friendship, and for many a discussion on plasmas, physics, politics and life.

Thanks to Naoise Mac Giollabhui and Brendan Doggett for help in proofreading this thesis and discussion of results.

To all the staff members from the School of Physics for their constant support: Nigel Carroll, Ken Concannon and Joe McCauley; John Kelly, Gillian O'Neill and James 'Jemer' Kavanagh from the front office; Mick Reilly, Pat Murphy, Gordon O'Brien and Dave O'Mahony from the workshop; Una Dowling, Rebecca Owens and Jeanette Cummins from the School of Physics office. Thank you all!

I am very grateful to Aodh O'Connor, Oran Morris and Emma Sokell from UCD for all their help during my time there.

To Mary Anna, the love of my life, thank you for standing by me through thick and thin. Your constant support, encouragement, patience and love have made me a better man.

Last but not least, I am grateful to God; my creator, my father and my friend.

Contents

List of Figures

List of Tables

Introduction

The present work investigates the effects of a fast electric DC discharge of moderate current through a laser produced plasma. Discharges were tested using various coaxial configurations, using the plasma produced by laser ablation as an initial source. Research involving laser plasmas and vacuum arc discharges has been reported for many years, where lasers are used to trigger high-voltage vacuum arcs for a myriad of applications such as X-ray generation, deposition of thin films, metallurgical coatings and electrical switching [1] [2]. In these cases the laser plasma is often used for precise triggering of the discharge, and in some instances, also gives some control of the initial plasma conditions. Of these different vacuum arc experiments, the generation of X-rays is of particular interest, since it has been shown that this radiation is produced by a Z-pinch, whereby the azimuthal self-magnetic field induced by current flow collapses the plasma to a small radius. When very high rates of current are present $> 10^{10}$ $[A\,s^{-1}]$, this compression will accelerate the particles in the column inwards producing a radial implosion, where the plasma reaches densities of 10^{21} $[cm^{-3}]$ at the center. As the plasma thermalises, it reaches temperatures of 100-1000 eV followed by radial emission of K-shell radiation (X-rays), electrons and ions [3] [4].

The above makes Z-pinches a viable source of ultraviolet (UV) radiation, which is currently in high demand for photo-lithography in computer processor development. Semiconductor chip manufacturers are constantly trying to advance Moore's Law, which is the *per annum* doubling in the number of transistors on a single die chip. Currently, existing chip production is able to print 45 nm features using an ArF

laser source, emitting in the deep-UV (DUV) at λ =193 nm, and using an immersion technique to increase resolution. The next step in the development of smaller feature sizes is said to lie in the use of extreme-UV (EUV) light sources; the wavelength of choice being λ =13.5 nm due to the Bragg reflection optics available. Currently, EUV radiation generation comes from two sources: high-intensity laser produced plasmas [5] and Z-pinches in high-current arc discharges [6]. Therefore, since both laser plasmas and Z-pinches are potential sources of EUV radiation, a combination of both is of great interest.

Among the aims of this work was the optimisation of a Z-pinch. This involved the production of an initial plasma plume by laser ablation, which was characterized to determine the plasma ion density, temperature and dimensions. The plasma was then put through an aperture leading into a discharge cell, where the inter-electrode gap, rate of current rise and energy delivered were also controlled. This, therefore, allowed for a highly controlled experiment that led to a better understanding of the pinch dynamics.

A second objective was the modification of laser plasma expansion dynamics, also using a fast electric discharge. This experiment was of interest due to preliminary testing using Langmuir probes, which showed an increased ion flux during discharging. It was thought that this configuration would help improve or modify thin film deposition, and therefore, different designs of discharge cell were tested.

Three coaxial geometries were tested in this work.

1. Open cylindrical collar, whereby the laser plasma is produced within a central electrode and allowed to expand freely out the open end. Increased ionic emission showed promising results for plume expansion control.

2. Conical collar, a variation of the open collar where the laser plasma was also produced within the cell, was used to concentrate the laser plasma into a small radius at the same time the discharge was triggered. This experiment also showed potential for plasma plume manipulation.

3. Collimation experiment, where an aperture was placed in the path of the laser plasma, thus controlling the diameter of the plasma going into the discharge cell. This experiment was designed to study the potential for Z-pinch generation.

The concept of coaxial discharging, as well as discharging through a laser plasma are not new, however, the present experiments avail of novel techniques, especially in the controlled observation of plasma pinching in the collimation experiment. Another novel technique is the use of self-similar transforms applied to Langmuir probe signals. These transforms allowed the estimation of ion density profiles as a function of time and distance at positions other than that of the ion probe.

Parts of this work were presented in conferences with peer-reviewed proceedings (Conference on Laser Ablation (COLA) 2007 [7] and High Power Laser Ablation Conference (HPLA) 2010), additionally, two papers are currently being prepared for submission to international journals.

This work is divided into 6 chapters. In *Chapter One*, the theoretical framework is established to facilitate the physical understanding of the various experiments, as well as the techniques involved in the data analysis. *Chapter Two* describes the various types of equipment used in the experiments, it explains the experimental techniques and also contains important notes on data analysis and instrument calibration. *Chapters Three, Four and Five* explain the results obtained for each coaxial geometry studied; some concluding remarks are found at the end of each chapter. Finally, *Chapter Six* gives the main conclusions and discusses the steps needed to continue where this work left off.

Chapter 1

Theory

1.1 Laser Ablation

Laser ablation refers to the removal of material from a target surface, usually a solid, by focused laser pulses of high irradiance ($> 10^8$ W cm^{-2}). When this occurs, the surface is heated locally on a small area ($A \lesssim 1$ mm^2) and material will begin to melt and vapourise; as heating continues, the vapour will become ionised expanding in the form of a plasma plume composed of excited neutrals, ions and electrons, which expands normal to the target. Numerous physical mechanisms are involved in the generation of plasmas by a laser pulse, therefore, the dynamics of this process, especially in its first stages, are still a matter of intensive research. Parameters such as laser pulse duration, energy and wavelength, material composition, surface morphology and ambient conditions all influence plasma formation and evolution.

There are many applications of laser ablation well established in both fundamental and applied research, some examples being precision machining and etching, chemical analysis and processing, thin film deposition and nanoparticle fabrication. The research group here in Trinity College Dublin has particular interest in the two latter applications, which provides a strong drive to understand the expansion dynamics of the plasma plume, and which ultimately influences how thin films or nanoparticles are formed. To that effect, the following is a description of the main processes in-

volved in the formation and expansion of the laser plume by nanosecond laser pulses on metals:

The ablation process will be discussed under the following phases:

1. Target heating
2. Vapourisation
3. Plasma formation
4. Plume expansion

1.1.1 Target Heating

The interaction of focused laser pulses with a solid target involve a complex series of processes dependent on pulse duration and wavelength, as well as material composition. From the material point of view, interaction with metallic targets is generally treated classically using the Drude model, which considers the valence electrons as if they were free particles. This leads to the representation of metals as a solid lattice surrounded by a dense electron cloud [8]. Based on this model, electron densities N_e^l range from $10^{28} - 10^{29}$ m^{-3}, calculated as the product of the solid's atomic density times the number of valence electrons. Indeed, when compared to dielectrics, the high thermal/electric conductivity of metals is due to this large number of 'free' electrons. In this case, the electric conductivity is proportional to the free electron density ($\sigma \propto N_e^l$). [9]. Heating of the target occurs as the photons of the incident laser pulse excite the valence electrons and a thermal wave propagates into the target volume around the irradiated spot. This thermal wave is an energy flux that propagates via collisions of "hot" electrons at the the irradiated surface with "cold" electrons within the material bulk. One can therefore express the electron thermal conductivity as: $K_e = (l_e n \bar{v} k_B/2)$, where l_e is the electron mean free path, n is the electron number per unit volume, $\bar{v}$ is the average electron velocity and k_B is Boltzmann's constant [10]. I.e., $K_e \propto N_e^l$.

Phase transitions to the liquid and vapour phase will ensue, provided the laser fluence [$\mathrm{J\,cm^{-2}}$] or irradiance[$\mathrm{W\,cm^{-2}}$] is high enough (the fluence threshold for laser ablation of metals is of the order $F \approx 1\ \mathrm{J\,cm^{-2}}$) [11].

In the case of nanosecond laser pulses, such as those used in this work, heat propagation into the target is generally modeled using the one-dimensional heat conduction equation:

$$\rho C \frac{\partial T}{\partial t} = \frac{\partial T}{\partial z}\left(K \frac{\partial T}{\partial z}\right) + A\alpha I(t) e^{-\alpha z} \tag{1.1}$$

where ρ is the density, C is the specific heat, T temperature, K thermal conductivity, A absorbance, a absorption coefficient and I the incident laser intensity [12]. Note that the thermophysical parameters ρ, C and K, as well as the the optical term A are all temperature-dependent parameters; this makes Eq. 1.1 difficult to solve analytically. However, good approximations are found when the thermophysical parameters are taken as temperature-independent, furthermore, the absorbance can be considered as constant during laser irradiation [13]. One solution to the heat conduction equation involves approximating the laser pulse using a Gaussian temporal profile $I(t) = I_0 exp[-(t - t_1)^2/t_0^2]$. Solving Eq. 1.1 numerically gives the maximum surface temperature:

$$T_g^{max} = 2.15 A I_0 \left(\frac{t_0}{\pi \rho C K}\right)^{1/2} \tag{1.2}$$

where $2t_0$ is the full width at half maximum (FWHM) of the laser pulse.

In cases such as laser welding, the molten phase is of major importance, and special attention is given to the liquid phase character, convective flow and solidification. However, in applications such as thin film deposition, target melting should be largely avoided. Molten droplets may be expelled due to vapour recoil pressure resulting in thin film damage [14].

1.1.2 Vapourisation

Evaporation at the target surface, whether in a solid or liquid phase, is described by the Hertz-Knudsen equation:

$$J_i = s\frac{p_s(T) - p_i}{(2\pi m_i kT)^{1/2}} \tag{1.3}$$

where J_i is the flux and m_i the mass of ion species i leaving the target surface, s is the evaporation coefficient, p_i is the partial pressure at infinity and p_s the saturated vapour pressure, which is given by the Clausius-Clapeyron relation:

$$p_s(T) = p_1 e^{-\frac{\Delta H_V}{R}\left(\frac{1}{T} - \frac{1}{T_b}\right)} \tag{1.4}$$

where $p_1 = 1$ atm, ΔH_V is the enthalpy of evaporation at boiling point temperature (T_b), R is the gas constant and k is Boltzmann's constant. Note that when in pressure equilibrium ($p_i = p_s(T)$), there is no particle ejection, whilst at $p_i = 0$ the flux is maximized. The above equations describe what is often called normal vapourisation; occurring at low densities of emitted particles (low fluence) where thermal equilibrium between the vapour and target is assumed. In this fluence regime, species leave the target surface at gas-kinetic velocities.

As fluence increases, namely in the regime of interest for thin films, a much higher quantity of particles is produced at the surface, resulting in a highly collisional cloud of gas that rapidly reaches thermal equilibrium. This occurs in a very thin layer close to the target called the Knudsen Layer (KL) [15]. The thickness of the KL is only a few mean free paths of species and beyond this boundary the plasma undergoes hydrodynamic (adiabatic) expansion.

1.1.3 Plasma Formation

An increase in laser irradiance on the target surface will cause ionisation of the expelled vapour and a plasma will be formed. The degree of ionisation (ξ), given

by collisions between thermal electrons and atoms within a gas at temperature T, is given by the Saha equation:

$$\frac{\xi^2}{1-\xi} = \frac{2}{n_e + n_a}\frac{g_i}{g_a}\left(\frac{2\pi m_e kT}{h^2}\right)^{3/2} e^{-(\chi/kT)}. \tag{1.5}$$

Here, $\xi = (n_e/n_e + n_a)$; where the subscripts i, e and a refer to ions, electrons and atoms respectively, n is the number density, g is the state degeneracy, χ is the ionisation energy and m_e is the electron mass. This formula holds only when $n_i = n_e$ [16].

When nanosecond laser pulses are used, the incoming pulse will not only interact with the target solid, but with the ejected vapour as well. As the laser fluence is increased, a greater fraction of atoms will become ionized, whereby the expanding vapour is considered a plasma. A significant number of free electrons will be present in the vapour as it approaches full ionisation ($\xi \approx 1$), thus, inverse Bremsstrahlung (IB) will be the main absorption mechanism of the incoming laser light. The absorption coefficient of the vapour/plasma is given by:

$$\alpha_{IB} = 1.37 \times 10^{-35}\lambda^3 \frac{\bar{Z}^2 n_i n_e}{T^{1/2}}\left[1 - e^{-\hbar\omega/kT}\right] \tag{1.6}$$

where $\bar{Z}$ is the mean ionisation and λ [μm] is the wavelength. It should be noted that for laser pulse widths greater than a few picoseconds, this absorption will have a shielding effect, whereby part of the laser pulse energy does not reach the target. An extreme case of absorption of laser radiation by the expanding plasma is the effect of optical breakdown, most notable in lasers with high intensities and long pulse widths (e.g. CO_2 lasers). Here, high laser fluences will increase IB absorption and photoionization, resulting in cascade ionisation due to energetic electrons in the plasma. This effect will lead to growth of the plasma cloud in the direction of incoming radiation in a so-called *laser supported absorption wave* [16].

1.1.4 Plume Expansion

The expanding plasma plume is observed macroscopically as a semi-ellipsoid, having an elongated shape along the axis normal to the target. One of the most widely-used models for describing this expansion is that developed by Anisimov [17], which is based on the following general assumptions:

1. The expansion is adiabatic: The plasma expands freely into vacuum once the laser pulse ends, implying no more heat is supplied to- or removed from- the plasma.

2. The expansion is isentropic: There is no heat exchange within the plasma as it propagates.

3. The expansion is self-similar: Physical parameters such as density and pressure are constant across semi-ellipsoidal surfaces.

As thermal energy is converted to kinetic energy within the Knudsen layer, the vapour undergoes hydrodynamic expansion governed by the gas-dynamic equations:

$$\frac{\partial \rho}{\partial t} + \nabla \cdot (\rho v) = 0 \tag{1.7}$$

$$\frac{\partial v}{\partial t} + (v \cdot \nabla)v + \frac{1}{\rho}\nabla p = 0 \tag{1.8}$$

$$\frac{\partial S}{\partial t} + (v \cdot \nabla)S = 0 \tag{1.9}$$

where ρ is the density, v the velocity, S is entropy and p is pressure. Furthermore, if the plume is considered an ideal gas, the adiabatic constant is taken as $\gamma = C_P/C_V = 5/3$ where C_P and C_V are the heat capacities at constant pressure and volume respectively. At time zero, the plasma is considered to have initial values of mass M_p, radius R_0, length Z_0 and energy E_p. The initial radius is taken as

that of the laser spot, whilst the length (distance from target surface to plasma front) is approximated as $Z_0 \approx v_s \tau_l$, where v_s is the sound velocity and τ_l is the laser pulse duration. As time progresses, the plasma front expands described by the coordinates *X(t)*, *Y(t)* and *Z(t)* as shown in Fig. 1.1. In this schematic, elliptical plume contours are shown for increasing time t_n.

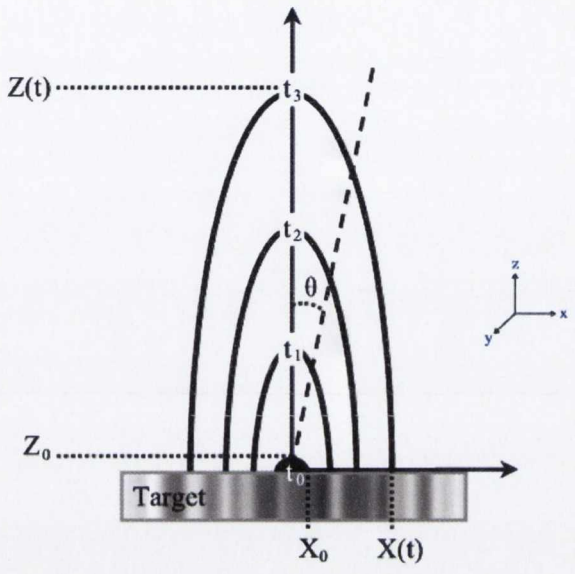

Figure 1.1: Plume expansion schematic

The following density, pressure and entropy profiles are obtained from the solutions to the gas-dynamic equations in an isentropic expansion:

$$n(x,\, y,\, z,\, t) = \frac{N_0}{I_1 X(t) Y(t) Z(t)} \left[1 - \left(\frac{x}{X(t)}\right)^2 - \left(\frac{y}{Y(t)}\right)^2 - \left(\frac{z}{Z(t)}\right)^2\right]^{1/(\gamma-1)} \tag{1.10}$$

$$\begin{aligned} p(x,\, y,\, z,\, t) \;=\; & \frac{E_0}{I_2 X(t) Y(t) Z(t)} \left[\frac{X_0 Y_0 Z_0}{X(t) Y(t) Z(t)}\right]^{\gamma-1} \\ & \times \left[1 - \left(\frac{x}{X(t)}\right)^2 - \left(\frac{y}{Y(t)}\right)^2 - \left(\frac{z}{Z(t)}\right)^2\right]^{\gamma/(\gamma-1)} \end{aligned} \tag{1.11}$$

$$S(x,\, y,\, z,\, t) \;=\; \frac{1}{\gamma-1}\,\ln\left\{\frac{\mathrm{E_0}}{\mathrm{I_2X_0Y_0Z_0}}\left[\frac{\mathrm{I_1X_0Y_0Z_0}}{\mathrm{M_p}}\right]^{\gamma} \times\left[1-\left(\frac{x}{X(t)}\right)^2-\left(\frac{y}{Y(t)}\right)^2-\left(\frac{z}{Z(t)}\right)^2\right]\right\} \tag{1.12}$$

where I_1 and I_2 are functions of γ, $N_0 = \int n(\mathbf{r},\, t)dV$ and $E_0 = (\gamma-1)^{-1}\int p(\mathbf{r},\, t)dV$. Note that S, p and n are terms which remain constant over ellipsoidal surfaces: $\frac{x^2}{X^2}+\frac{y^2}{Y^2}+\frac{z^2}{Z^2} = const.$ for plume boundaries X, Y and Z. Further details of this derivation can be found in Refs. [17] [18]. Three coupled ordinary differential equations are thus obtained for the gas-dynamic equations using the above solutions (Eqs. 1.10, 1.11 and 1.12) [19]. This has the form:

$$X(t)\frac{d^2X}{dt^2}+Y(t)\frac{d^2Y}{dt^2}+Z(t)\frac{d^2Z}{dt^2} = A\left[\frac{X_0Y_0Z_0}{X(t)Y(t)Z(t)}\right]^{\gamma-1} = \left[\frac{V_0}{V}\right]^{\gamma-1} \tag{1.13}$$

where $A = (5\gamma-3)E_p/M_p$. From the above model, there are various characteristics that arise [20]:

1. As the plume begins to expand, strong pressure gradients accelerate the vapour in all directions, yet these gradients rapidly go to zero and the expansion becomes inertial.

2. Initially, pressure gradients are greater in the Z direction, given that this dimension is much smaller than the spot size, which results in the plume having a characteristic semi-ellipsoidal shape.

3. The same pressure gradients mentioned above also give rise to the so-called flip-over effect. This implies that during the acceleration phase, for an initial spot size X_0, Y_0 where $X_0 < Y_0$, the pressure gradient will laterally drive the plasma having the shortest dimension causing it to expand at a higher rate. This results in the dimensions X_1, Y_1 at a later time where $X_1 > Y_1$.

4. Assuming cylindrical symmetry ($X(t) = Y(t)$), the elongation or ellipticity of the plume (k) is a function of the lateral and longitudinal expansions: $k(t) = Z(t)/X(t)$. If the plasma is not cylindrically-symmetric there will be two k values (k_x and k_y).

5. The angular distribution of the plume will be given by: $cos^n\theta$, where $n = 3k^2$ [17].

1.2 Optical Emission Spectroscopy

Excited atoms and ions in a gas will emit characteristic spectral lines throughout the UV, visible and IR spectrum. In the case of a transient event, such as a laser produced plasma or pulsed arc discharge, the plasma has a lifetime of only a few microseconds from the initial material vapourisation. During this time, high excitation rates due to electron collisions will populate electronically excited states in the atoms, emitting light quanta as they decay to their ground state. In order to detect and analyse this emission, a spectrometer can be used, however, when using a conventional detector such as a CCD or photodiode array, the light emitted during the entire event is temporally integrated. In order to obtain spectra resolved in time, detection devices capable of capturing events with nanosecond exposure times are required. The microchannel plate (MCP) is such a device, which allows gating down to about 2 ns. Coupled to an intensified CCD, this detector is also capable of collecting light of very low emission intensity.

In addition to temporal resolution, being able to distinguish the various emitting particles spatially is also desirable. Two common techniques are:

1. Point imaging system. An imaging system collects local emission from the plasma, which is focused onto a fibre optic coupled to the spectrometer. Spatial resolution is achieved by displacing the imaging system parallel to the plume axis. The detector can be a one-dimensional array [21].

2. Direct plume imaging. A light collection system images the plume onto the spectrometer slit. By using two-dimensional detection, such as a CCD, the plume emission spectrum is resolved spatially [22].

1.2.1 Transitions and Thermodynamic Equilibrium

When analyzing emission from laser produced plasmas, a strong continuum is observed within the first few nanoseconds after the laser pulse. As time elapses, lines will begin to form as the plasma expands and cools, producing a spectrum characteristic of the material being ablated. The distinct forms of emission seen during the ablation process are the result of three transition types: bound-bound (*b-b*), bound-free (*b-f*) and free-free (*f-f*) [23] [24]. These are illustrated in Fig. 1.2.

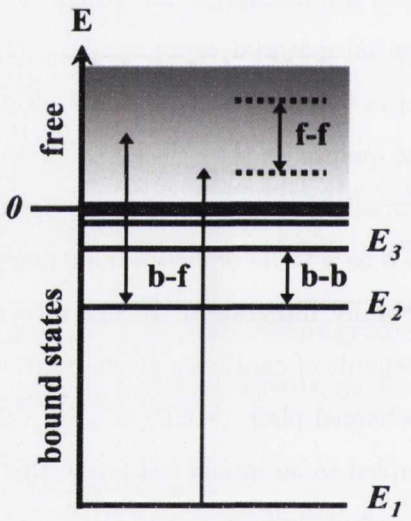

Figure 1.2: Electronic transitions present in LPP's. The zero-level represents the boundary between bound and free electrons.

1. **Bound-bound** transitions occur between two electronic bound states and is therefore discrete, producing line radiation of a specific photon energy/wavelength.

2. **Bound-free** transitions occur during processes of photoionisation (when an incoming photon has energy exceeding the binding energy of the electron) and

radiative recombination (electron capture). Since only the bound electron is quantized, a continuum spectrum is observed. For a given bound state j, these transitions are represented as: $A_j + h\nu \leftrightarrow A^+ + e^- + \epsilon$, where ϵ is the electron kinetic energy.

3. **Free-free** transitions, also known as *Bremsstrahlung* (braking radiation), are a source of continuum radiation as well. The process of electron acceleration in the field of surrounding ions causes them to gain or lose energy ($h\nu = \Delta\epsilon$). The process known as *Inverse Bremsstrahlung* also falls into this category, where electrons absorb energy from incoming photons.

This work will be dealing mostly with the intensities of bound-bound transitions, rendering information on radiating atoms and ions as the plasma plume expands.

When an electron makes a transition within the field of an ion or atom, the irradiance observed will depend on [25]: (a) the transition probability; (b) the number of electrons occupying the upper level of the transition; (c) the probability emitted photons will not be absorbed while traversing the plasma.

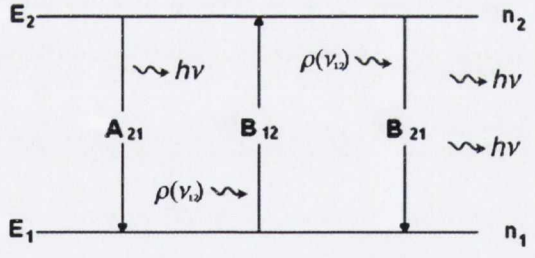

Figure 1.3: Transitions by spontaneous emission, absorption and stimulated emission.

Consider a two-level system with an upper energy level E_2 and lower level E_1, having respective populations n_2 and n_1 (see Fig. 1.3). The probability of a transition from the excited state to the lower state by the spontaneous emission of a photon with energy $h\nu_{12}$ is A_{12}. Conversely, the probability of an electron absorbing a photon

of energy $h\nu_{12}$ is given by B_{12}. Stimulated emission, whereby, an incident photon stimulates the emission of a 2^{nd} photon, also with energy $h\nu_{12}$ has a probability B_{21}.

In the presence of radiation with density $\rho = \rho(\nu_{12})$, the above B transition probabilities can be expressed as transition rates: $B_{12}n_1\rho$ and $B_{12}n_2\rho$ (s^{-1}).

In a system in thermodynamic equilibrium, such as a black body, the upward and downward transitions are equal:

$$A_{21}n_2 + B_{21}\rho(\nu_{12})n_2 = B_{12}\rho(\nu_{12})n_1 \tag{1.14}$$

Therefore, solving for ρ, the radiation density is:

$$\rho(\nu_{12}) = \frac{A_{21}}{B_{12}(n_1/n_2) - B_{21}} \tag{1.15}$$

The relative distribution of states when a system is in thermodynamic equilibrium is described by the Boltzmann distribution. At a given temperature T this is:

$$\frac{n_2}{n_1} = \frac{g_2}{g_1}e^{-(E_2-E_1)/kT} \tag{1.16}$$

where n is the number density, g is the statistical weight and E is the energy. The relation between the transition rates and the distribution of states can be assessed by substituting Eq. 1.16 in Eq. 1.15:

$$\rho(\nu_{12}) = \frac{A_{21}}{B_{12}\left(\frac{g_1}{g_2}e^{(E_2-E_1)/kT}\right) - B_{12}} \tag{1.17}$$

where the transition energy $h\nu = E_2 - E_1$. Therefore, for the particular case where: $g_1B_{12} = g_2B_{21}$ and $A_{21} = [8\pi h(\nu_{12}/c)^3]B_{21}$ one obtains the Planck blackbody equation:

$$\rho(\nu_{12}) = \frac{8\pi h\nu^3}{c^3}\frac{1}{e^{-h\nu/kT} - 1} \tag{1.18}$$

Blackbody radiation, characterized by a wavelength and temperature-dependent radiation density function, assumes an equilibrium system where radiative emission and absorption are perfectly balanced. As considered previously, one of the characteristics of the irradiance of a spectral line was the probability of a photon escaping without being absorbed; which will naturally depend on the number of absorbers present in the medium and the probability of absorption taking place at a particular transition B_{12}. If light of wavelength λ traverses an absorbing medium of thickness dx, the change in irradiance dI is expressed as: $dI_\lambda(x) = \kappa_\lambda I_\lambda(x)dx$, where κ_λ is the absorption coefficient. Within a homogeneous medium, the solution to this equation is expressed as:

$$I_\lambda(x) = I^0_\lambda e^{-\kappa_\lambda x} \tag{1.19}$$

where I^0 is the incident irradiance. Equation 1.19 is also known as Beer's Law; the argument in the exponential function is termed optical thickness or optical depth: $\tau_\lambda = -\kappa_\lambda x$. If the optical depth is greater than unity ($\tau_\lambda \gg 1$), it is said the plasma is *optically thick*, conversely, when the optical depth is smaller than unity ($\tau_\lambda \ll 1$) the plasma is *optically thin* [26]. The absorption coefficient can also be expressed in terms of a particular transition as:

$$\kappa(\lambda) = \pi r_0 \lambda^2 f_{12} n_1 \left(1 - e^{-hc/\lambda kT}\right) P(\lambda) \tag{1.20}$$

where $P(\lambda)$ represents the spectral line profile function (e.g. Lorentzian or Voigt) and f_{12} is the absorption oscillator strength, which is related to the Einstein A coefficient by [27]:

$$f_{12} = \frac{\epsilon_0 m_e c \lambda_{21}^2}{2\pi e^2} \left(\frac{g_2}{g_1}\right) A_{21} \tag{1.21}$$

Note that a plasma may be optically thick / thin for certain transitions only, in other words, there are plasma systems where the blackbody radiation density is not high enough to maintain equilibrium for the entire gas at a single temperature, and yet,

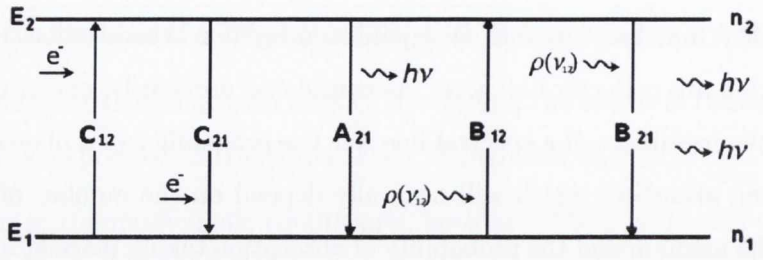

Figure 1.4: Two-level transitions including collisional and radiative cases.

a high density of excited states is maintained purely by electron collisions. Indeed, there exist systems where thermodynamic equilibrium is satisfied for certain levels and temperatures; these are said to be in local thermodynamic equilibrium (LTE). Figure 1.4 shows the added collisional processes involved in transitions of a 2-level system, where the collision rates are given by: $n_1 C_{12} = n_2 C_{21}$.

1.2.2 Local Thermodynamic Equilibrium

In a plasma, the process of ionisation and recombination can be the result of either collisional or radiative effects. The following terms describe these transitions in equilibrium:

$$A + e^- \Longleftrightarrow A^+ + 2e^- + \Delta\epsilon \qquad \text{(Collisional excitation / 3-body recombination)}$$

$$A + h\nu \Longleftrightarrow A^+ + e^- + \Delta\epsilon \qquad \text{(Radiative recombination / photoionization)}$$

where $\Delta\epsilon$ is the electron kinetic energy balance.

Thermodynamic systems in LTE remain in equilibrium only at certain times and in certain regions of the plasma, where the Boltzmann and Maxwell distributions hold for a given temperature. Another type of distribution found in LTE conditions is used when dealing with ionised gases. When collisions between electrons and atoms

or molecules are such that considerable ionisation results, the Saha equation is used to describe the ionisation of a gas at temperature T:

$$\frac{n_i n_e}{n_a} = 2\left(\frac{2\pi m_e kT}{h^2}\right)^{1/2} \frac{g_i}{g_a} e^{-(\chi/kT)} \tag{1.22}$$

where the subscripts a, i and e refer to to atoms, ions and electrons respectively, g is the state degeneracy (statistical weight). This formula was mentioned previously (Eq. 1.5) in terms of degree of ionisation: $\xi = n_e/(n_e + n_a)$ [16]. An important point to make is whether or not the plasma being studied is indeed in LTE. As mentioned above, at higher densities where the plasma is optically thick, radiative emission and absorption balance each other out. It was also stated that an optically thin plasma in LTE must be dominated by collisional transitions. However, if the plasma density decreases sufficiently to the point where the probability of a radiative transition is equal, or exceeds the probability of a collisional transition, level populations will no longer follow the Boltzmann distribution and LTE breaks down. In other words, the collisional transition rate should exceed the radiative decay rate by a substantial margin (at least a factor of ten).

Consider a two-level system where electrons can occupy an upper level (2) and may decay to a lower level (1). A collisional transition rate C can be defined as:

$$C = n_e n_2 X \tag{1.23}$$

where X is a de-excitation coefficient. Therefore, based on the above criteria, the following inequality must hold for LTE: $C \geq 10 n_2 A_{21}$, (A_{21} - transition probability). The above leads to an inequality relating the minimum plasma density necessary for LTE in terms of electron temperature and transition energy level difference ΔE:

$$n_e \geq 1.6 \times 10^{12} T_e^{1/2} (\Delta E)^3 \qquad [cm^{-3}] \tag{1.24}$$

where T_e is given in [K] and ΔE in [eV]. This somewhat qualitative description is

based on the work of R. McWhirter [25] in the 1960's, and still widely quoted in the literature as a necessary condition for LTE.

1.2.3 Plasma Temperature from Spectroscopic Measurements: Relative Line Intensities

As seen in the previous section, line intensities are directly related to the level populations and transition probabilities. Spectral line emission can be measured in different ways, and it is necessary at this point to clarify the different units encountered in the literature. In this work, conventions will be taken from the book by A. Thorne et.al. "Spectrophysics: Principles and Applications" [23].

The term "intensity" in common language is a widely misused unit to measure emission strength. Light *intensity* is actually a measure of the power per unit solid angle [$\mathrm{W\,sr^{-1}}$], used generally to measure emission from a point source. *Irradiance*, on the other hand, having units of power per unit area [$\mathrm{W\,m^{-2}}$], aptly describes the emission from a radiating surface, and as such, is used throughout this work. Notwithstanding, when dealing with emission in spectral terms, the power per unit area per unit solid angle [$\mathrm{W\,m^2\,sr^{-1}}$] or *radiance* will be used to describe the emission from a radiating surface. What is actually measured by the spectrometer in the experiments herein is the radiance per unit wavelength [$\mathrm{W\,m^2\,sr^{-1}\,nm^{-1}}$], i.e. *spectral radiance* L_λ. Finally, the so-called *emissivity* $j(\lambda)$, which is the spectral radiance per unit thickness x, is measured as [$\mathrm{W\,m^{-3}\,sr^{-1}\,nm^{-1}}$]. Indeed, the integral of $j(\lambda)$ over the spectral line width is related to the irradiance, as well as to the Einstein A coefficient as:

$$I_{21} = \int L_\lambda d\lambda = \int x\, j(\lambda)\, d\lambda = x \frac{n_2 hc}{4\pi\lambda_{21}} A_{21} \tag{1.25}$$

If the population follows a Boltzmann distribution, the irradiance is given by:

$$I_{21} = \alpha \frac{g_2 A_{21}}{\lambda_{21}} e^{-E_2/kT} \tag{1.26}$$

where α represents a constant inherent to the terms common to all lines in the measurement. Based on the above equation, it is possible to obtain a value of temperature by taking the ratio of intensities of two lines in the same ionisation stage. Thus, for a pair of lines with upper energy levels i and j:

$$\frac{I_i}{I_j} = \frac{g_i A_i \lambda_j}{g_j A_j \lambda_i} e^{-(E_i - E_j)/kT} \tag{1.27}$$

Note that in order to determine T, it is necessary to have reliable values for the level degeneracies g, transition rates A and upper-level energies $E_{j,k}$ for the transitions involved. The above description can be extended to the case where multiple lines of the same ionisation species are available. Based on Eq. 1.26, a so-called Boltzmann plot can be constructed by graphing the logarithm of $I\lambda/gA$ vs. the upper-level energy E_2, with the resulting line having slope equal to $-1/kT$. It is worth noting that only relative line irradiances are required to estimate the electron temperature, and that one need not know the value of the constant α explicitly.

It is also possible to determine the temperature of two lines from different ionisation stages by invoking the Saha and Boltzmann distributions. Combining Eq. 1.16 and Eq. 1.22, gives the relative number densities of ions in two different ionisation stages (i and i+1) with respective upper states j and k:

$$\frac{n_e n_{i+1,k}}{n_{i,j}} = \frac{2(2\pi mkT)^{3/2}}{h^3} \frac{g_{i+1,k}}{g_{i,j}} e^{-((\chi + E_k - E_j)/kT)} \tag{1.28}$$

where, χ is the ionisation energy of the i^{th} ionisation stage. The diagram in Fig. 1.5 illustrates the above equation.

Based on Eq. 1.28, the relative ionisation stages can be expressed in terms of relative line intensities instead of number densities. Substituting Eq. 1.25 in the Saha-Boltzmann equation:

$$\frac{I_{i+1,k}}{I_{i,j}} = \frac{(A/\lambda)_{i+1,k}}{(A/\lambda)_{i,j}} \frac{2(2\pi mkT)^{3/2}}{h^3 n_e} \frac{g_{i+1,k}}{g_{i,j}} e^{-((\chi + E_k - E_j)/kT)} \tag{1.29}$$

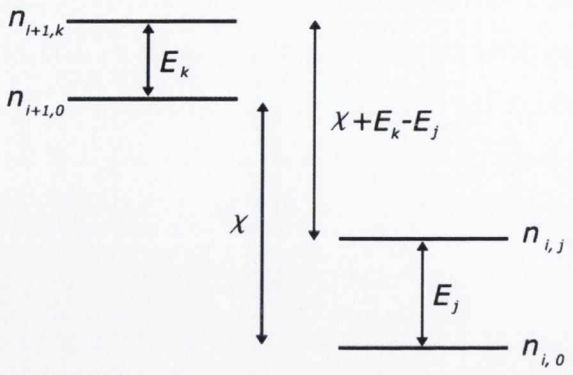

Figure 1.5: Energy levels for Saha-Boltzmann equation.

This equation is often known as the coupled Saha-Boltzmann equation. Following a similar procedure to that of Eq. 1.27, the above equation can be linearised by taking the logarithm:

$$ln\left(\frac{I_{i+1,k}(A/\lambda)_{i,j}\, g_{i,j}}{I_{i,j}(A/\lambda)_{i+1,k}\, g_{i+1,k}}\right) = ln\left(\frac{2(2\pi mkT)^{3/2}}{h^3 n_e}\right) - \frac{\chi + E_k - E_j}{kT} \tag{1.30}$$

Note that although the ordinate term in the linear equation contains a temperature value, it varies very little over a broad temperature range. Furthermore, the intercept may be useful to determine a plasma electron density.

1.2.4 Plasma Density from Spectroscopic Measurements: Stark Broadening

The width of a spectral line depends on a variety of factors, inherent to both the light source being analysed and the instrument used to capture it. Even when a highly monochromatic source is used to generate a spectrum, the width of the spectral line or lines will be limited by the resolution of the spectrometer. Once the resolution is well characterized, physical information from the light source can be inferred from any additional width detected from a specific line, a term generally known as spectral line broadening. This broadening can be roughly categorized in to 3 types: - *Natural* broadening, *Doppler* broadening and *Pressure* broadening.

The first of these is inherent to any transition, and stems from the finite decay time for spontaneous emission (cf. Einstein coefficients). This term is generally of the order of $10^{-4} - 10^{-5}$ nm, and therefore, negligible [28]. Doppler broadening results from the motion of radiating particles towards or away from the line-of-sight of the observer. Therefore, a radiating particle moving with velocity v parallel to the line of observation will produce an apparent wavelength shift $\Delta\lambda = \pm\lambda v/c$. Using the Maxwell distribution of velocities for a gas in thermodynamic equilibrium, a simple term is derived for the Doppler half-width as [29]:

$$\Delta\lambda_{1/2} = 2\sqrt{ln2}\sqrt{\frac{2kT\lambda_0^2}{mc^2}} \tag{1.31}$$

For the low temperature plasmas produced by laser ablation, this term is generally neglected as well. For instance, an aluminium plasma at a temperature of 3 eV will have a Doppler-broadened line at 500 nm of $\Delta\lambda_{1/2} = 0.01$ nm, a value that would only be measured with a high resolution spectrometer [30]. The third type of line broadening, namely pressure broadening, is actually subdivided into three types: *Resonance*, *Van der Waals* and *Stark* broadening. These are physically related to identical-atom systems, different-atom/molecule systems and and charged particles respectively. Since this work is mainly concerned with charged particle interactions, only Stark broadening will be considered here.

Stark broadening of spectral lines comes from the Stark effect in quantum mechanics, whereby an atom or ion perturbed by an electric field results in splitting of the energy levels. According to perturbation theory, symmetric splitting will occur in the case of hydrogen atoms, as a result of the linear dependence with the electric field E (linear Stark effect). Conversely, non-symmetric splitting will occur for all other atomic systems, being proportional to E^2 (quadratic Stark effect), appearing red-shifted. Given that the number of perturbers (electrons and ions) directly affects the broadening term, it therefore follows that the increased width observed will strongly depend on the plasma density. Indeed, the broadened line will have a width (in [Å]) of:

$$\Delta\lambda = 2w\left(\frac{n_e}{10^{16}}\right) + 3.5A\left(\frac{n_e}{10^{16}}\right)^{5/4}\left(1 - \frac{3}{4}N_D^{-1/3}\right)w. \tag{1.32}$$

In this equation, A is the ion broadening parameter, w is the electron impact width parameter and N_D is the number of particles in the Debye sphere (in $[cm^{-3}]$). Note that n_e is also in $[cm^{-3}]$, whilst A and w are in [Å] and can generally be found tabulated in the literature [31], [32], [33]. The terms in Eq. 1.32 are the broadening contributions due to electrons (LHS) and ions (RHS), where the ionic term is generally negligible given the much slower response of ions to perturbations. Another approach to explaining this is using the impact approximation, which states that the greater contribution of electrons to broadening is due to their high velocities, i.e. collision rates. Electron impact broadening would then be responsible for a much greater number of collision-induced transitions than ions [34].

The Debye term N_D in the above equation arises from the distance at which charge neutrality in the plasma no longer holds. In other words, one can consider a plasma as macroscopically quasi-neutral ($n_i \backsimeq n_e \backsimeq n$) down to a critical distance where charged particles are no longer shielded by the surrounding ions and electrons. This distance is termed Debye length (λ_D), and is the radius of a sphere, inside which, individual particle interactions become significant:

$$\lambda_D = \left(\frac{\epsilon_0 kT}{2e^2 n_e}\right)^{1/2} \tag{1.33}$$

or, in simpler form:

$$\lambda_D = 740\left(\frac{kT}{n_e}\right)^{1/2} \tag{1.34}$$

where λ_D is in [cm], kT in [eV] and n_e in [cm^{-3}].

Therefore, given an electron density n_e, the number of particles in a sphere of radius λ_D is:

$$N_D = n_e\frac{4}{3}\pi\lambda_D^3 \tag{1.35}$$

For example, a plasma at a temperature of 3 eV and a density of 10^{14} cm^{-3} will have ~900 ions in a sphere of radius ~130 μm.

1.3 Vacuum Arc Spots

A vacuum arc is a high-current discharge where plasma is formed in the inter-electrode gap by vapourisation and ionisation of the cathode surface material. This dense vapour is generated at localized areas on the cathode surface, called arc spots, which are responsible for providing both the evaporated material and intense electron emission during the discharge event. Arc spots are initially formed at areas of high field emission on the cathode surface, such as protrusions or sharp edges [35]. As the current density increases, local melting by joule heating will eventually lead to an explosive release of conducting medium followed by the formation of a spark discharge [1].

Each spot is a conglomerate of smaller microspots also known as ectons [36], which are 1-3 μm in size. Ectons are transient in nature, decaying and re-forming as the spot moves along the cathode surface [37]. Each of these smaller spots is able to carry 1-10 A of current, constituting one of multiple separate microjets expelling plasma out to ~100 μm, a distance at which mixing occurs to form a large spot [38]. "Macro" spots, on the other hand, have been shown to measure 100-300 μm and carry ~100 A of current, whereby, if the demand for higher current flux increases, the spots will both multiply and move around the surface in a so-called retrograde motion. Some studies have shown the spots may expand radially away from the center, sometimes following an annular pattern. It has been suggested this expanding ring phenomenon is due to the differences in magnetic flux inside and outside the current-carrying ring [39]. Ion current is generally neglected, given only 8-10% of the total arc current comes from anode ions. Furthermore, this occurs on relatively diffuse areas of the surface, the exception being when very high currents (5-10 kA) are present. Notwithstanding, luminous areas on the anode surface may indeed be visible, even at lower currents (authors make a distinction between anode jets, anode

spots and footpoints, the latter being low-current, diffuse emission centers) [40].

1.4 Magnetohydrodynamics (MHD) and the Z-Pinch

1.4.1 MHD Equations and the Static Pinch

As mentioned in the introduction, one of the main motivations of this work was experimentation to obtain a zeta pinch, a form of magnetic confinement of plasma. The well known Bennett condition, which expresses the balance between magnetic and plasma pressure offers an approximate estimate of the plasma and discharge conditions required for a pinch. What follows is a simple derivation of this equation based on the resistive MHD model.

Once magnetic fields are present in the vicinity of a plasma, one must turn to magnetohydrodynamics (MHD), where a closed set of formulae, including Maxwell's equations, is used to describe the interaction of magnetic fields, whether external or induced, with the flow of plasma. There are various models used to describe magnetohydrodynamic behaviour; one-fluid, dual-fluid, ideal and resistive are but a few. The latter two will be considered herein, with special emphasis on the resistive model. There are three fundamental MHD equations, namely mass continuity, conservation of momentum and Ohm's Law which combined with an equation of state (which will assume an adiabatic plasma with a Maxwellian distribution) serve to describe interactions of plasma and field. These equations are, respectively:

$$\frac{\partial \rho_m}{\partial t} = \nabla \cdot (\rho_m \mathbf{U}) = 0 \tag{1.36}$$

$$\rho_m \frac{d\mathbf{U}}{dt} = \mathbf{J} \times \mathbf{B} - \nabla P \tag{1.37}$$

$$\mathbf{J} = \sigma(\mathbf{E} + \mathbf{U} \times \mathbf{B}) \tag{1.38}$$

$$\frac{d}{dt}(P\rho_m^{-\gamma}) = 0 \tag{1.39}$$

where ρ_m is the mass density, $\mathbf{U}$ the velocity, P is the pressure, $\mathbf{J}$ is the current density, σ is the conductivity and γ is the adiabatic constant $\gamma = C_P/C_V$. One of the main differences between the ideal and resistive MHD models comes from Ohm's Law 1.38, where σ is taken to be infinite in the ideal case (i.e. the plasma is considered a perfect conducting medium), whilst the resistive model allows for energy dissipation given $\sigma \ll \infty$ (albeit, neglecting other loss terms such as viscous flow and heat conduction) [41]. In addition to the MHD equations, Maxwell's equations are required as well:

$$\nabla \times \mathbf{B} = \mu_0 \mathbf{J} + \mu_0 \epsilon_0 \frac{\partial \mathbf{E}}{\partial t} \tag{1.40}$$

$$\nabla \cdot \mathbf{B} = 0 \tag{1.41}$$

$$\nabla \times \mathbf{E} = -\frac{\partial \mathbf{B}}{\partial t} \tag{1.42}$$

$$\nabla \cdot \mathbf{E} = \frac{\rho_q}{\epsilon_0} \tag{1.43}$$

In the resistive model, two further simplifications are considered -Due to slow temporal variation, the displacement current in Ampere's law (Eq. 1.40) ($\mu_0\epsilon_0\partial\mathbf{E}/\partial t$) is negligible compared to the conduction current $\mathbf{J}$, and the plasma is considered neutral, therefore $\rho_q = 0$ in Gauss' Law (Eq. 1.43).

Bennett's condition for a plasma pinch is derived from a static equilibrium case, i.e., $\mathbf{U} = 0$. Therefore, $d\mathbf{U}/dt = 0$ and equation 1.37 can be rewritten as:

$$\mathbf{J} \times \mathbf{B} = \nabla P \tag{1.44}$$

which represents the balance between the pressure gradient and $\mathbf{J} \times \mathbf{B}$ forces (a system said to be in force-balanced equilibrium). The above can be rewritten as:

$$\frac{1}{\mu 0}(\mathbf{B} \cdot \nabla)\mathbf{B} = \nabla \left(\frac{B^2}{2\mu_0} + P \right) \tag{1.45}$$

When considering linear plasma confinement systems, it is convenient to represent the magnetic field in cylindrical coordinates, whereby: $\mathbf{B} = [0,\, B_\theta(r),\, B_z(r)]$. Substituting in Eq. 1.45, the radial component is:

$$\frac{d}{dr}\left(P + \frac{B_\theta^2}{2\mu_0} + \frac{B_z^2}{2\mu_0} \right) = -\frac{B_\theta^2}{\mu_0 r} \tag{1.46}$$

The two simplest cases arise when the current density and magnetic field are orthogonal, whereby two types of plasma pinching can occur -the Theta (θ) pinch and Zeta (Z) pinch. A schematic of the two configurations is shown in Fig. 1.6.

$$B = B_z; \quad J = J_\theta \qquad (\theta - Pinch)$$

$$B = B_\theta; \quad J = J_z \qquad (\mathrm{Z} - Pinch)$$

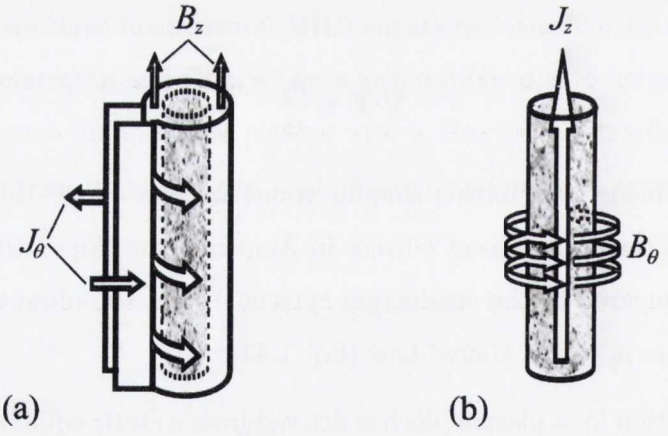

Figure 1.6: Schematic of axial/azimuthal current density J and magnetic field B for θ-pinch (a) and Z- pinch (b).

- In the theta pinch (Fig. 1.6(a)), the current flows around the plasma column and parallel axial magnetic field lines will be in the region between the conductor and the plasma, constricting it until the pressure is balanced with that of the plasma (if the plasma is a good conductor, the **B** field cannot penetrate the column) [42].
- In a pure zeta pinch (Fig. 1.6(b)), the case of interest in this work, the only contribution of the magnetic field is in the azimuthal (θ) direction.

Expanding and re-arranging Eq. 1.46 with $B_z = 0$:

$$r^2 \frac{dP}{dr} = -\frac{d}{dr}(rB_\theta)^2 \tag{1.47}$$

By the same token, the only contribution to the current density is in the z direction (J_z), thus, the current flowing in a cylinder of radius r is:

$$I(r) = 2\pi \int_0^r J_z r \, dr = \frac{2\pi}{\mu_0} r B_\theta \tag{1.48}$$

Substituting Eq. 1.48 in Eq. 1.47:

$$r^2 \frac{dP}{dr} = -\frac{\mu_0}{2} \frac{d}{dr} \left(\frac{I}{2\pi} \right)^2 \tag{1.49}$$

Integrating Eq. 1.49 within the column of plasma ($r = a$) and invoking the ideal gas law ($P = n_i k T_w$):

$$2\pi \int_0^a P r \, dr = 2\pi k T_w \int_0^a n_i r \, dr = \frac{\mu_0}{8\pi} I_a^2 \tag{1.50}$$

Where $T_w = T_i + \bar{Z} T_e$, $\bar{Z}$ is the mean plasma ionisation, I_a is the current inside the column of radius a and n_i is the ion density and one may define $2\pi \int_0^a n_i r \, dr = N_i^l$ as the ion line density. Therefore, Eq. 1.50 for a plasma in thermal equilibrium ($T_e = T_i$) becomes:

$$8\pi N_i^l kT_e(\bar{Z}+1) = \mu_0 I_a^2 \tag{1.51}$$

This equation is known as the *Bennett condition* for pinch equilibrium.

1.4.2 The Dynamic Z-Pinch

Recall the above equation was based on the assumption of static equilibrium, which allowed the derivation of the condition where magnetic and plasma pressures are equal. However, in the case of transient events such as those in this work, information on the dynamics of the pinch is also needed. To this end, three models describing the collapse of the plasma column due to a magnetic field will be reviewed: the *snowplow model*, the *slug model* and the *simplified MHD model.*

Before describing the above methods, special consideration should be given to the propagation of waves within a plasma, known as MHD or Alfvén waves. These arise when perturbations in the plasma cause the magnetic field lines to produce a 'restoring force', thus generating a wave that propagates in the direction of the magnetic field. When considering a homogeneous plasma, the Alfvén wave velocity is given by:

$$v_A = (B^2/\mu_0\varrho_0)^{1/2} \tag{1.52}$$

where B is the magnetic field and ϱ_0 is the plasma mass density [43]. The characteristic time of wave propagation is defined as the Alfvén time:

$$\tau_A = R_0/v_A \tag{1.53}$$

where in this case R_0 is the initial radius of the plasma column.

Returning to the pinch dynamics, the *snowplow* model assumes the plasma as contained in a perfectly conducting, infinitely thin cylindrical shell which preserves its shape during the implosion. The gas contained within the cylinder is pushed inwards by a 'magnetic piston' which sweeps all the mass in front of it in the form of

a shockwave. The equation of motion of an imploding shell of radius R is:

$$M \frac{d^2R(t)}{dt^2} = \frac{\mu_0 I^2}{2\pi} \frac{1}{R(t)} \tag{1.54}$$

where M is the mass per unit length and R is the time-varying radius of the current sheet. Taking the initial conditions: $R(0) = R_0$ and $R'(0) = 0$, the solution to this differential equation at constant current I_{max} is:

$$\left(\frac{dR}{dt}\right)^2 = \frac{R_0^2}{\tau_A^2} \, 2ln\left(\frac{R_0}{R(t)}\right) \tag{1.55}$$

and

$$\frac{t}{\tau_A} = \left(\frac{\pi}{2}\right)^{1/2} erf\left\{\left[ln\left(\frac{R_0}{R(t)}\right)\right]^{1/2}\right\} \tag{1.56}$$

where time has been normalized to the Alfvén time τ_A. By approximating $R(t)/R_0 = 0.1$, which implies a radial compression to $1/10^{th}$ of its size, estimates of the implosion velocity and time can be calculated from Eqs. 1.55 and 1.56 [44]:

$$v_{imp} = \frac{dR}{dt} \approxeq 2\frac{R_0}{\tau_A} = \frac{2I_{max}}{\pi R_0}\left(\frac{\mu_0}{\varrho_0}\right)^{1/2} \tag{1.57}$$

$$\tau_{imp}^{sp} \approxeq \tau_A \left(\frac{\pi}{2}\right)^{1/2} = 2\frac{R_0^2}{I}\left(\frac{\varrho_0}{\mu_0}\right)^{1/2} \tag{1.58}$$

For instance, taking an aluminium plasma column of 3 mm at a density of 10^{14} cm^{-3} and a current of 1 kA gives: $v_{imp} \approx 10^5$ m/s and $\tau_{imp}^{sp} \approx 36$ ns. A more realistic time for implosion, however, is given when a steady current rate (dI/dt) is added to 1.58. Taking the current rate as a linear function of time $[I(t) = t(dI/dt)]$, the implosion time becomes:

$$\tau_{imp}^{t} = \left(\frac{\varrho_0}{\mu_0}\right)^{1/4}\left(\frac{2R_0^2}{dI/dt}\right)^{1/2} \tag{1.59}$$

which for a current rise of 10^9As^{-1} gives an implosion time of: $\tau_{imp}^{t} = 183$ ns. The snowplow model is perhaps the most simplistic, and although in many cases it

provides an adequate description of experimental results, it neglects various effects such as ionisation, shock formation and ohmic heating [45].

The slug model, developed by D. Potter utilises a hydrodynamic approach that treats the imploding system as a shock front which moves ahead of a thin, infinitely-conducting shell [46]. Is is also assumed that there exist a non-zero internal pressure P_0, which is much smaller than the shock pressure ($P_0 \ll P_s$). For a shock velocity $v_s = dR_s/dt$ normal to the plasma flow, the imploding shockwave will thus be described by the so-called Rankine-Hugoniot (R-H) conditions:

$$u_s = \frac{2}{\gamma + 1} v_s \tag{1.60}$$

$$\rho_s = \frac{\gamma + 1}{\gamma - 1} \rho_0 \tag{1.61}$$

$$P_s = \frac{2}{\gamma + 1} \rho_0 v_s^2 \tag{1.62}$$

where γ is the adiabatic constant and u_s, ρ_0 and P_s are the velocity, density and pressure of the fluid behind the shock. One can therefore assume a balance between the magnetic pressure (piston) and the pressure behind the shock (P_s), to wit:

$$\frac{\mu_0 I^2}{8\pi^2 R_p^2} = \frac{2}{\gamma + 1} \rho_0 v_s^2 \tag{1.63}$$

where R_p is the magnetic piston radius. Using the adiabatic law ($\gamma P dV = -V dP$) combined with the R-H conditions, an equation for constant current is solved, obtaining: $R_p = R_0 \left(\frac{\gamma}{\gamma + 1 - (R_s/R_p)^2} \right)^{\gamma/\gamma - 1}$. The final pinch radius R_{min} is obtained when $R_s/R_p \to 0$, therefore,

$$R_{min} = R_0 \left(\frac{\gamma}{\gamma - 1} \right)^{\gamma/\gamma - 1} \tag{1.64}$$

This means that for an adiabatic constant of $\gamma = 5/3$, the minimum radius is reached when $R_{min} = 0.3R_0$. Numerical solutions also provide the time required for the implosion, which is given by:

$$\tau_{imp}^{sl} = 0.38\frac{R_0^2}{I}\left(\frac{16\pi\rho_0}{\mu_0}\right)^{1/2} \tag{1.65}$$

Using the same plasma conditions as above (diameter of 3 mm; density of 10^{14} cm^{-3} and current of 1 kA), the final radius after implosion is estimated to be: $R_{min} \approx 1$ mm. The pinch time, on the other hand, is: $\tau_{impl}^{sl} = 45$ ns. This model also predicts the final density and temperature of the plasma at the axis of the column. Once again, taking $\gamma = 5/3$:

$$T_{max} = 0.032\frac{\mu_0 I^2}{k n_i R_0^2} \tag{1.66}$$

$$\rho_{max} = 16.4\rho_0 \tag{1.67}$$

which predicts a maximum temperature of $T_{max} = 280$ eV and density $\rho_{max} = 1.6 \times 10^{15}$ cm^{-3}.

Finally, the simplified MHD model assumes a finite plasma thickness, contained between the shock front and the magnetic piston, and is actually a semi-empirical fit to the snowplow and slug models. The shock front velocity is taken as the Alfvén velocity (Eq.1.52), whilst the shock propagation time from its initial radius R_0 to the axis is given by the Alfvén time (Eq.1.53). In this model, the plasma shock propagation time is coupled to the time constant of the discharge circuit, $t_c = \sqrt{LC}$, where C and L are the circuit capacitance and inductance respectively. The pinch time is therefore:

$$\tau_{imp}^{mhd} = k(\tau_A t_c)^{1/2} \tag{1.68}$$

where k is a semi-empirical parameter that depends on t_c/τ_A, and is estimated to be 1.5 and 0.8 for the snowplow and slug models respectively [47]. Under the plasma

conditions used previously (diameter of 3 mm; density of 10^{14} cm^{-3} and current of 1 kA), this gives respective pinch times of: $\tau_{imp}^{sp} = 140$ ns and $\tau_{imp}^{sl} = 74$ ns. In addition to these parameters, the MHD model can be used to estimate ohmic losses, and some prediction on the behaviour of lensing effects of a magnetic field for a stream of ions.

1.4.3 Equilibrium Dynamics and Instabilities

The possibility of using Z-pinches as a source of high-energy photon radiation is one of the driving factors in this work. Once a Z-pinch is formed, the main source of plasma heating will depend on conductivity (Joule heating is proportional to electron temperature via the Spitzer conductivity [48]), whilst, plasma cooling will be due to radiation losses. It is therefore said that a Z-pinch is stable when radiative losses equal resistive heating, whereby, the pinch radius will contract if radiative effects are greater than joule heating, and vice versa [44]. Furthermore, if this radiation loss far exceeds heating, an effect termed *radiation collapse* is said to occur. There is a critical current when this balance is predicted to occur which is called the *Pease-Braginski current* (I_{PB}). The derivation of I_{PB} is given by equating the Bremsstrahlung loss per pinch unit length (Eq. 1.69) and Joule heating (Eq. 1.70) [49]:

$$P_r = 1.69 \times 10^{-38} T^{1/2} \int 2\pi n^2 r dr \ [\mathrm{Wm}^{-1}] \tag{1.69}$$

$$E = 1.03 \times 10^{-4} (ln[\Lambda]) T^{-3/2} J_0 \ [\mathrm{Vm}^{-1}] \tag{1.70}$$

where T is the temperature [eV], J_0 is the axial current density and $ln[\Lambda]$ is the Coulomb logarithm. By setting $P_r = I_{PB}E$, the critical current is given by: $I_{PB} = 0.685\frac{\bar{Z}+1}{\bar{Z}}(\lambda ln[\Lambda/10])^{1/2}$ [MA] . Here $\bar{Z}$ is the mean ionisation and λ is a factor dependent on current density, temperature and number density; generally $\lambda \approx 1.$ In ideal circumstances, equilibrium should last considerably longer than radiative

losses and magnetic field diffusion. [44].

The transient nature of equilibrium is physically related to what are known as MHD instabilities. Although the mathematical treatment describing these instabilities is outside the scope of this work, one can think of these as analogous to the equilibrium points in a mechanical system, where a state is stable when in a potential trough and unstable when on a potential cusp [50]. Qualitatively, the problem arises at the boundary between the plasma and the **B**-field, where a so-called interchange instability occurs. As the self-magnetic field develops, it will constrict the plasma in certain regions. The walls of the column will begin to curve inwards, resulting in a non-uniform current density along the boundary, charge buildup and the formation of local electric fields that will enhance the disturbance. These disturbances are known as Kruskal-Schwartzchild instabilities, and are the MHD analog of the Rayleigh-Taylor instability in fluid mechanics.

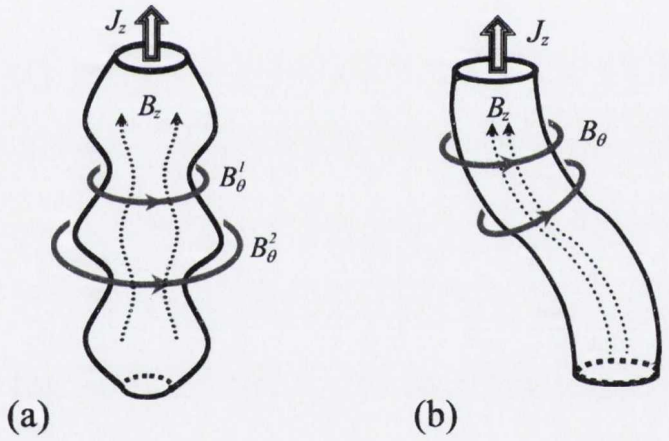

Figure 1.7: Sausage (a) and kink (b) instability in cylindrically-symmetric plasmas.

In the case of cylindrically-symmetric plasmas, one may have so-called *sausage* or *kink* instabilities. The former is a structure of contracted and expanded radii along the length of the column, whilst the latter is the development of a 'bend' in the plasma column (Fig. 1.7). Note that in both instability types the axial magnetic field (B_z) is non-zero. Furthermore, it is possible to stabilize these configurations

by adding an external magnetic field along the z-axis, which will create an internal pressure that diminishes the development of the perturbation.

1.5 Plasma Focusing

It has been of some interest in the field of high-energy physics to use plasma focusing devices, which rely on external magnetic fields to deflect charged particles. In this work, it is thought focusing may occur due to the self-magnetic azimuthal field produced by current flow within the expanding plasma; a possibility that is explored at the end of chapter three.

In the presence of a current carrying plasma, charged particles will enter a radial field similar to that of an axisymmetric lens [47]. For a uniform current density J within a conductor of radius R_p, the magnetic field will be given by:

$$B = \frac{\mu_0 I_p}{2\pi R_p} \tag{1.71}$$

The focusing strength of the lens will be given by: $K = G(e/p)$,where e is the electron charge, p the particle momentum and G is field gradient $G = \mu_0 J/2$. The phase ϕ is defined for a lens of length l as: $\phi = l\sqrt{K}$, which is used to determine the focal length given by:

$$f = \frac{1}{\sqrt{K} sin(\phi)} \tag{1.72}$$

If the incident ions have a divergence angle α, the current I_0 required to collect the beam will be given by:

$$I_0 = \frac{2\pi\alpha^2 p}{e\mu_0} \tag{1.73}$$

1.6 Summary

The main physical processes that will be encountered in the experiments herein have now been discussed. Since the laser produced plasma is the initial source of ions before the discharge onset, the physics of laser ablation gives a better understanding of the initial plasma conditions as discharging begins. Furthermore, spectroscopic analysis of the plasma is an effective method for measuring physical parameters, such as electron temperature and ion density, before and after the discharge. Finally, given the magnetohydrodynamic character of the experiments, where high currents are driven through the plasma, the effects of the induced magnetic field on plasma flow have also been discussed, with the possibility of encountering magnetic compression and/or pinching.

In the chapter that follows (*Chapter Two*), a description of the experimental setup is given, as well as the equipment and techniques used for analysis throughout this work.

Chapter 2

Experimental Methods

2.1 Discharge Cell Design

Three different discharge configurations were studied in this work, all in a coaxial geometry, where the main difference was in the shape of the outer electrode or 'collar'. The three collars used were an open-ended collar, a collar with interior conical cross section, and a collimating aperture. A BNC connector shell was adapted to the discharge electronics so all collars and inner electrode studs could be used interchangeably.

The open-ended collar (Fig. 2.1) was machined from aluminum, having a diameter of 1 cm and an overall length of 1.5 cm. Two diametrically opposing slits were cut into the sides, having a length of 1 cm and a width of 3 mm. These were implemented to allow optical access to the collar as well as the ablating laser pulse, which was focused onto the inner electrode surface at 45°.

The conical collar (Fig. 2.2) was dimensionally similar to the open design, with an overall exterior length of 1.5 cm and 1.2 cm diameter. This part was also machined from aluminum, with the inner-cone having a base diameter of 1 cm and a half-angle apex of 40° ending in a 3 mm orifice. The laser pulse was focused onto the inner electrode, passing through the orifice.

(a) (b)

Figure 2.1: Three-dimensional image (a) and dimensions (b) of the open collar geometry.

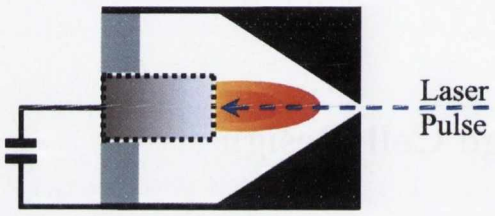

Figure 2.2: Conical collar

The third design (collimating aperture) was machined out of stainless steel, having an overall length of 1.5 cm and a diameter of 1 cm. Two rectangular windows (1.0 × 0.5 cm) were cut on opposing sides of the collar. The end of the cylinder was closed, having a 3 mm orifice in the center. The laser was focused on a rotating target placed at 1 cm from the aperture, which in turn acted as a collimator producing a thin plasma column inside the cell. Figure 2.3 shows a schematic of this collar.

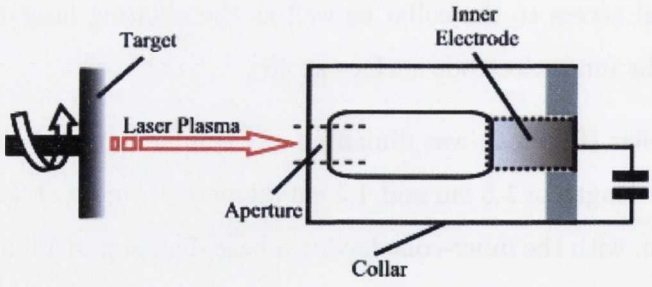

Figure 2.3: Discharge cell with collimating aperture.

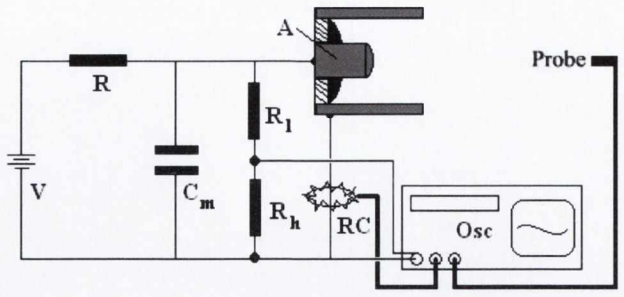

Figure 2.4: Discharge circuit. R-charging resistor; C_m-Capacitor; R_1, R_h-voltage divider; RC-Rogowski coil; A-inner electrode.

2.2 Experimental Setup

Using an Nd:YAG laser (λ= 1064 nm) with a pulse width of $\Delta\tau$ = 7 ns or an Excimer laser (λ= 248 nm; $\Delta\tau$ = 20 ns), triggering of the discharges was done by ablation of metal targets inside a vacuum chamber using different discharge cell configurations (described below). Chambers were pumped down using a roughing and turbo-molecular pump combination (Pfeifer TMH 071), working at a nominal pressure of 10^{-4} mbar. Inside the chamber was a self-contained metallic circuit box which consisted of a capacitor connected in series to the electrode leads and charged using a Glassman ER-1000 power supply with reversible polarity. Voltage was monitored using a voltage divider and current was measured using a Rogowski coil. The circuit schematic is shown in Fig.2.4.

Voltage and current monitoring were connected to a 300 MHz Tektronix TDS-3034B oscilloscope triggered with the laser pulse using a fast photodiode. Plasma charge density was monitored using an electrostatic probe also connected to the oscilloscope via a modified biased tee (Koopman) circuit. This probe could be charged positive to measure negative collected charge (electrons) or negative to measure the flux of positive charge (ions).

Two Andor (iStar DH734 and ICCD DH520) intensified charged coupled devices (ICCD's) were used to capture simultaneous time-resolved emission from the expanding plasma. One of these cameras captured optical emission in imaging mode

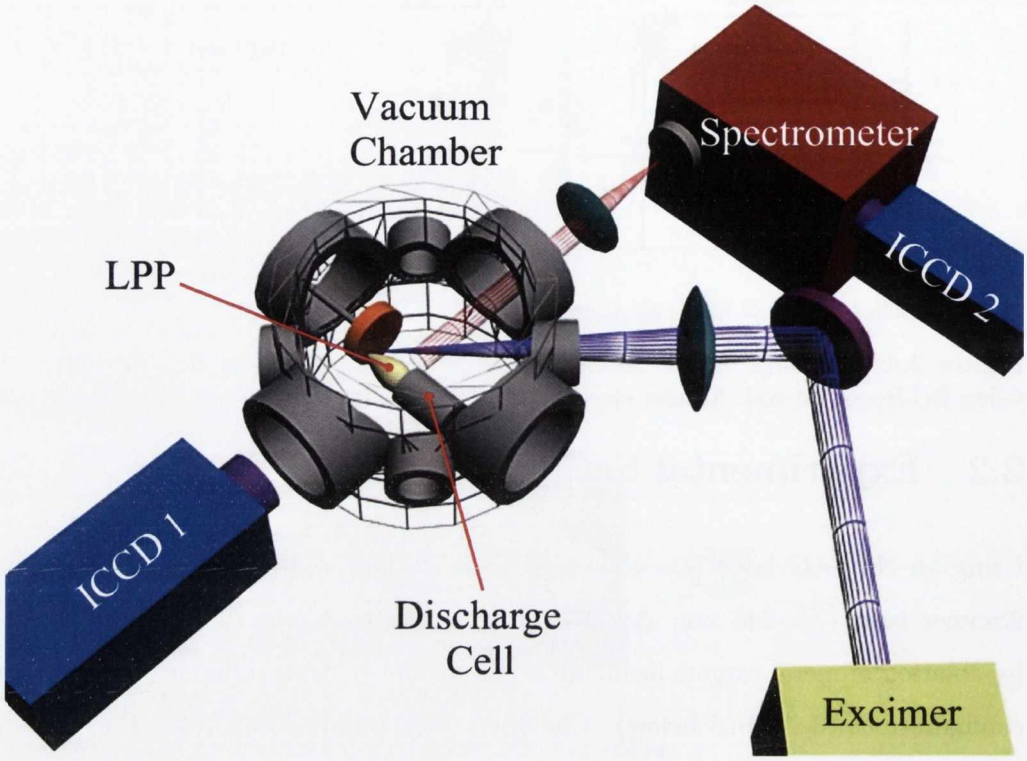

Figure 2.5: Experimental setup

via a 1:1 camera lens, whilst the other was attached to a 1/4 meter Czerny-Turner spectrometer (Oriel Cornerstone 260i) with selectable diffraction gratings (300, 600 and 1200 l/mm) and a spatial resolution of 50 μm. The Andor iStar has a minimum temporal gate of 3 ns whilst the ICCD's is of 5 ns. A schematic of the camera configuration is shown in Fig. 2.5.

Film depositions were also carried out for various tests whereby a glass or plastic substrate was placed normal to the plasma expansion. Thickness profiles from these films were extracted using an Epson Perfection V700 flatbed scanner operating in transmission mode. Mass loss was also determined for these experiments by weighing the targets before and after the depositions using a Mettler-Toledo precision micro-balance with a resolution of 20µg.

2.3 The Langmuir Probe

Electrostatic (Langmuir) probes are a tool often used for the analysis of laser produced plasmas. The Langmuir probe consists of an exposed metallic surface, usually cylindrical or planar, placed in the path of the plume. As a singly-ionised plasma enters the vicinity of the probe, a current will be drawn given by $I_i = Aen_iv_i$, where A is the probe area, n_i is the ion density and v_i the plasma flow velocity. However, in order for an ion current to be collected at the probe surface, the following condition must hold: $v_i \gg (kT_e/m_i)^{1/2}$, where the term on the RHS is known as the Bohm velocity v_B and arises from the formation of a so-called *plasma sheath*, commonly present at the boundary of a plasma. In general, although the plasma is quasi neutral, the high mobility of electrons with respect to ions will cause the surface of a boundary to become negatively charged, which will in turn produce an area of positive charge directly in front of the surface, having a thickness $x \approx \lambda_L$ [51]. In the stationary plasma case, due to the potential difference between the boundary and the plasma, ions will be accelerated towards the boundary in an area called pre-sheath, where presumably ions acquire the Bohm velocity cited above [52]. If the ion flow velocity is greater than the Bohm velocity by a significant margin, it can be assumed the current collected is due to the former. For instance, a plasma of aluminium ions at 1 eV will have a Bohm velocity of $v_B \approx 10^3$ ms^{-1}. It will be shown below that most of the ions in the plasma exceed this velocity by at least one order of magnitude.

By using a biasing circuit and connecting to an oscilloscope, plume charge collection as a function of time can be measured. Furthermore, by setting the appropriate bias (positive or negative) on the probe it is possible to detect either ions or electrons in the plasma plume. Figure 2.6(a-b) shows both an ion and an electron signal from an aluminum plasma plume set at $z = 30$ cm from the target. Because probes with different surface areas were used throughout these experiments, the signals will be expressed as charge per unit area, i.e. the ion or electron current j_i, j_e [mA cm^{-2}] .

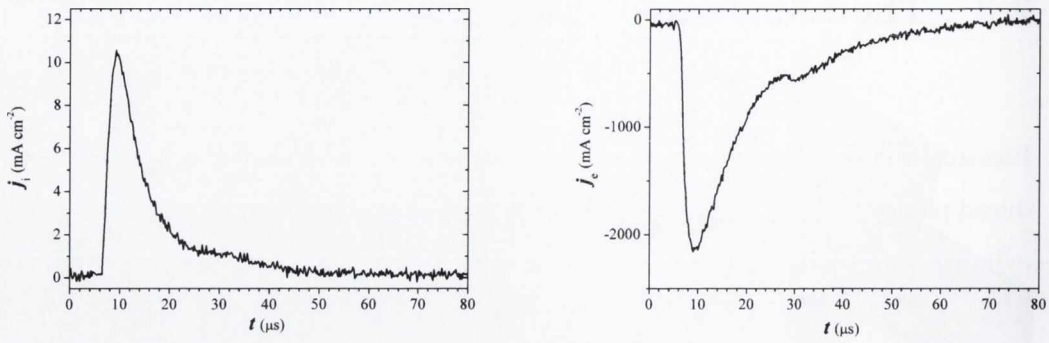

(a) (b)

Figure 2.6: Ion (a) and electron (b) signals from Langmuir probe; $z = 30$ *cm*.

2.3.1 Ion\Electron density and flux

As mentioned above, plasma in the vicinity of the probe will induce a current proportional to both the velocity and density of the ions. The general equation when a multiply ionised plasma is present is given by:

$$I_i = eAv\sum_j n_j Z_j \tag{2.1}$$

where A is the probe area, e the electron charge and v the ion velocity. Here, n_j is the ion density for a given ionisation state Z_j. This equation can therefore be used to estimate the ion density upon collection of a time dependent ion current, as the one shown in Fig. 2.6(a-b). For a singly-ionised plasma ($Z = 1$); solving for n_i, the equation becomes:

$$n_i = \frac{I_i}{eAv} \tag{2.2}$$

Therefore, the data in an ion probe signal can be converted from current to density by applying equation 2.2 to the dataset. For example, the signal shown in Fig. 2.6 can be plotted as a function of density, as seen in Fig. 2.7.

Whilst the ion density depends on plasma flow, i.e. the product of the ion time-of-flight times the current, the electron density is independent of plume velocity, being

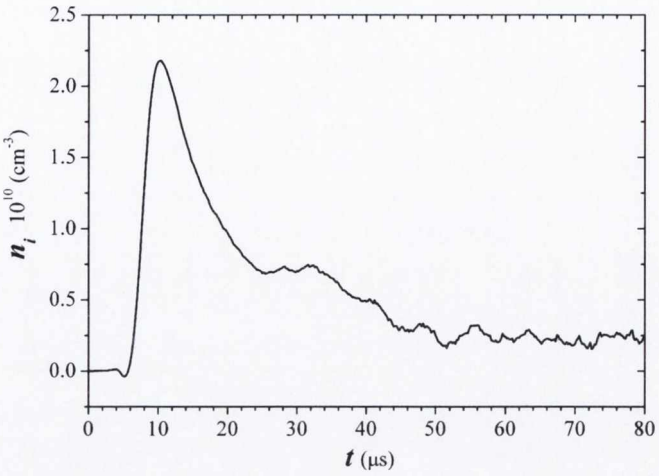

Figure 2.7: Ion density calculated from Langmuir probe signal shown in Fig. 2.6(a); $z = 30$ cm; $A = 0.2$ cm^{-2} .

solely determined by the electron thermal motion (i.e., the electron temperature T_e). As the bias of the probe is increased from detecting ions (negative bias) to electron detection (positive bias), a plot of the current induced by the plasma vs. voltage shows characteristic features of the plasma (Fig. 2.8 [53]). Increasing the bias voltage takes the current to a zero value, termed the floating potential (V_f), where both ion and electron currents are equal. Further bias increase brings the detection into the so-called electron retarding region, where in a Maxwellian energy distribution of electrons the current is given by: $I = I_e^{sat} exp\left(\frac{V-V_p}{kT_e}\right)$. Here, V_p is the plasma potential, which is the knee of the curve, and indicates a change in slope. Beyond the plasma potential is the electron saturation region I_e^{sat}, where electron signals are normally measured . This is given by:

$$I_e = \frac{1}{4} A e n_e c_e \tag{2.3}$$

where c_e is the electron thermal velocity in a Maxwellian distribution: $c_e = (8kT_e/\pi m_e)^{1/2}$.

An estimate of the number of ions per area (integrated flux F_i) as the plume expands can be determined from the probe signals using the following relation:

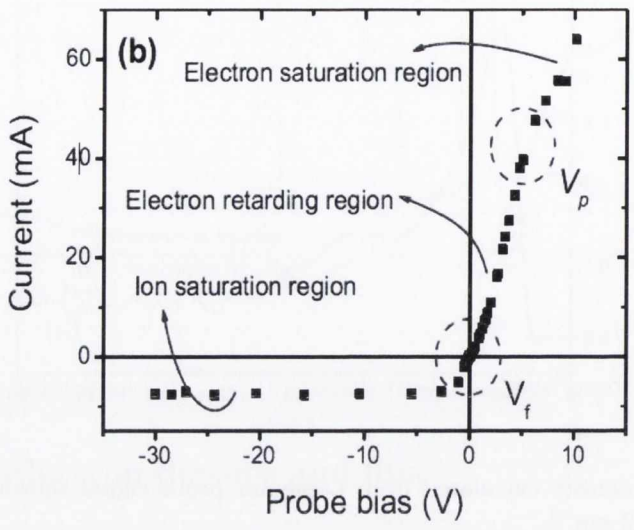

Figure 2.8: I-V characteristic of LPP with Langmuir probe.

$$F_i = \frac{1}{A} \int f(t)dt \tag{2.4}$$

where $f(t) = I(t)/e$. By integrating $f(t)$ one obtains the total number of charged particles, which divided by the probe area gives the integrated flux [ions cm^{-2}]. For instance, the signal shown in Fig. 2.6(a) gives a total integrated flux of $F_i = 6.5 \times 10^{13}$ cm^{-2}.

2.3.2 Ion Velocity and Energy Distributions

The velocity and energy distribution of ions contained in the plasma plume can also be inferred from the probe signals by plotting dN/dv vs. v or dN/dE vs. E. This can be derived from rewriting equation 2.4 as:

$$F_i = \frac{1}{e} \int I(t)dt = \int \frac{dN}{dv} dv = \int \frac{dN}{dE} dE. \tag{2.5}$$

Expressing the rightmost terms as time derivatives:

$$\frac{dN}{dv}dv = \frac{dN}{dv}\frac{dv}{dt}dt \tag{2.6}$$

$$\frac{dN}{dE}dE = \frac{dN}{dE}\frac{dE}{dt}dt \tag{2.7}$$

and taking $E = 1/2(mv^2)$ and $v = x/t$, gives the ion velocity and energy distributions [54]:

$$\frac{dN}{dv} = \frac{I(t)t^2}{ex} \tag{2.8}$$

and

$$\frac{dN}{dE} = \frac{I(t)t^3}{emx^2} \tag{2.9}$$

Plots of these distributions are shown in Fig. 2.9(a-b), where the ion currents are taken from Fig. 2.6(a) .

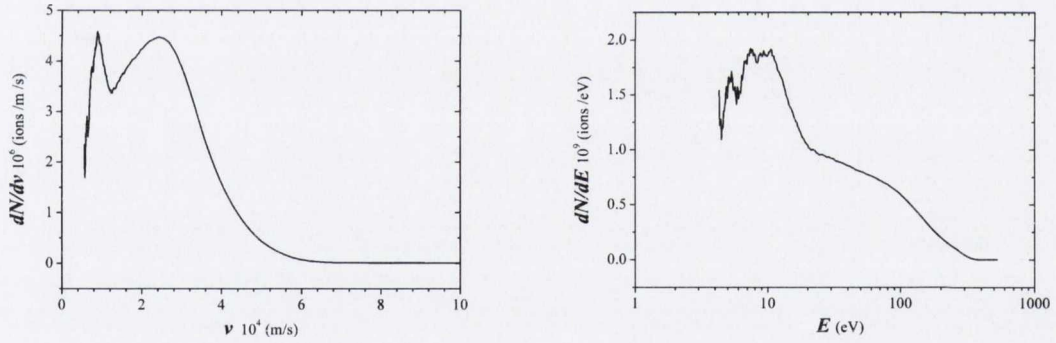

(a) (b)

Figure 2.9: Ion velocity (a) and energy (b) distributions derived from from Langmuir probe signal.

2.3.3 Self-Similar Expansion

The dynamics of the plasma expansion into vacuum predicted by the Anisimov theory establishes an acceleration phase during the first 50 - 100 ns after the laser

pulse (see section 1.1.4). Beyond this phase, the plume expansion becomes inertial and its shape will remain unchanged [18], a condition known as self-similarity. This entails that the plume flow variables such as velocity, density, temperature and pressure can be 'frozen' at any point in time and the resulting contour shape will not change [24]. This commonly implies a change of coordinates known as a self-similarity ansatz, which has the general form: $\xi = x/t$ or $\xi = x/X(t)$.

Regarding the present experiments, the above criterion suggests that even though the Langmuir probe is at a fixed distance from the target, the ion density profiles can be estimated at other distances by applying appropriate transforms to the original signal. The plasma flow velocity v_p is therefore equal at any arbitrary position z', with respect to the original probe position z_p. This implies $v_p = v'$, and hence, $z_p/t = z'/t'$. Therefore, the density at any distance z' having a temporal profile t' will be related to the probe distance z_p and temporal profile t, by the following transforms:

$$n_i(z_0, t') = n_p(z_p, t) \left(\frac{z_p}{z_0}\right)^3 \tag{2.10}$$

where

$$t' = t \left(\frac{z_0}{z_p}\right). \tag{2.11}$$

Recall Eq. 2.1, which is written in terms of the above notation for a singly-ionised plume:

$$I_i(t) = n_i(z_p, t) e A v \tag{2.12}$$

For instance, the signal shown in Fig. 2.6(a), was taken at a distance of 30 cm. Using Eqs. 2.11 and 2.10 an estimate of the density at 1 cm or 1 m are calculated and plotted in in Fig. 2.10.

Similar transforms can be applied to calculate the ion density as a function of dis-

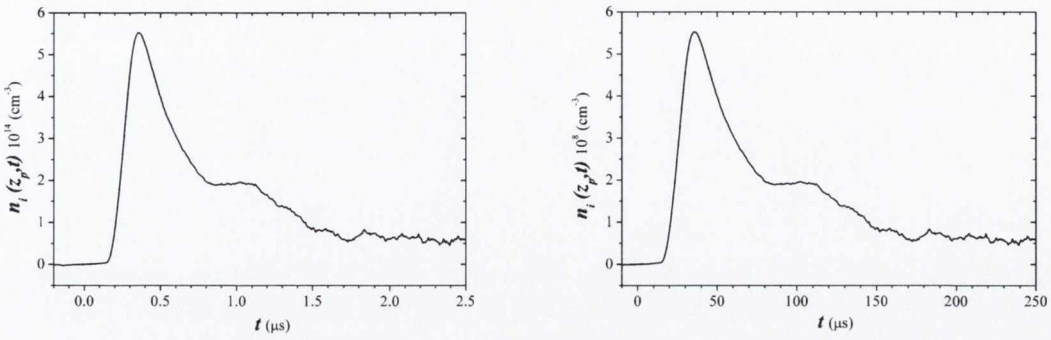

(a) (b)

Figure 2.10: Ion density estimates derived from Langmuir probe signals using self-similar theory. Distance from target is: (a) 1 cm; (b) 1 m.

tance $n_i(z', t_0)$ as well, to wit:

$$n_i(z', t_0) = n_i(z_p, t) \left(\frac{t_p}{t'}\right)^3 \tag{2.13}$$

where

$$z' = z_p \left(\frac{t_0}{t}\right). \tag{2.14}$$

Note that for these equations a suitable time t_0 should be chosen.

An example of density as a function of distance calculated from Eqs. 2.13 and 2.14 is shown in Fig. 2.11 for $t_0 = 500$ ns and $t_0 = 1$ μs.

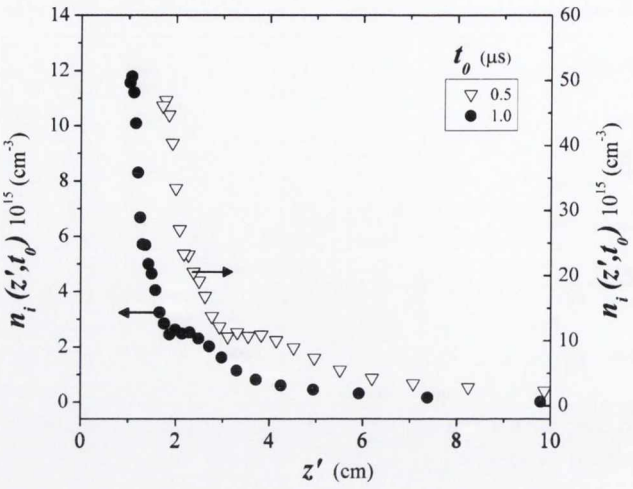

Figure 2.11: Ion density as a function of distance z' for $t_0 = 0.5$ *(right axis)* and 1.0 μs *(left axis)*.

2.4 Electric Discharge Analysis

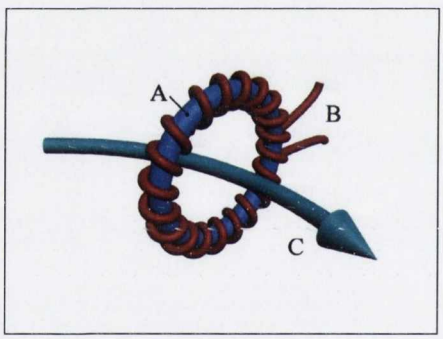

Figure 2.12: Rogowski coil: (A) Main loop; (B) Secondary winding; (C) Current-carrying conductor.

Current and voltage monitoring was achieved using a Rogowski coil and voltage divider respectively. As shown in Fig.2.4, the coil was placed around the lead going to the gun cathode, whilst the divider measured the voltage drop across the capacitor. Rogowski coils are a type of current-to-voltage transducer that collect all the current within a coiled loop following Ampere's Law (Fig. 2.12). They are easy to build and calibrate and are linear within a wide range of current values [55]. The output is a voltage signal proportional to the current: $-V = \alpha\,(dI/dt)$, where the constant $\alpha = (-AN\mu_0/l)$ is related to the coil characteristics. Here, A is the coil winding area, N the number of turns and l the coil length.

Once calibrated, the coil signal can be integrated via software or an integrating

circuit, rendering a signal of current as a function of time. Integrated and calibrated signals are shown in Fig. 2.13 along with their corresponding voltage values.

To determine whether these current and voltage signals were accurate, fits using the circuit simulation program PSpice were carried out. In order to consider factors such as plasma resistance and circuit inductance which contribute to signal oscillations and damping, extra elements were placed in the circuit to fit the signals; namely a series resistor R_s and series inductor L_s. The comparison of experimental and simulated signals are shown in Fig. 2.14.

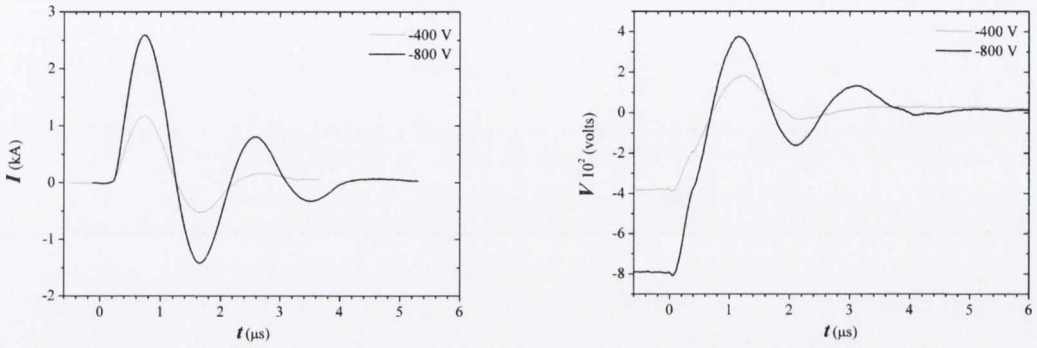

Figure 2.13: Discharge current (a) and voltage (b) signals for -400 and -800 volts.

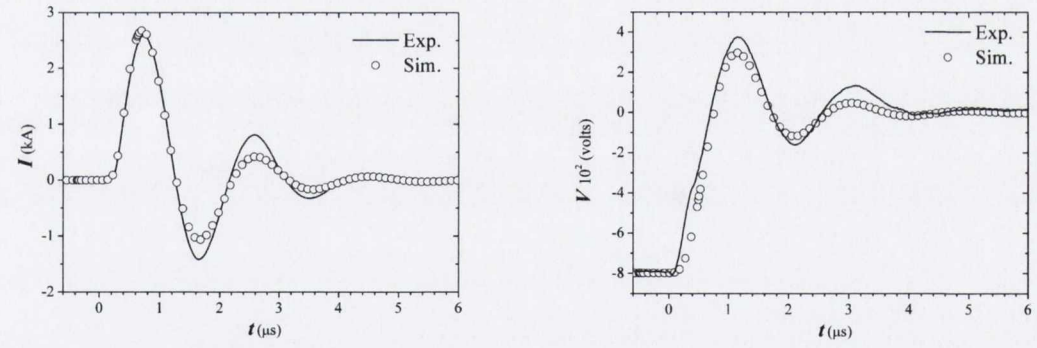

Figure 2.14: PSpice simulations of current (a) and voltage (b) compared to experimental results; -800 V. Simulation parameters: $R_s = 100$ mΩ and $L_s = 70$ nH.

The simulated signals were in good agreement with those obtained in the experiments, both in the peak I and V values and in the oscillatory character of the

signal. The equivalent values of inductance and resistance used were $R_s = 100$ mΩ and $L_s = 70$ nH respectively.

2.5 Spectrometer Resolution and Calibration

2.5.1 Spectral Resolution

The maximum spectral resolution of the spectrometer (Oriel Cornerstone 360) in these experiments can be determined in two ways:

1. The theoretical approach involves the calculation of the reciprocal linear dispersion of the spectrometer R_d [nm mm^{-1}] defined as:

$$R_d = \frac{d\lambda}{dx} = \frac{d\ cos(\beta)}{mf} \tag{2.15}$$

where d is the diffraction grating ruling separation, f the focal length of the spectrometer (250 mm), β the diffraction angle and m the diffraction order. Since only first-order diffr ction lines are considered ($m = 1$), and these occur at small angles ($10° - 20°$), equation 2.15 is approximated by: $R_d = d/f$. Therefore, given the 300 l/mm grating, the reciprocal dispersion is $R_d = 13.3$ nm mm^{-1}. To find the spectrometer resolution or bandpass, one need only use the relation:

$$B_p = WR_d \tag{2.16}$$

where W is the spectrometer slit width. The resolution using the 300 l/mm grating is then: $B_p = 0.66$ nm.

2. A second experimental approach involves the spectrometer's detector, which in this case is an ICCD with 1064 pixels across, each measuring 26 μm. Again, using equation 2.16, the dispersion is now determined by: $R_d = S/d_n$, where S is the spectral range and d_n is the number of detector elements. Because the active area of the spectrometer is slightly smaller than the detector (i.e., the

right and left edges of the detector are unused), a spectrally-calibrated image can be used. For instance, an image using the 300 l/mm grating has an active area of 655 px over a spectral range of 220 nm. This therefore gives a dispersion of: $R_d = 12.9$ nm mm^{-1} and therefore, a resolution of $B_p = 0.65$ nm. Both techniques are in good agreement.

2.5.2 Spatial Resolution

The smallest feature the spectrometer can measure spatially (seen on the X-axis of the spectral images) will depend on the magnification of the entire optical system, given by the product of the light delivery system $M_B = 3/20$ and the spectrometer $M_S = 1.6$. This means the total magnification will be: $M_T = 0.24$. Therefore, the image on the spectrometer ICCD of a feature 1 mm in size will be 240 μm. Given the pixel size of 25 μm, the resolution is actually: $\sim$10 μm per pixel. The spatial features analysed in this work, however, are not in the sub-millimetre range, and this resolution factor is used only for scaling purposes.

2.5.3 Spectral Line Irradiance Calibration

The absolute value of spectral line radiance will depend on various factors, such as the throughput of the light collection system (apertures, mirrors and lenses), the spectrometer (width of the slit and diffraction grating), and the settings of the ICCD/MCP. Indeed, as light impinges on the ICCD, the number of counts read from a single pixel will depend on the MCP gain and gate time, as well as the number of accumulations of a given experimental run. By using a source of known irradiance across the wavelength band of interest, an absolute calibration can be achieved which will include all the above factors and give an absolute radiance value for the acquired spectra. To this end, a 100 W quartz halogen lamp (Oriel 6333) was used to calibrate the system. This source has a characterised irradiance when placed at a distance of 50 cm from the imaging plane, where it produces a uniform flux

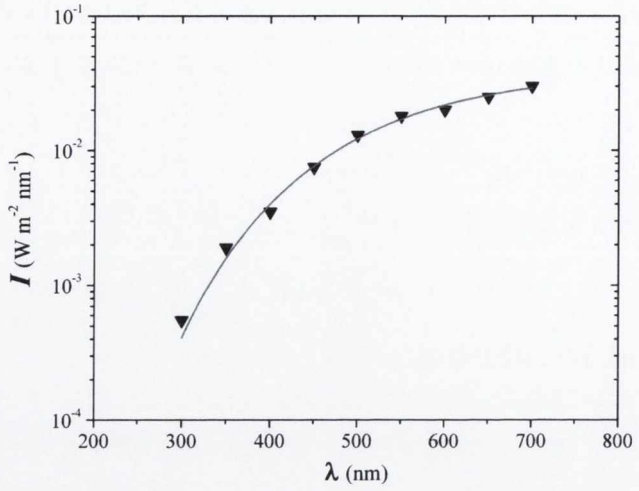

Figure 2.15: Fit of Oriel lamp data using blackbody equation.

density over a 2.5 cm × 2.5 cm area. Therefore the number of counts C_L detected on the ICCD from the lamp output can be expressed as:

$$C_L(\lambda) = F(\lambda) \cdot I_L(\lambda) \cdot n_L^{Aq} \cdot n_L^{Px} \cdot \Delta t_L \tag{2.17}$$

where n_L^{Aq} is the number of acquisitions, n_L^{Px} the number of pixels binned, Δt_L is the gate time and $I_L(\lambda)$ is the spectral irradiance of the lamp. $F(\lambda)$ is a function introduced to account for the multiple variables in the optical path and detection system mentioned above. The lamp spectral irradiance $I(\lambda)$ [W · m^{-2} · nm^{-1}] is given by the blackbody radiation equation as:

$$I_L(\lambda) = A_f \cdot 10^{-9} \left(\frac{2\pi hc^2}{\lambda^5} \right) \frac{1}{e^{hc/\lambda k T_B} - 1} \tag{2.18}$$

here, h is Planck's constant, c is the speed of light, λ is the wavelength and T_B the blackbody temperature. The free parameter A_f is used along with the blackbody temperature T_B to fit Eq. 2.18 to the tabulated data found in the lamp manual (Fig. 2.15). These were found to be: $A_f = (7.6 \times 10^{-6} \pm 1.1 \times 10^{-6})$ and $T_B = (3226.8 \pm 64)$ K.

Thus, one finds the value of $I_L(\lambda)$ that fits the data provided by the manufacturer.

Similar to Eq. 2.17 the spectral radiance of the plasma will be related to the counts on the ICCD by:

$$C_P(\lambda) = F(\lambda) \cdot I_P(\lambda) \cdot n_P^{Aq} \cdot n_P^{Px} \cdot \Delta t_P \tag{2.19}$$

Once again, $F(\lambda)$ is the function common to the optical system, given that the light collected from both sources (plasma and lamp) goes through the exact same optical elements. Therefore, solving Eq. 2.19 for $I_P(\lambda)$ [$\mathrm{W \cdot m^{-2} \cdot nm^{-1}}$], the plasma irradiance is:

$$I_P(\lambda) = \frac{C_P(\lambda)}{F(\lambda) \cdot n_P^{Aq} \cdot n_P^{Px} \cdot \Delta t_P} \tag{2.20}$$

Solving for $F(\lambda)$ in Eq. 2.17 and substituting in Eq. 2.20:

$$I_P(\lambda) = \frac{C_P(\lambda) \cdot I_L(\lambda) \cdot n_L^{Aq} \cdot n_L^{Px} \cdot \Delta t_L}{C_L(\lambda) \cdot n_P^{Aq} \cdot n_P^{Px} \cdot \Delta t_P} \tag{2.21}$$

Recalling the plasma radiance $L_P(\lambda)$ [$\mathrm{W \cdot m^{-2} \cdot nm^{-1} \cdot sr^{-1}}$] as the irradiance $I_P(\lambda)$ per unit solid angle Ω:

$$L_P(\lambda) = \frac{I_P(\lambda)}{\Omega}. \tag{2.22}$$

The angle subtended by the beam collection system is given by $\theta = tan^{-1}(r/x)$ where r is the lens radius and x is the distance from the plasma to the lens.

As an additional note, spectrometers generally have a so-called acceptance angle or cone, i.e. the angle at which all light will enter the apparatus. The Oriel Cornerstone 260 spectrometer has an acceptance half-angle of $\theta_s = 7.4°$ In order to collect the greatest amount of light from a source with the maximum spectral range, the delivery lens solid angle should match this acceptance cone. In this work, the half-angle impinging on the spectrometer slit after the light collection system is: $\theta_c = 6.2°$. Therefore, the spectrometer will be slightly under-filled.

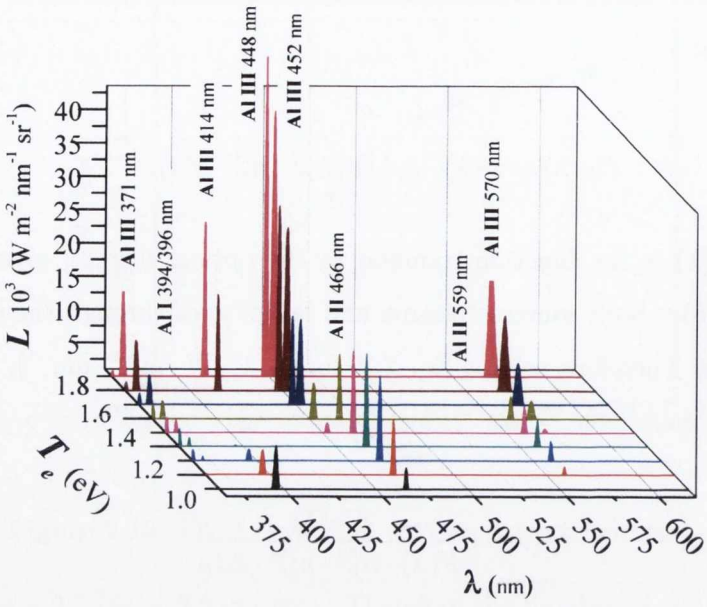

Figure 2.16: PrismSPECT Al spectrum sequence using 0.1 eV increments for constant ion density; $n_i = 10^{16} cm^{-3}$.

2.6 PrismSPECT: Emission Spectrum Simulations

The collisional-radiative simulation software PrismSPECT® made by Prism Computational Science Inc. is a very useful tool for interpreting spectroscopic data obtained in spectroscopy experiments. The software allows the user to simulate a wide array of elements from the periodic table, including multi-element plasmas with given relative compositions. By establishing a plasma thickness, electron temperature and ion density, lines can be obtained, which include the full set of transitions. It also resolves the mean plasma ionisation, ion fractions and electron density. Simulations can be run for both LTE and non-LTE cases. Figure 2.16 shows an example of a sequence taken at increasing electron temperature and constant ion density for aluminum lines.

From this sequence one can infer how plasma ionisation changes with electron temperature. From 1.0 eV to 1.2 eV the neutral Al 396 line radiance decreases. As temperature is increased further, the 466 nm and 559 nm Al II lines increase in ra-

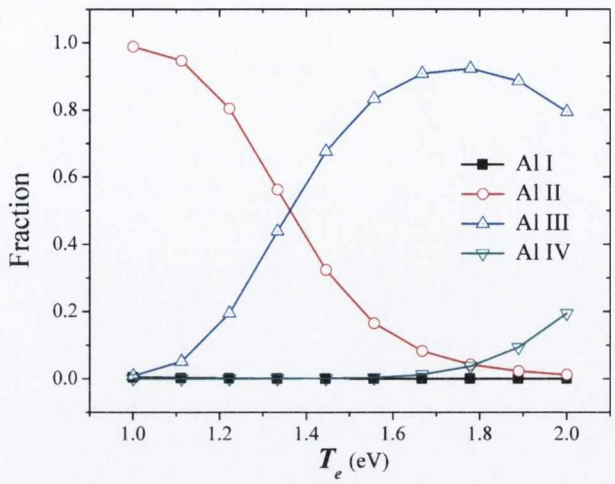

Figure 2.17: Ion fraction as a function of temperature for an Al plasma; $n_i = 10^{16} cm^{-3}$

diance, being most intense around 1.3 eV. The same trend is observed approaching 1.6 eV, where Al II lines begin to give way to Al III lines seen at 414, 448, 452 and 570 nm (see section 3.4 for energy level diagram).

It should be noted that the software occasionally shows unexpected behaviour. For instance, the 452 nm Al III line increases in intensity as the temperature rises from 1.4 eV, yet, between 1.6 and 1.8 eV, the 448 nm line suddenly appears beside it. Although a gradual appearance of this line would be expected, this effect was present no mater how small the temperature steps were set in the simulation. This will be addressed with the software manufacturer in due course.

The population of relative ion species is another feature of the software, and can be plotted as a function of electron temperature or ion density. An example for varying T_e is shown in Fig. 2.17.

As the electron temperature rises there are approximately equal populations of Al II and Al III at ~1.35 eV. Subsequently, as the singly-ionised species die out, the fraction of Al III reaches almost 100%, whilst the Al IV fraction begins to rise as well. Conversely, it is also possible to find how spectral lines behave with changing ion density at constant temperature; such a plot is shown in Fig. 2.18.

The prominent lines in the spectra of Fig. 2.18 are all Al III lines (370, 414, 448, 452

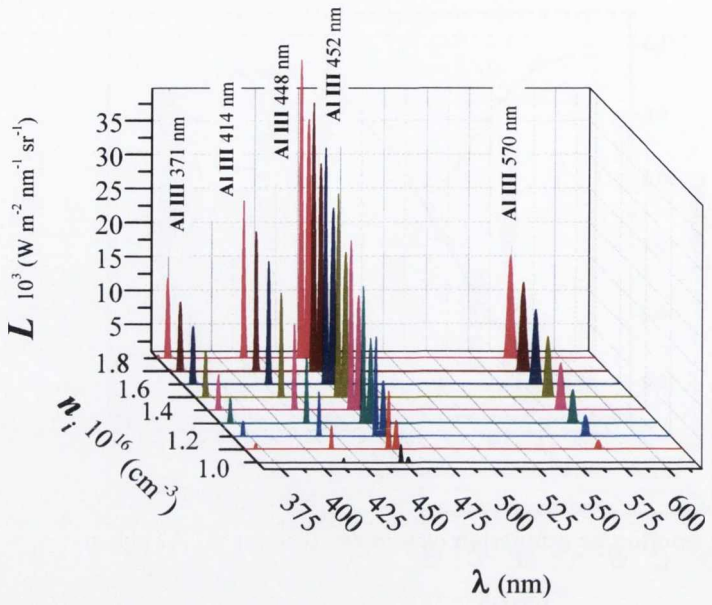

Figure 2.18: PrismSPECT Al spectrum sequence using $10^{15} cm^{-1}$ increments for constant electron temperature; $T_e = 2\,eV$.

and 570 nm) and increase in radiance with rising density. Note that as per Boltzmann's distribution, the line intensity ratios remain constant for a fixed temperature (cf. Eq. 1.27). Again, plotting the relative ion-state populations for changing ion density, this is indeed the case (Fig. 2.19). As the density increases, the fraction of Al III ions increases, whereas the Al IV species decrease. Although no Al IV lines are observed in the spectra presented here, it is likely these are found in the UV spectral range.

By comparing an absolutely-calibrated spectrum obtained experimentally with the output in PrismSPECT, plasma parameters, such as ion/electron density, temperature and mean ionisation can be extracted for a wide variety of plasmas, including the low temperature, high density plasmas produced in laser ablation. However, a perfect match is not always possible, since it is often the case that certain transitions are not present in the software model. This issue can be averted by changing to a different spectral range or target material.

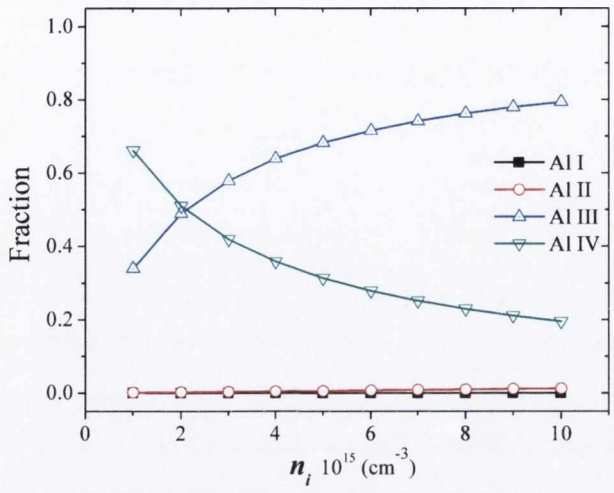

Figure 2.19: Ion fraction as a function of density for an Al plasma; $T_e = 2\,eV$

2.7 Energy Spectrum Analysis

In order to identify the ion species in the laser produced plasma plume as well as those formed during the discharge, the coaxial plasma gun setup was taken to the Atomic and Molecular Physics labs in University College Dublin. This group has an electrostatic energy spectrum analyser (ESA), which is normally used to study highly ionised laser plasmas.

There have been numerous plasma studies using this experimental technique, and a research area that benefits greatly from the use of energy analysers is the study of plasmas for extreme ultraviolet (EUV) sources. Highly energetic plasmas, where charge states between 8^+ and 13^+ are needed, can be produced by tightly-focused laser ablation. Emission in the 13.5 nm transition bands has been reported using materials such as Sn and Xe[1] [56, 57]. Another technique involves the use of fast electric discharges that produce a pinch in the plasma, emitting EUV radiation due to MHD constriction [58]. ESAs may be used as analytical tools as well, where unknown elements or contaminants are present in the target and need to be identified

[1]This is known as an unresolved transition array (UTA); present in high-Z atoms. Millions of individual lines combine to emit in the EUV spectral range.

[59].

Energy spectrum analysers belong to the broad family of mass spectrometers; these are instruments that use electric and/or magnetic fields to separate charged particles based on their charge-to-mass ratio. Other types of mass spectrometers include sector field, quadrupole, time of flight and Fourier transform cyclotron analysers. The field, whether electrostatic or magnetic, acts as a filter that only lets particles with a certain mass and charge through, in other words, it disperses ions towards a given angle to be collected by a detector. Many devices also work in tandem, using a first system to separate the ions followed by a second that focuses them onto the detecting medium. The detectors used also vary in sensitivity and sophistication, and can range from a simple photographic plate or Faraday cup to a Channeltron®, a microchannel plate (MCP) or a photomultiplier tube [60].

Experiments at UCD were done using a Comstock AC-902b spherical sector electrostatic energy analyser with a microchannel plate detector. Two separate chambers at a nominal vacuum of 10^{-5} mbar were used for this experiment, where a bell chamber was used to set up the plasma gun, whilst a second dedicated chamber contained the analyser which was set at a distance of 1.4 m from the gun via an 80 cm beam line. An ion probe was placed in the path of the plasma at 40 cm from the cathode and $\sim 10°$ with respect to the expansion axis. An Nd:YAG (λ = 1064 nm) was used to trigger the discharge. A schematic of the experiment is shown in Fig. 2.20. Signals from the ESA detector, ion probe and Rogowski coil were monitored simultaneously using a 1 GHz, 4-channel digital oscilloscope (Agilent Infiniium DSO8104A), triggered using a photodiode.

The ESA used in this experiment was an electrostatic analyser, having two spherical section parallel plates, one concave, and the other, convex (see Fig. 2.21). The device was used in time-of-flight mode, where a constant electric field is set between the plates and only ions meeting the following criteria can pass through to the detector:

$$\frac{E}{q} = \frac{\Delta V}{R} \tag{2.23}$$

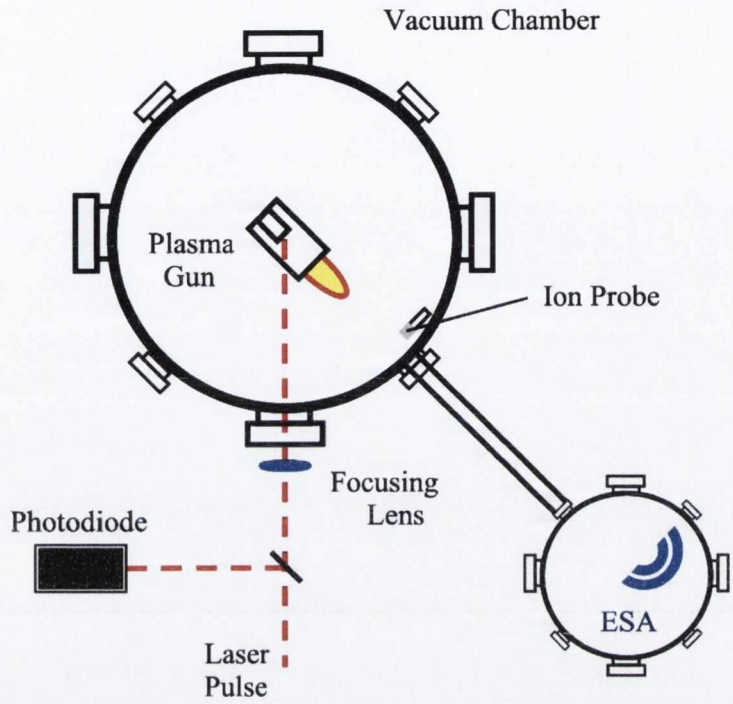

Figure 2.20: Experimental setup for energy spectrum analysis

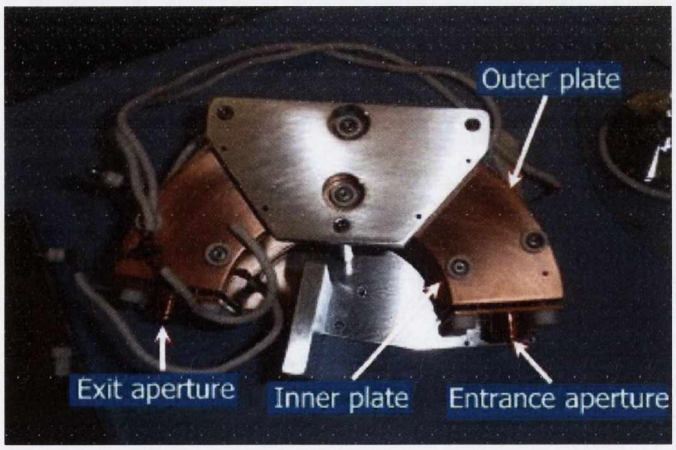

Figure 2.21: Spherical sector electrostatic energy analyser

where E is the ion energy, ΔV is the parallel plate potential difference and R is related to the inner and outer plate radii (r_1, r_2) by: $R = \frac{r_2}{r_1} - \frac{r_1}{r_2}$. Once an ion enters the analyser, the set potential across the plates will turn it 166° and it will arrive at the detector if it meets the above criteria. Otherwise, if the ion has insufficient energy, it will move towards the inner plate, whilst ions with too much energy will strike the outer plate. One may also derive the expected time-of-flight of specific ions from the kinetic energy equation, to wit:

$$E = \frac{1}{2}mv^2 = \frac{1}{2}m\left(\frac{x}{t}\right)^2 \tag{2.24}$$

which gives the time-of-flight (t_f) by solving for t:

$$t = t_f = x\sqrt{\frac{m}{2E}}; \tag{2.25}$$

here, m is the ion mass, and x is the distance from the source to the detector. The output of the energy analyser is a series of peaks in the time domain, each related to a specific ion and charge state. By triggering the oscilloscope with the arrival of the laser on the target, these peaks can be identified by using equations 2.23 and 2.25.

2.7.1 ESA Error Analysis

It should be noted that the error in time of flight increases with time. This is due to the voltage jitter in the power supplies used to maintain the potential across the plates, which was measured to be $\Delta V = \pm 5$ V. The associated error is derived from Eq. 2.23,

$$\Delta E = \frac{q}{R}\Delta V; \tag{2.26}$$

differentiation of the ion kinetic energy (Eq. 2.24) gives:

$$\Delta t_f = \frac{t^3}{mx^2}\Delta E. \tag{2.27}$$

Substituting Eq. 2.26 in Eq. 2.27 gives the time of flight error (Δt_f) as a function of time:

$$\Delta t_f = \frac{qt^3}{Rmx^2}\Delta V. \tag{2.28}$$

As the above equation suggests, the error will depend on the ion species being analysed. The plot in figure 2.22 shows the expected time of flight errors for Al I, II and III ion species.

The energy resolution of the analyser is related to its physical parameters, such as the electrostatic plate radius term R, input aperture ω, the angle subtended by the analyser ϕ, as well as the path length L. The resolution is, therefore, given by [61]:

$$\begin{aligned} \frac{\Delta E}{E} &\approx \frac{\omega}{R(1-cos(\phi)) + Lsin(\phi)} \\ &\approx 4.5\% \end{aligned} \tag{2.29}$$

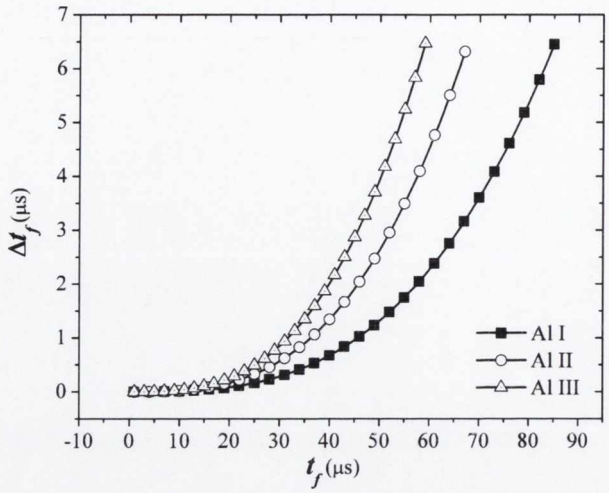

Figure 2.22: Time of flight error for Al I-III ion species due to power supply jitter (ΔV = 5 V).

Chapter 3

Open-Ended Collar Geometry

Discharges ranging from 0 to 1 kV were studied in this geometry using aluminium and copper cathode targets. Excimer laser pulses were focused down to a 1×2 mm spot with an energy of 80 mJ, giving a fluence of 4 J cm^{-2}. ICCD imaging and spectroscopy as well as various ion probe measurements were used to study the plume, and ion energy spectrum analysis was carried out to determine the ionic composition of the plasma. The results are discussed below.

Figure 3.1: Digital camera photos of open-ended collar showing initial ablation plume (left) and -800 V discharge (right).

3.1 The Discharge

Current and voltage were monitored for each event, recording the signals from the potential drop of the capacitor and the current delivered to the cathode using an oscilloscope (see Section 2.2). Figures 3.2 and 3.3 show the processed signals for voltage and current respectively, for changing discharge potential.

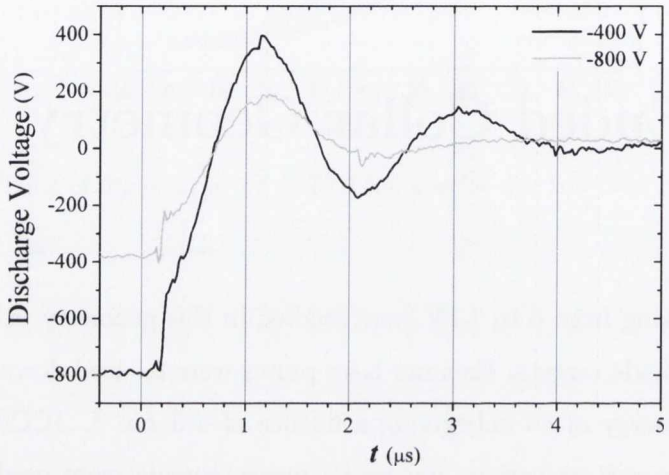

Figure 3.2: Voltage signals for -400 and -800 V discharge potentials; Al cathode.

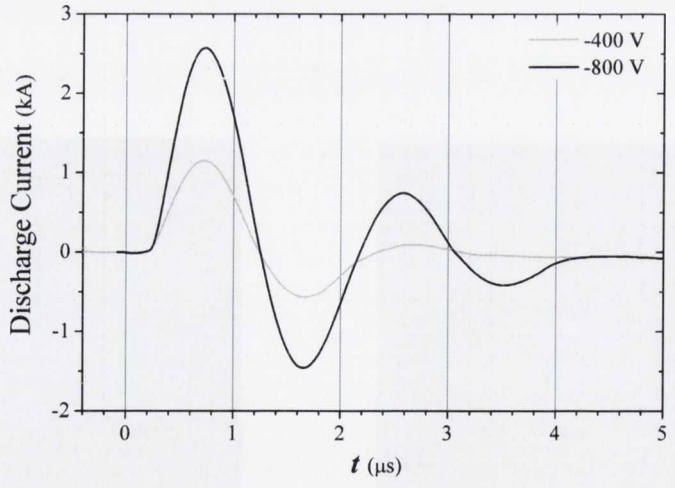

Figure 3.3: Current signals for -400 and -800 V discharge potentials; Al cathode.

From the time the laser strikes the target (time zero measured with the photodiode), the voltage and current signals begin after 200 ns, having a damped oscillation character with a period $T = 2$ μs; this is due to the inherent circuit inductance ($\sim$65 nH). The voltage crosses zero at 700 ns, which is the same time the current reaches its maximum value. The potential is then reversed and the current begins to decrease, reaching zero as the voltage peaks in the reverse polarity at 1.2 μs.

3.2 Ion Probe

For the open geometry experiments reported herein, Langmuir probe measurements were taken at 30 cm from the target, having a potential of -30 V and +15 V for ions and electrons respectively. A large distance ($\sim$ 30 cm) was maintained between the probe and the target to avoid electric pickup from the discharge. In most cases, both ion and electron signals were recorded simultaneously during each discharge event by using two probes. Figures 3.4 and 3.5 show the respective ion and electron signals at various discharge potentials for a copper target.

When no voltage is present, the normal ablation signals are seen, having a maximum around 10 μs. As the discharge voltage is increased, a second peak begins to form, evident at 20μs at low voltages. Further increase in the discharge potential causes this second peak to move to earlier times and a third peak seems to emerge from the second, although the original signal remains almost constant throughout. By way of comparison, probe signals are shown using an aluminium cathode in Figs. 3.6 and 3.7; for 0, -400 and -800 volts. A similar tendency to that of copper is evident, with multiple peaks appearing as the discharge ensues. The time of arrival of the plasma plume to the probe is practically the same for both metals ($\sim$7 μs), however, the aluminium plasma seems to propagate faster with the discharge. For instance, at -800 V discharge, the first peak arrives $\sim$4 μs earlier. This is likely due to factors related to each material, such as ion mass, ionisation potential, surface reflectivity and melting point.

Taking the ion signals for aluminium (Fig. 3.6), velocity and energy distributions can be estimated, as detailed in Section 2.3. Figures 3.8 and 3.9 show plots of $\mathrm{d}N/\mathrm{d}v$ vs. v and $\mathrm{d}N/\mathrm{d}E$ vs. E for varying discharge conditions.

As the discharge current increases, the ion velocity and energy distributions shift to higher values. It is noteworthy that the distributions at higher voltages exhibit strong single or multiple peaks, an effect consistent throughout the experiments, regardless of material.

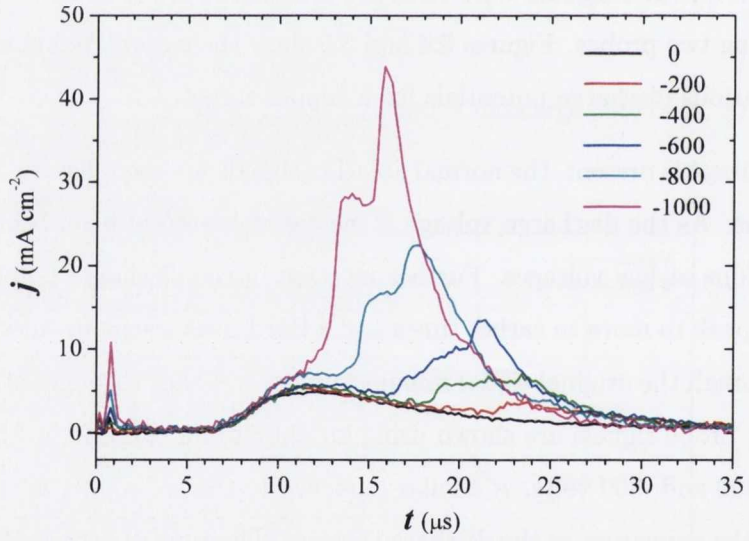

Figure 3.4: Ion signals for varying discharge potentials; Cu cathode.

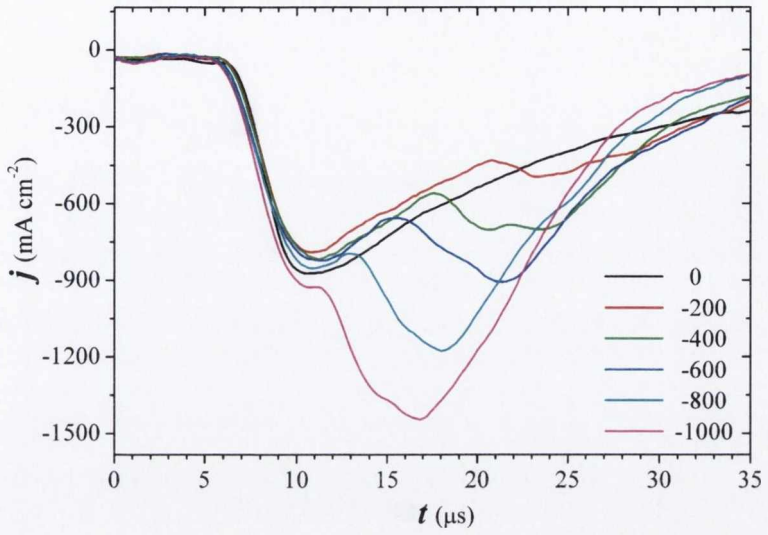

Figure 3.5: Electron signals for varying discharge potentials; Cu cathode.

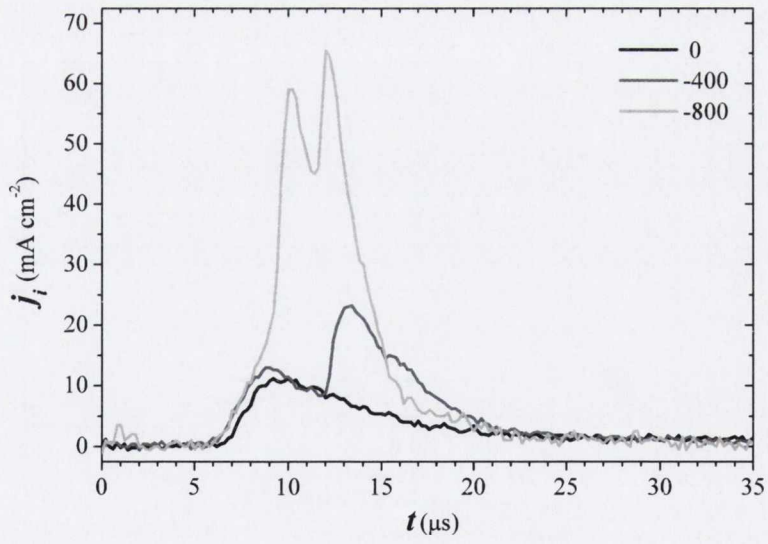

Figure 3.6: Ion signals for varying discharge potentials; Al cathode.

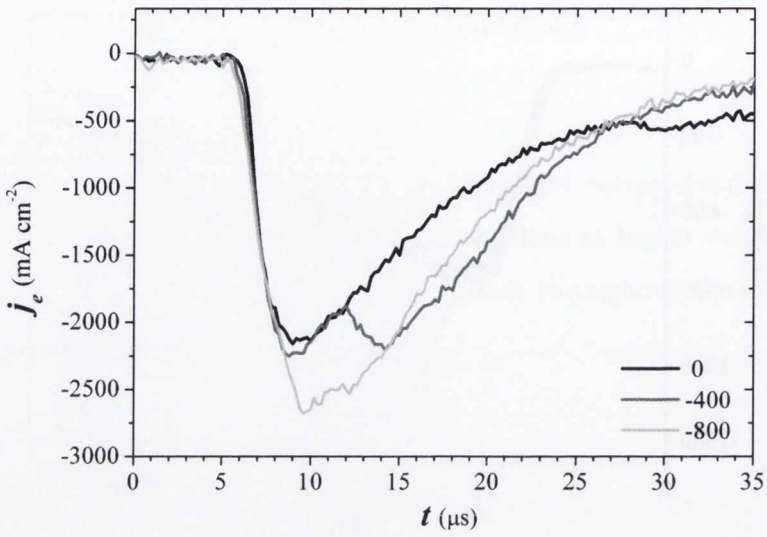

Figure 3.7: Electron signals for varying discharge potentials; Al cathode.

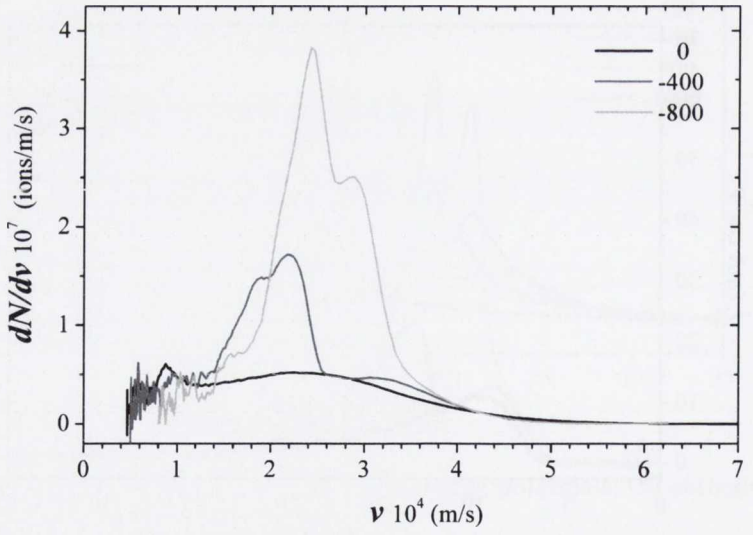

Figure 3.8: Velocity distribution taken from ion probe signals (Fig. 3.6) for varying discharge potentials; Al cathode.

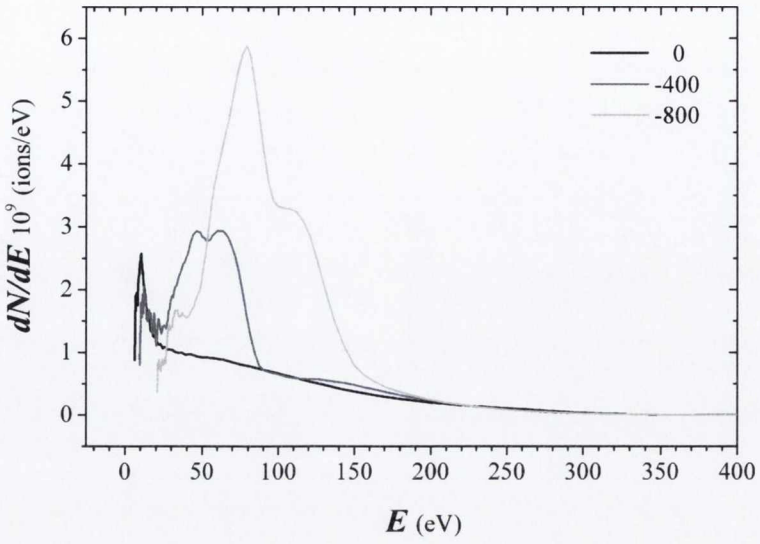

Figure 3.9: Energy distribution taken from ion probe signals (Fig. 3.6) for varying discharge potentials; Al cathode.

3.3 ICCD Imaging

Images of plasma emission were taken at various time delays from the onset of the laser pulse. Delay-times (τ) were taken in 200 ns steps, ranging from zero up to 4 μs (this number varied, depending on plume duration). The intensifier gate time was $\Delta t_g = 50$ ns. A comparison of the plume expansion with and without a -400 V discharge is shown in Figs. 3.10 and 3.11 as a time-resolved sequence. Special note should be made on the ICCD camera *gain*, which varies from 0 to 255. Turning up the gain produces an exponential increase in photoelectrons along the MCP channel, increasing the measured emission at the detector [62]. Although this number wasn't quantified (i.e. the images are not normalized for irradiance), higher gain values were used to increase image intensity when the plasma had low emission. For instance, the LPP (left column, Fig. 3.10) decreases in irradiance as time progresses, starting with very intense emission at early times and falling rapidly in emission thereafter. Gain was therefore increased from 0 to 200 with increasing time delay Δt. Conversely, in the case where a -400 V discharge was applied, irradiance remains steady for longer delays times, and therefore, gain was kept constant at 150.

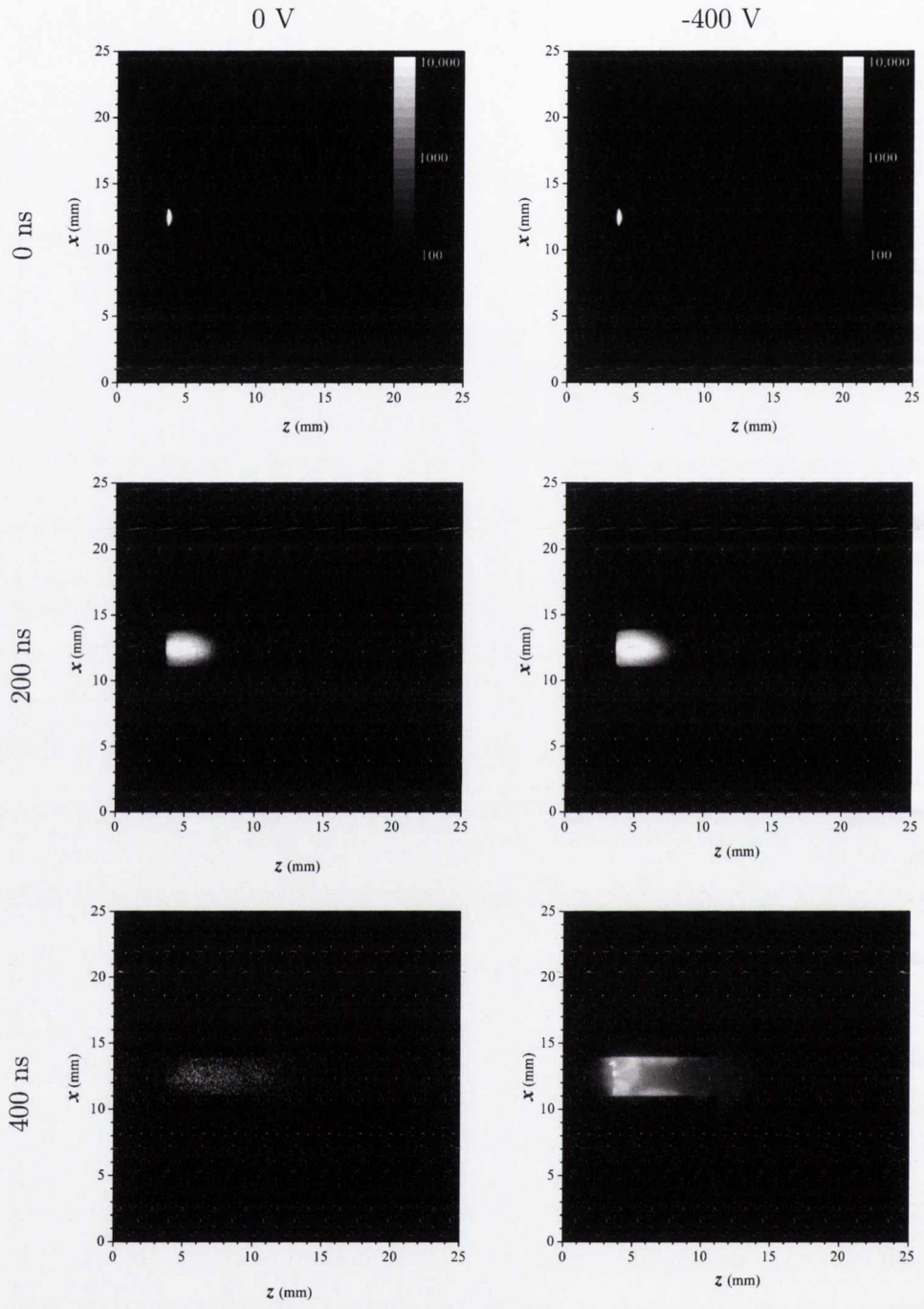

Figure 3.10: Time-resolved image sequence comparing 0 and -400 V discharge potentials. ICCD gate width $\tau = 50ns$. See text for notes on gain. (Intensity scale is logarithmic)

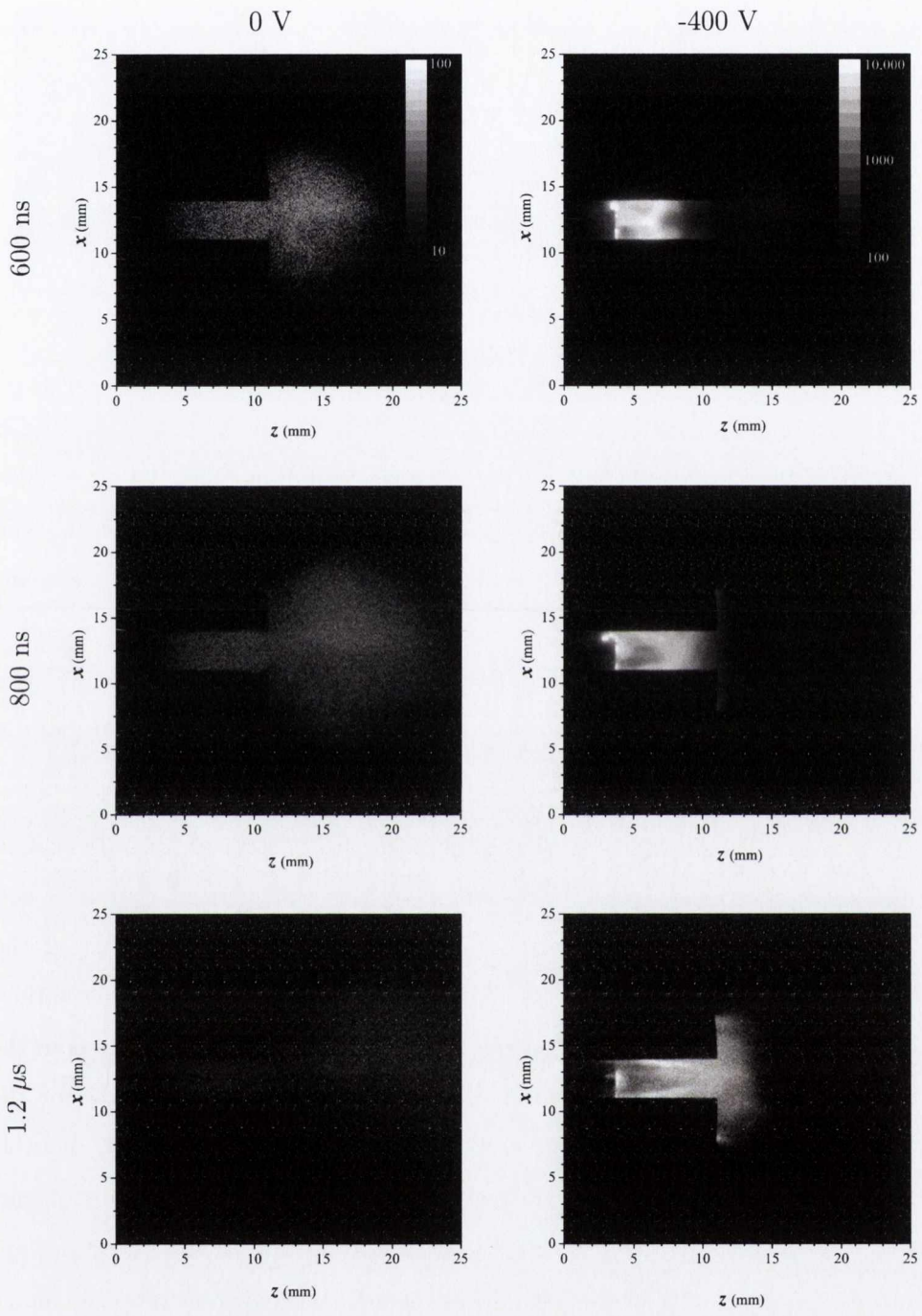

Figure 3.11: Time-resolved image sequence comparing 0 and -400 V discharge potentials; $\tau = 50ns$. See text for notes on gain. (Intensity scale is logarithmic)

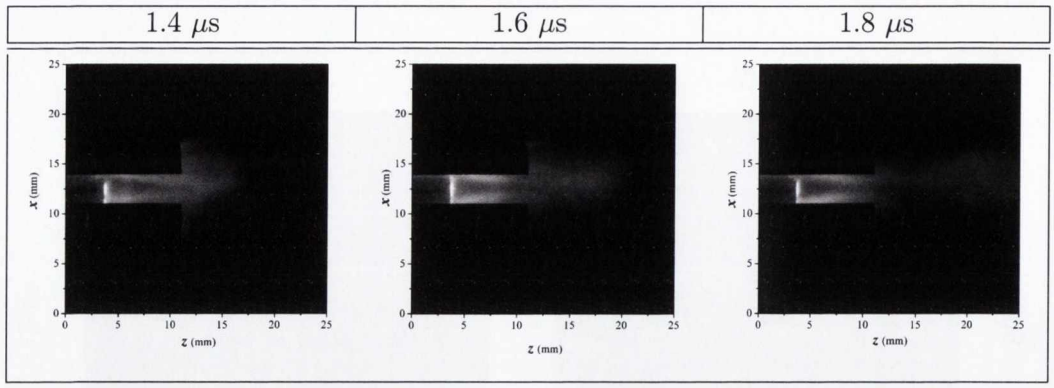

Figure 3.12: ICCD image sequence at later times; $\tau = 50$ ns.

In Fig. 3.2 it was shown that the discharge current begins to flow at 200 ns. Particular features in the discharge begin to arise at around 400 ns after the laser pulse, where an arc is seen to extend from the cathode to the collar, out to ~2 mm. This arc is then seen to decouple from the cathode surface in the shape of a wave, and propagate towards the end of the gun. Emission begins to appear at the end of the gun around 1 μs followed by the ejection of a slug of plasma at 1.6 μs (Fig. 3.12). This slug propagates at a velocity $v = 2 \times 10^6$ cm s^{-1}, which corroborates the distribution seen in Fig. 3.8.

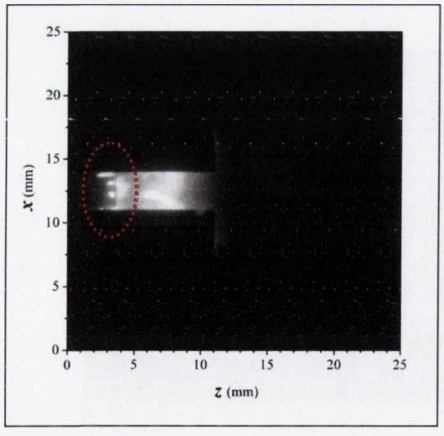

Figure 3.13: Arc spots on cathode; -800 V; $\Delta t = 600$ ns.

Plasma emission was observed up to 3 or 4 μs (depending on the voltage and current), corresponding to the duration of the current signal. Arc spots forming on the cathode surface were also observed intermittently throughout the discharge. Both on the top and sides of the electrode, these spots were especially notable at times corresponding to a high rate of current rise, which according to the literature, appear spontaneously with current rates-of-change of $dI/dt > 10^8$ A s^{-1} [37].

At -800 V arc spots were observed to appear at delays of 600 ns and 2.2 μs, corresponding to the rates $dI/dt = 6 \times 10^9$ A s^{-1}

and 2.3×10^9 A s^{-1}. These are precisely the times of current outflow [from the central electrode to the outer collar (see Fig. 3.13)]. Recall that under moderate current rates, spots form and dissolve as discharging ensues, often moving radially away from the center of the electrode due to retrograde motion (see section 1.3). However, when current rise rates exceed 10^9 A $s^{-1}$the original spot(s) formed by the laser plasma and initial current flow cannot sustain the required current density. The rate of formation of contiguous new spots cannot keep up with the demand of current outflow and new spots will form randomly at the surface [37]. Further evidence of the radial movement of arc spots on the cathode surface can be seen in a series of microscope images shown in Fig. 3.14. These were taken at a 50× magnification following 4000 shots/discharges.

Images show an increasing surface area of molten material around the ablation spot, which at 600 ns has exceeded the image area and covered the entire surface. Figure 3.14(d) shows a 500×magnification of the molten cathode surface at 600 V. Also noteworthy at 600 V (Fig. 3.14(c)) is the appearance of radial streaks as well as concentric patterns on the cathode surface. This might suggest retrograde motion taking place, with spots moving outwards as the discharge current increases.

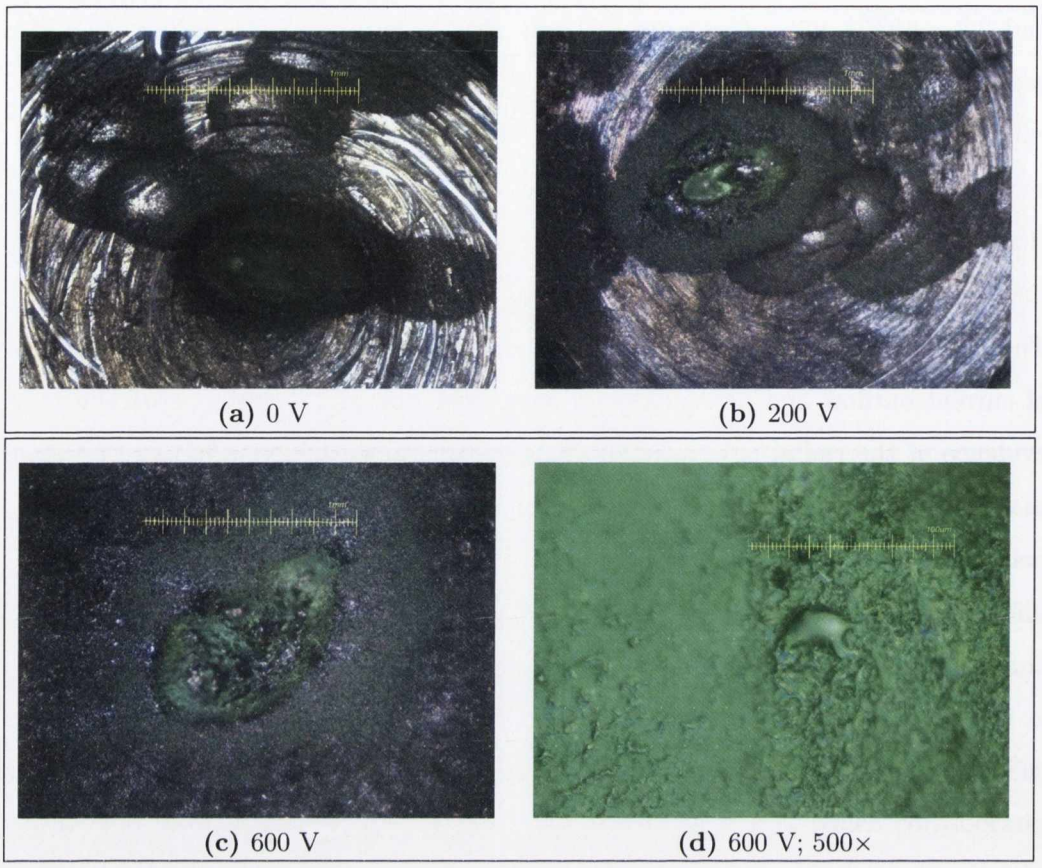

(a) 0 V **(b)** 200 V

(c) 600 V **(d)** 600 V; 500×

Figure 3.14: Microscope images of Al cathode for varying discharge voltages; 4000 shots.

3.4 Spectroscopy

Spectroscopic data was taken using a second ICCD camera coupled to a 1/4 meter Czerny-Turner spectrometer. Spatially-resolved spectral lines were captured simultaneously with the imaging ICCD. The output was analysed both as a spectral image, as well as spatially resolved spectra in order to study the behaviour of the various spectral lines as a function of time and discharge voltage. Images captured simultaneously with those shown in section 3.3 for 0 and -400 volts are shown in Figs. 3.16 and 3.17.

Within the first tens of nanoseconds from the arrival of the laser pulse ($\Delta t = 0$), a bright continuum in the spectrum is observed at the target surface. This is due to photon emission via Bremsstrahlung during the collisional phase of the plume expansion[1]. As time elapses, this continuum gives way to Stark-broadened spectral lines which evolve into the lines observed onwards of $\Delta t = 200$ ns. The magnified images in figure 3.15(a-b) show the appearance of this continuum at time zero and the lines beginning to form and expand upwards (y-axis).

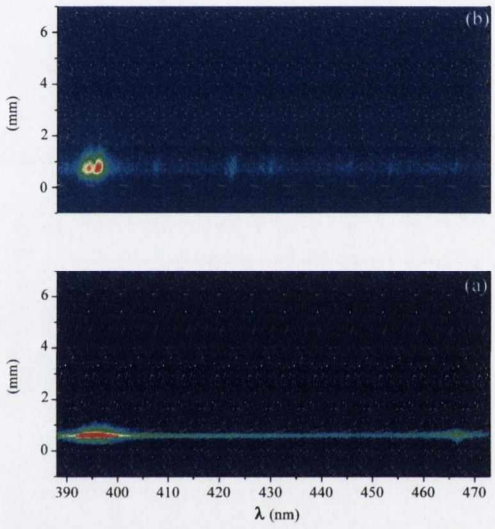

Figure 3.15: Continuum emission showing the strongly broadened Al I spectral line doublet (394/396 nm) (a) and line formation after 100 ns (b).

The wavelength of the most intense lines observed is shown in Fig. 3.18, which include neutral aluminium (Al I) as well as ions of Al II and III.

When no discharge is present, lines corresponding to neutral and singly-ionised

[1]This is actually a disputed point, since it has not been fully established if the continuum is due to severe Stark-broadening or free-free processes [63].

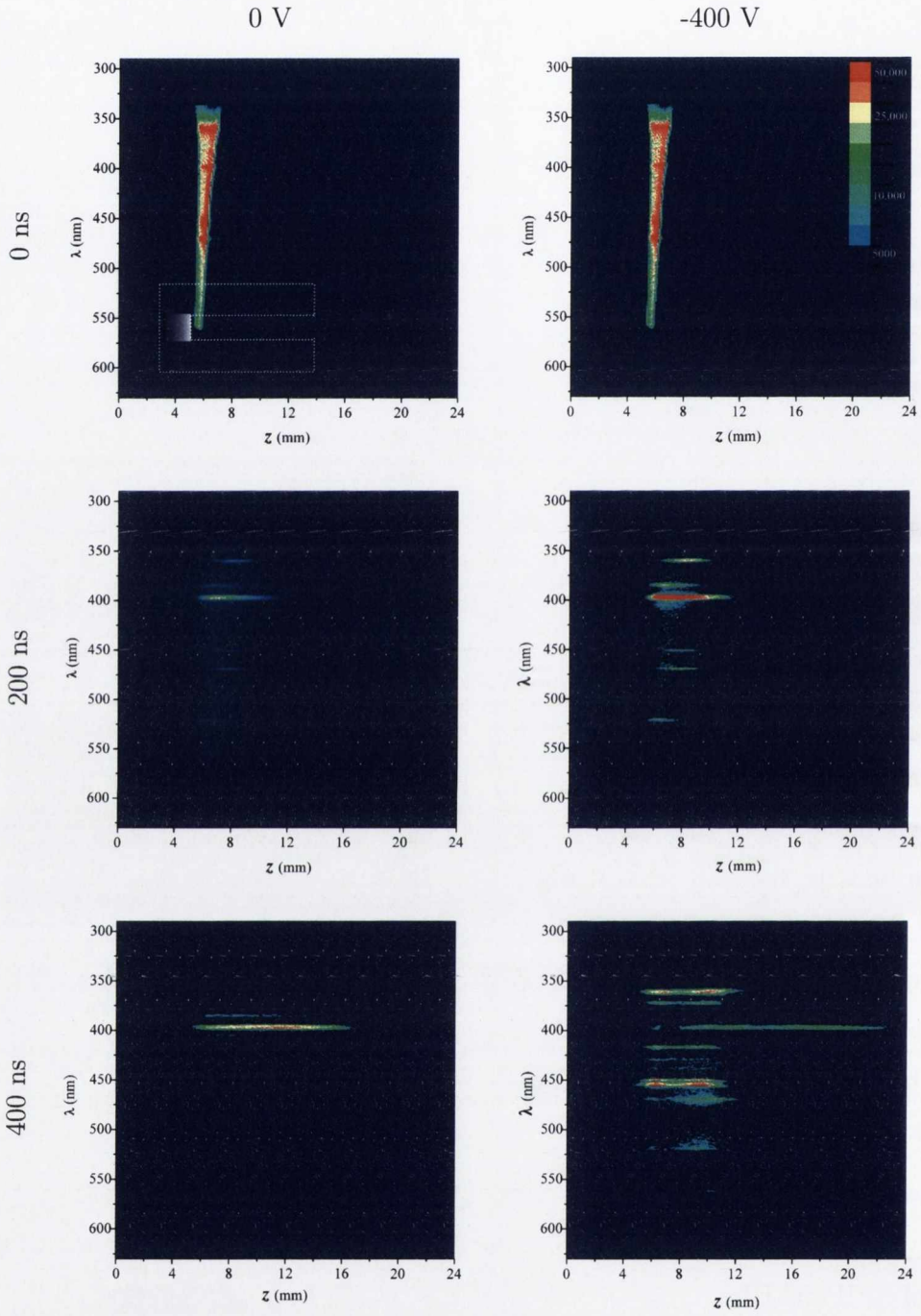

Figure 3.16: Time-resolved spectral image sequence comparing 0 and -400 V discharge. Top image shows collar position. Constant gain. Intensity scale is logarithmic.

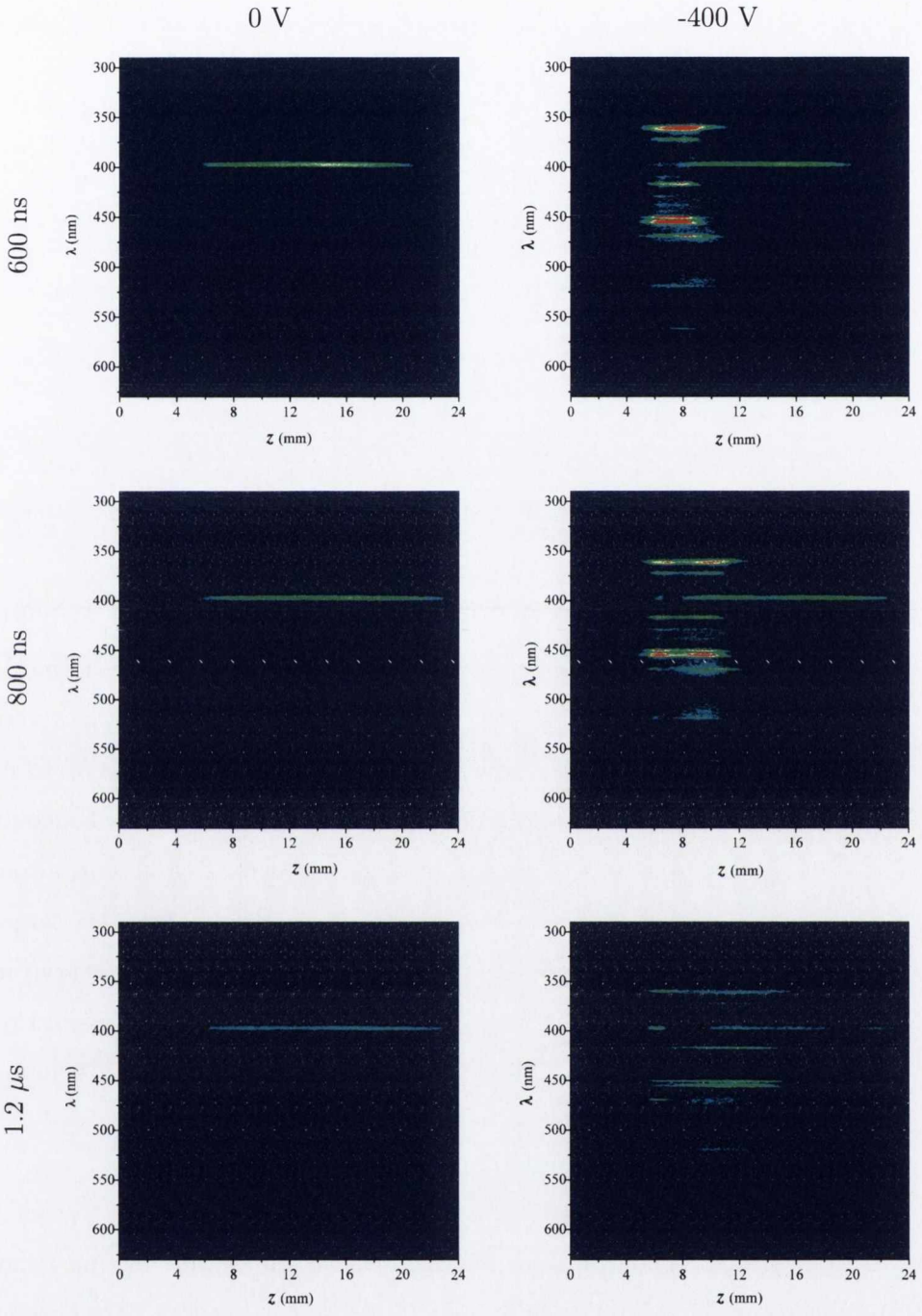

Figure 3.17: Time-resolved spectral image sequence comparing 0 and -400 V discharge potentials. Constant gain. Intensity scale is logarithmic.

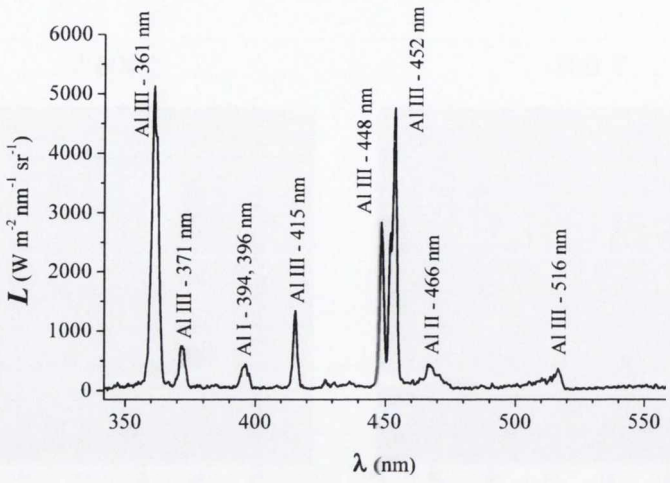

Figure 3.18: Spectral line identification; $V = -400$ V; $\Delta t = 800$ ns; $z = 1$ mm.

aluminium are observed, the most prominent being the neutral 394, 396 nm doublet. On the other hand, when the discharge is present, in addition to the Al I and Al II ions, intense lines of Al III are observed. Although higher ionisation stages were recorded with ion energy spectrum analysis (Section 3.5), only transitions up to Al III were observed in optical spectroscopy. As mentioned previously, so-called lineouts were taken from the image data to study the spectrum at increasing distances from the target. Therefore, lineouts were chosen for 1, 3, 6, 9 and 12 mm from the target (note the outer edge of the collar is ~10 mm). An example of these is shown in Figs. 3.19 and 3.20, where the lineout sequences are taken from the images in Fig. 3.17 at 800 ns, for both 0 and -400 V discharge. The spectra have been absolutely calibrated following the procedure in section 2.5.

Looking at zero volts, the line irradiance increases with distance (at this time delay most of the plasma has already exited the gun). Conversely, with -400 V the current is just starting to rise at this time and the series of Al III lines are beginning to appear close to the cathode. Note that the main Al I line seen in Fig. 3.19 (a) is also present at -400 V, having an irradiance of the same order in both cases.

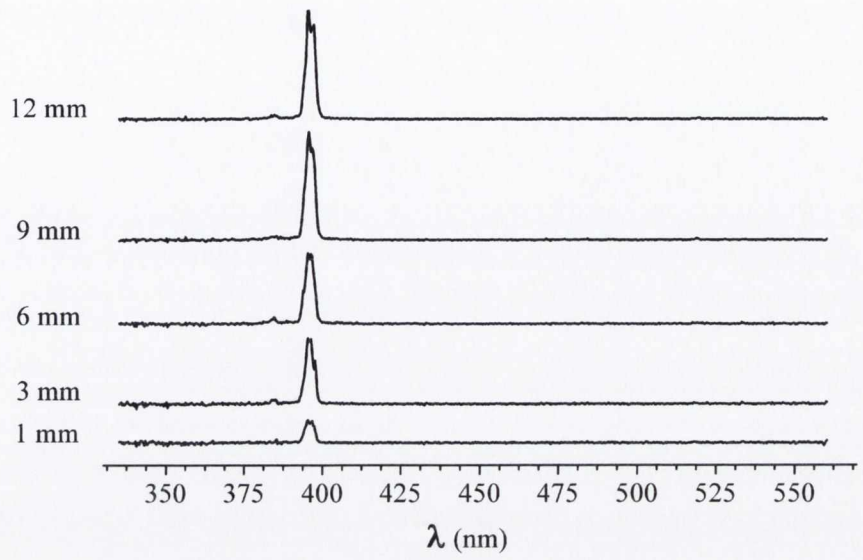

Figure 3.19: Lineouts at varying distance from the cathode at 0 V discharge and time delay $\Delta t = 800\ ns$.

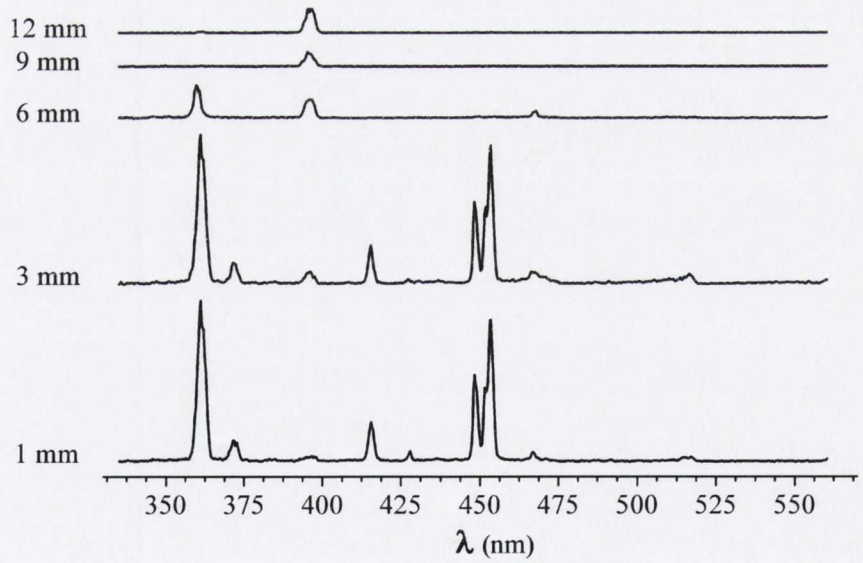

Figure 3.20: Lineouts at varying distance from the cathode at -400 V discharge and time delay $\Delta t = 800\ ns$.

Figures 3.21, 3.22 and 3.23 show the main transitions for neutral, singly- and doubly-ionised aluminium respectively. The transitions observed experimentally are shown in Table 3.1.

Note that the use of Boltzmann statistics throughout this spectroscopic analysis requires the condition for LTE to be met. Recall the McWhirter criterion from Section 1.2.2: $n_e \geq 1.6 \times 10^{12} T_e^{1/2} (\Delta E)^3$. Figure 3.24 shows a self-similar transform applied to the plot shown in Fig. 3.6 at 0 V. This signal represents the plasma density profile at 3 mm from the ablated target, distance at which current is seen to begin flowing, and shows a maximum density of 2×10^{16} cm^{-3}. Assuming a plasma temperature of $\sim$1 eV and a transition energy of 3 eV implies: $n_e \geq 5 \times 10^{15}$, therefore satisfying McWhirter's criterion.

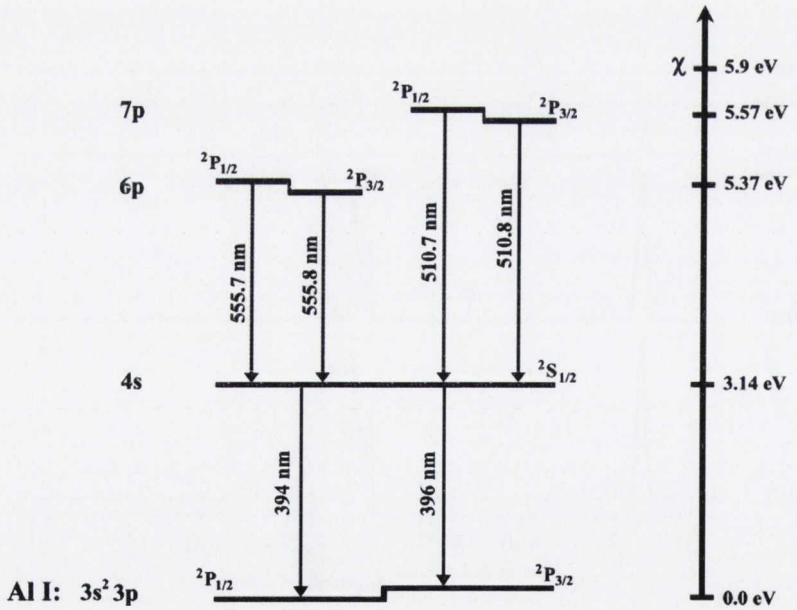

Figure 3.21: Energy level diagram of Al I. χ- Ionization potential.

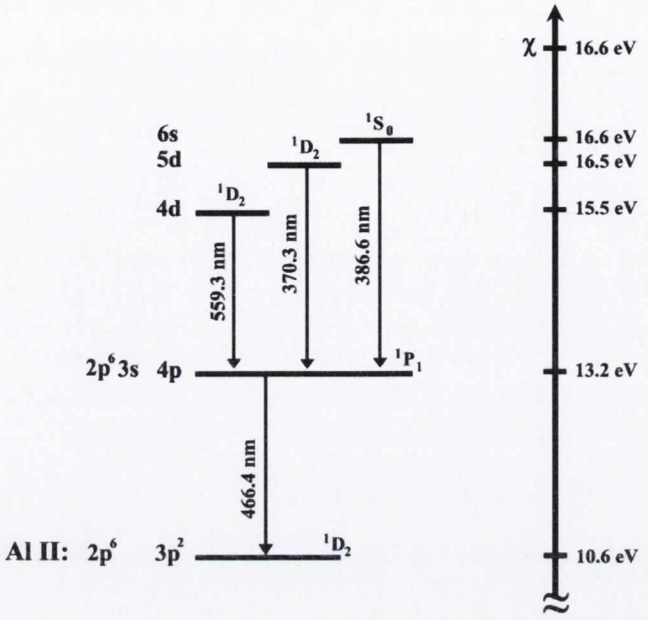

Figure 3.22: Energy level diagram of Al II. χ- Ionization potential.

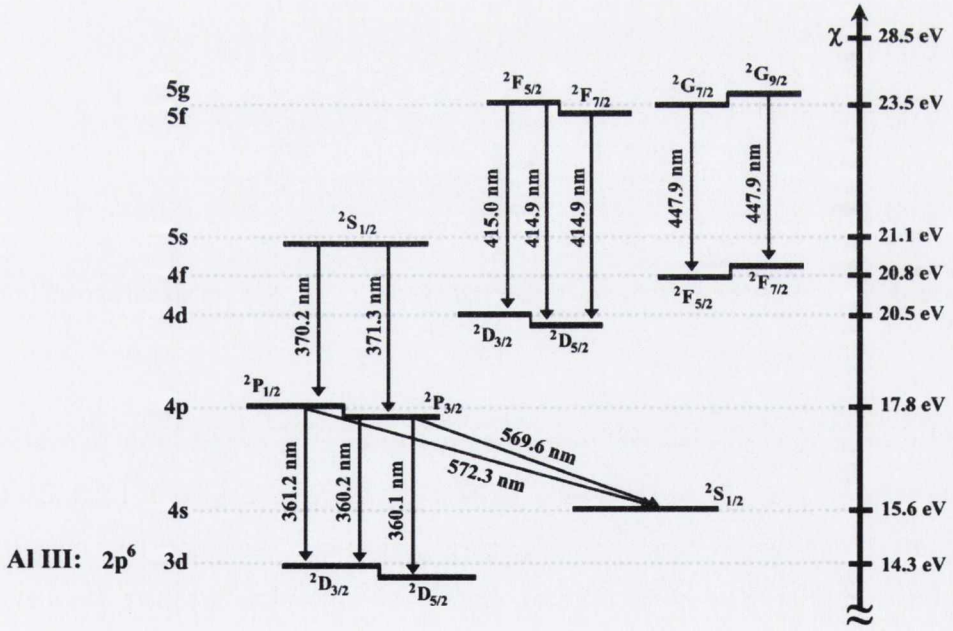

Figure 3.23: Energy level diagram of Al III. χ- Ionization potential.

Table 3.1: Aluminium transitions observed in laser and discharge plasma spectra.

Ion (Al)	λ (nm)	Transition
I	394	$3s^2 3p(^2P_{1/2}) \rightarrow 3s^2 4s(^2S_{1/2})$
I	396	$3s^2 3p(^2P_{3/2}) \rightarrow 3s^2 4s(^2S_{1/2})$
II	466	$3p^2(^1D_2) \rightarrow 3s\,4p(^1P_1)$
II	559	$3s\,4p(^1P_1) \rightarrow 3s\,4d(^1D_2)$
III	361	$2p^6 3d(^2D_{3/2}) \rightarrow 2p^6 4p(^2P_{1/2})$
III	371	$2p^6 5s(^2P_{3/2}) \rightarrow 2p^6 4p(^2S_{1/2})$
III	415	$2p^6 4d(^2D_{5/2}) \rightarrow 2p^6 5f\,(^2F_{7/2})$
III	448	$2p^6 4f\,(^2F_{5/2}) \rightarrow 2p^6 5g(^2G_{7/2})$
III	452	$2p^6 4p(^2P_{3/2}) \rightarrow 2p^6 4d(^2D_{5/2})$
III	516	$2p^6 5g(^2G) \rightarrow 2p^6 7h(^2H)$

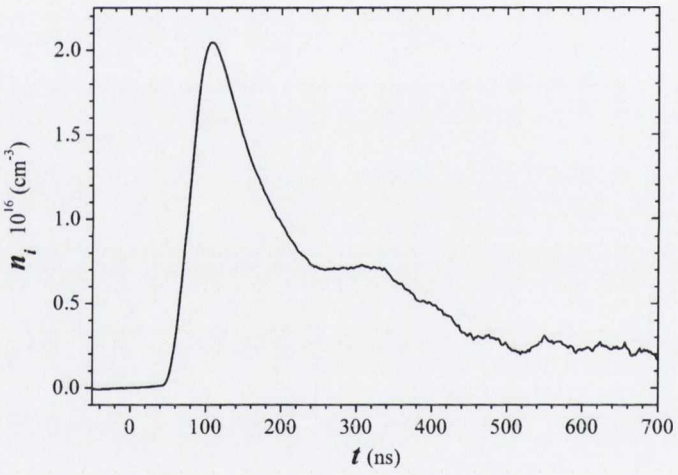

Figure 3.24: Probe signal at 3 mm using a self-similar estimate from signal shown in Fig. 3.6; 0 V.

Based on the cited transitions, a temperature can be extracted from the ratio of line intensities based on the Boltzmann statistics reviewed in Section 1.2.3. To this effect, in order to get a good spread when fitting the data, line transitions must have upper energy levels that are wide apart. Indeed, by taking the 361, 370, 415 and 452 nm lines, Boltzmann plots were analysed for varying time delays and distances from the target to map out the temperature. An example of this is shown in Fig. 3.25,

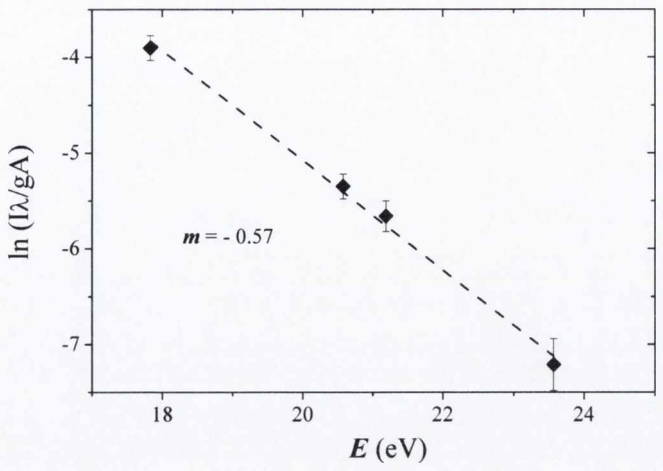

Figure 3.25: Boltzmann plot; $d = 1$ mm; $\Delta t = 800$ ns; 400 V.

based on the lineout at 1 mm shown in Fig. 3.19(b). The area under the lines was calculated in order to determine I, whilst the values of E_2, g and A (the upper-level energy, state degeneracy and transition probability) were taken from the National Institute of Standards and Technology (NIST) tables.

The Boltzmann plot thus shows the plasma electron temperature as the negative inverse of the slope for a given distance and time delay. Which in Fig. 3.25 is: $T_e = 1.7$ eV. This result is consistent with values reported in the literature, where typical LPP electron temperatures under similar conditions are in the range of 1-2 eV [64, 65].

The electron temperature can therefore be calculated for the distances and time delays of the experiment. A comparison of these for -400 and -800 V discharge voltages is shown in Figs. 3.26 and 3.27 respectively. Profiles were calculated from 1 to 12 mm from the cathode, where it should be noted that the edge of the collar is found at ~10 mm.

As will be discussed below, the electron temperature of the LPP at 3 mm after 200 ns is ~1 eV. As time evolves, the temperature at this distance will have dropped to 0.6 - 0.8 eV. However, as the discharge ensues, around Δt =600 ns, the electron temperature is seen to rise to 2.2 and 2.8 eV for the -400 and -800 V discharges

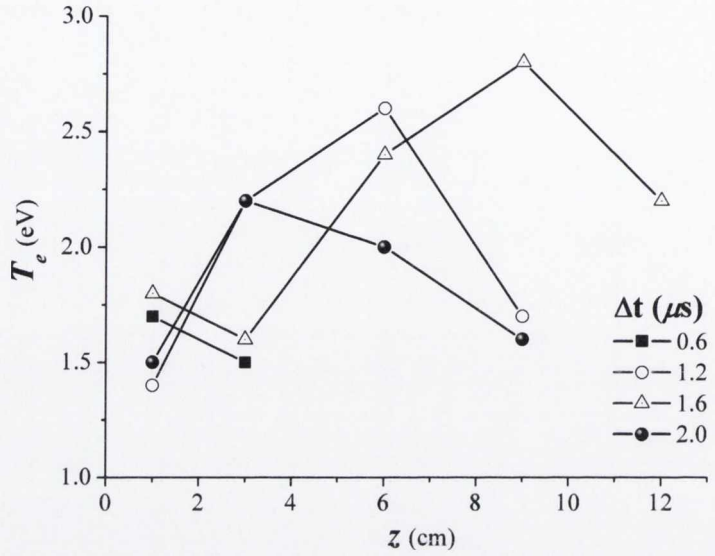

Figure 3.26: Electron temperature profiles as a function of distance for varying time delay; -400 V discharge.

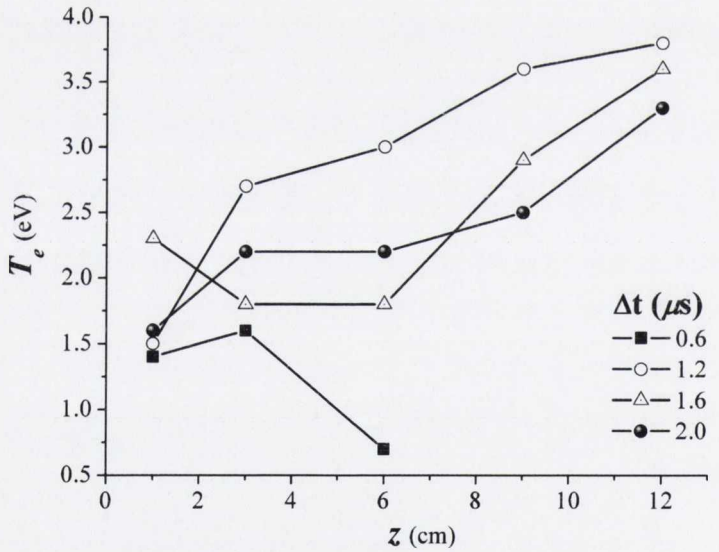

Figure 3.27: Electron temperature profiles as a function of distance for varying time delay; -800 V discharge.

respectively. The electron temperature appears to increase with distance as well, reaching its maximum close to the edge of the collar in the -400 V case. For -800 V, however, the maximum seems to extend outside the collar edge, and the maximum recorded temperature is almost 4 eV at 12 mm (outside the collar), at a time delay of 1.2 μs.

As shown in Fig. 3.19, the emission spectrum of the LPP without a discharge only shows one spectral line, which pertains to the 394/396 doublet. Because this is the only line present, the electron temperature could not be calculated from Boltzmann statistics, and the spectroscopy software package *PrismSPECT* presented in Section 2.6 was used instead. The main quantities needed to compute the the spectral lines are the electron temperature, ion density (n_i) and plasma thickness (t_P). The latter term being related to the number of emitting atoms in the line of sight. Care must be taken when choosing these parameters, since there are multiple combinations of these that can give a similar spectrum.

In order to get a good approximation for T_e, the thickness was taken to be $t_P = 1$ cm, since one can assume the plasma is mostly constrained by the collar, which measures 1 cm in diameter. On the other hand, to get an approximation of the density to be used in the program, the self-similar probe theory was applied (Section 2.3.3).

Taking the probe signal shown in Fig. 3.6 for zero voltage, the density profile at 3 mm was estimated using self-similar theory (Fig. 3.28). This plot gives a density profile as a function of time, which was used to approximate the density values in the simulation for different time delays. Indeed, at a constant distance of 3 mm, lineouts are compared to simulations in Fig. 3.29.

The values of T_e and n_i used to fit the spectra are shown in Table 3.2, comparing them to those taken from the ion probe signal at 3 mm.

The density values from the probe and those used for the spectroscopy simulations are in good agreement, which adds confidence to the temperature estimate.

It can therefore be concluded that at 3 mm (approximately where the discharge makes initial contact with the collar), the laser produced plasma has a temperature

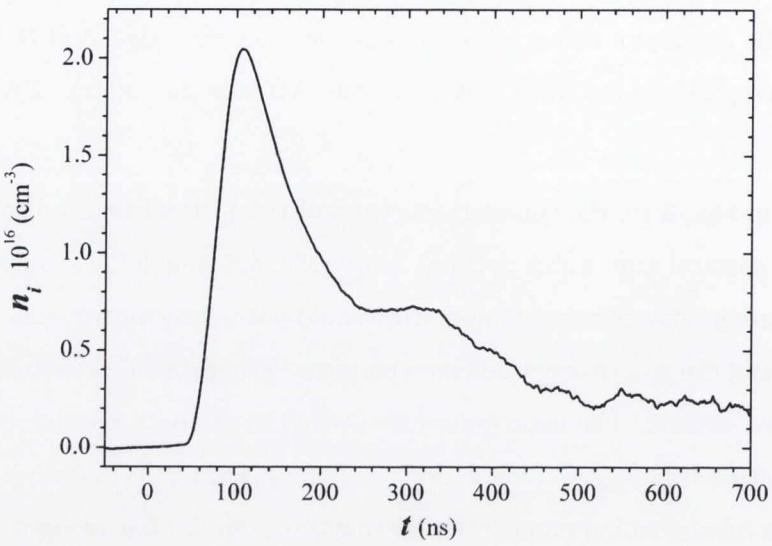

Figure 3.28: Ion density profile at 3 mm from target.

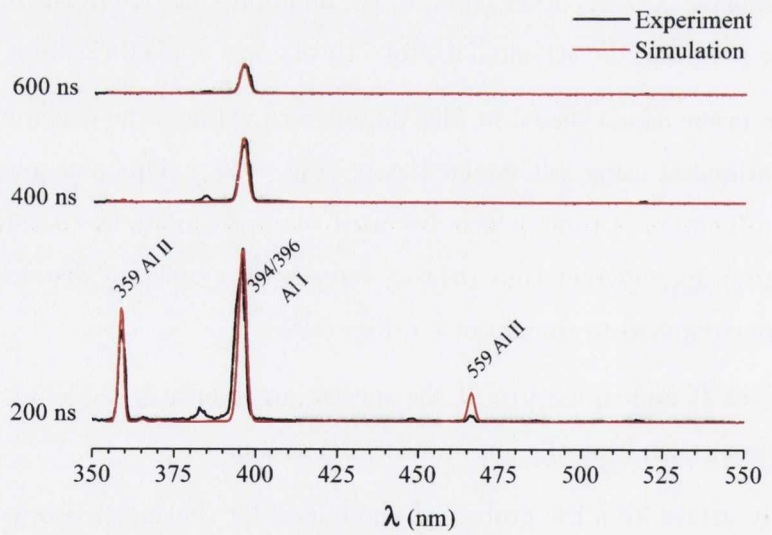

Figure 3.29: PrismSPECT fits at 3 mm for different time delays.

Table 3.2: Electron temperature and ion density at 3mm used for PrismSPECT simulations. Mean ionisation ($\bar{Z}$) and electron density are calculations done by the software.

Δt (ns)	T_e (eV)	n_i (Probe)	n_i (PSpect)	n_e (PSpect)	$\bar{Z}$
			($\times 10^{15}$ cm^{-3})		
200	1.1	9.6	8.3	8.9	1.1
400	0.90	4.9	3.0	3.0	1.0
600	0.80	2.2	1.3	1.3	1.0

of ~1 eV. At this same position, the temperature will begin to rise as the discharge ensues, reaching values of 2.5 eV (V = -800 volts). As time progresses, the high-temperature area moves out towards the end of the barrel and temperature continues to rise, showing maximum values at the outer edge of the collar. Looking at the profiles, the plasma may actually be hotter outside the collar.

3.5 Time-of-Flight Mass Spectroscopy

Analysis was performed for aluminium cathode targets ablated using an Nd:YAG laser emitting at 1064 nm, with a fluence of 1 J cm^2. In this experiment, distances were overall larger than in the previous studies, given the chamber size. The probe distance was 40 cm, while the ESA detector (microchannel plate) was 1.4 m away from the gun. Ion and electron signals were taken for the full range of discharge voltages (0-1 kV), and are shown in Figs. 3.30 and 3.31. A feature to note in the signals is the seemingly sharp decrease in ion flux at the maximum discharge voltage (1 kV). This was due, in part, to the high variability in signal strength registered at the probe. In other words, shot-to-shot probe signals varied widely in peak voltage, as well as temporally. Notwithstanding, the fact that each ESA signal was recorded simultaneously with the ion/electron signals in question, made a correlation between these possible.

For the range of discharge voltages studied, electron signals are in good agreement with their ion counterparts. Electric potential across the curved electrostatic plates of the energy spectrum analyser (ESA) was scanned starting at ΔV= 20 V. The

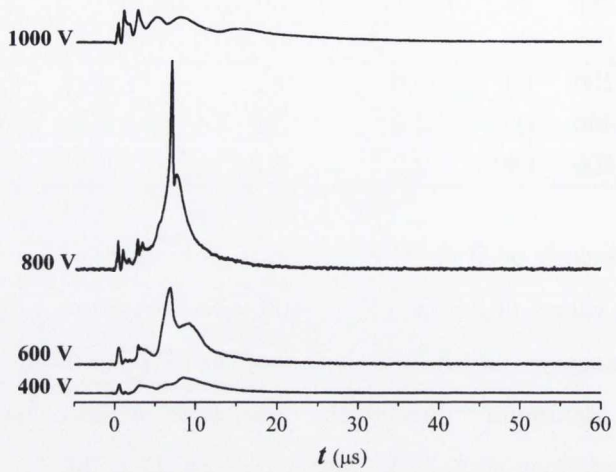

Figure 3.30: Ion signals taken simultaneously with the energy spectrum analyser data for changing discharge voltage.

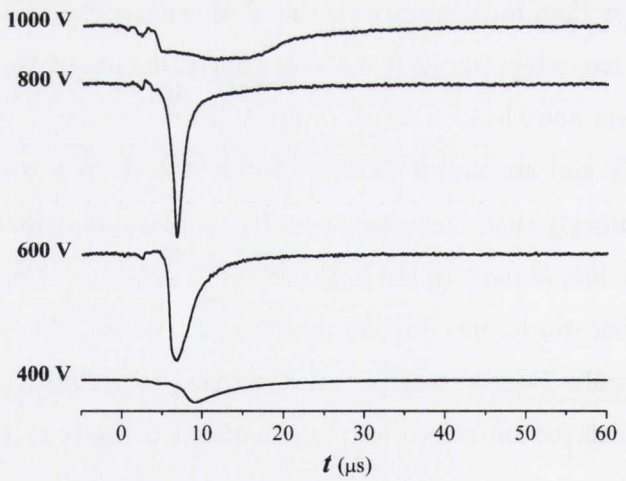

Figure 3.31: Electron signals taken simultaneously with the energy spectrum analyser data for changing discharge voltage.

range of plate potentials was increased up to $\Delta V =$ 1000 V as the discharge voltage went from 0 to 1 kV in order to detect the more highly charged species in the plasma.

Figure 3.32 shows the time of flight (t_f) signals obtained from the ESA of the pure ablation plume (no discharge). Note that except for $\Delta V =$ 40 V, where a second peak observed at 30 μs, only one peak is observed per voltage setting, implying that there is a single ionic species in the plasma (Al II). The second peak observed at 40 V corresponds to a small number of Al III ions. Recalling the mass spectrometer and time of flight equations from Section 3.5, where $\frac{E}{q} = \frac{\Delta V}{R}$ and $t_f = x\sqrt{\frac{m}{2E}}$, the ionic species in the plasma can be determined by matching the peaks to the expected times-of flight. Table 3.3 shows the time of flight and associated energies expected for Al II, which agree with the spectrum in Fig. 3.32.

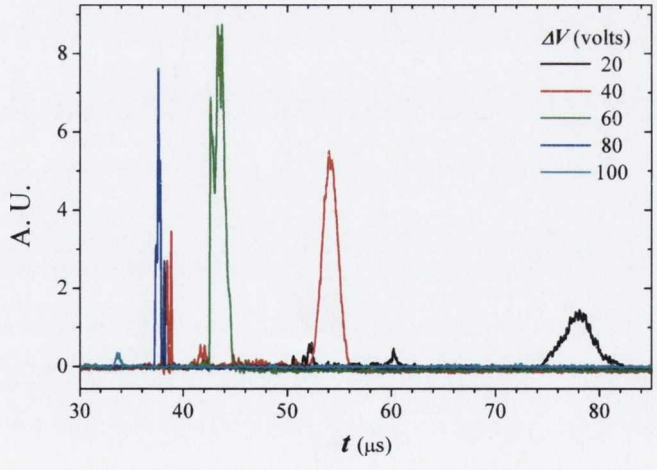

Figure 3.32: Time of flight Al II peaks from plasma plume; no discharge.

Table 3.3: Comparison of experimental and calculated times of flight and ion kinetic energies for peaks in fig. 3.32. Experimental errors are taken from the FWHM; calculated errors (Δt_f and ΔE) are discussed in section 2.7.

ΔV (volts)	E (eV) (±5 %)	t_f (μs) *(calculated)*	t_f (μs) *(measured)*
20	46 (±2)	76 (±4)	78 (±4)
40	91 (±5)	54 (±2)	54 (±2)
60	136 (±7)	44 (±1)	43 (±2)
80	182 (±9)	38 (±1)	38 (±1)
100	227 (±11)	34 (±1)	34 (±1)

As the table shows, the time of flight values are in good agreement with the peaks in the spectrum, especially for the higher energy (lower t_f) ions. It can be noted that the width of the peak changes with t_f, becoming increasingly narrow at earlier times. This can be explained via the error associated with the power supplies, as well as the bandpass of the analyser (cf. Section 3.5).

As the discharge potential is increased, the number of peaks per ESA potential (ΔV) also increases, each corresponding to a different ionic species in the plasma. For instance, Figs. 3.33 and 3.34 show the time of flight spectra of a -800 V discharge at two ESA potentials: 120 V and 320 V. Note that there are extra peaks appearing other than aluminium which were found to correspond to hydrogen, carbon and oxygen; contaminants likely pertaining to impurities on the electrode surfaces or a the Teflon insulation at the base of the discharge cell.

By noting that the area under the curve of each peak is proportional to the number of ions impinging on the detector (MCP), it is possible to infer an ion time of flight distribution for each species in the plasma, i.e., the amount of ions arriving at the detector at a given time. This information can then be correlated with the ion probe signal in order to identify the time of arrival of the various ions to the probe; albeit having the probe at a considerably shorter distance than the ESA. Each point in Fig. 3.35 represents the integrated signal of an Al II peak in Fig. 3.32. This plot also shows the Al III peak (marked as a star), which observed in Fig. 3.32 as well; this peak is seen at $\Delta V = 40$ and has a time of flight $t_f \approx 38$ μs. Under the

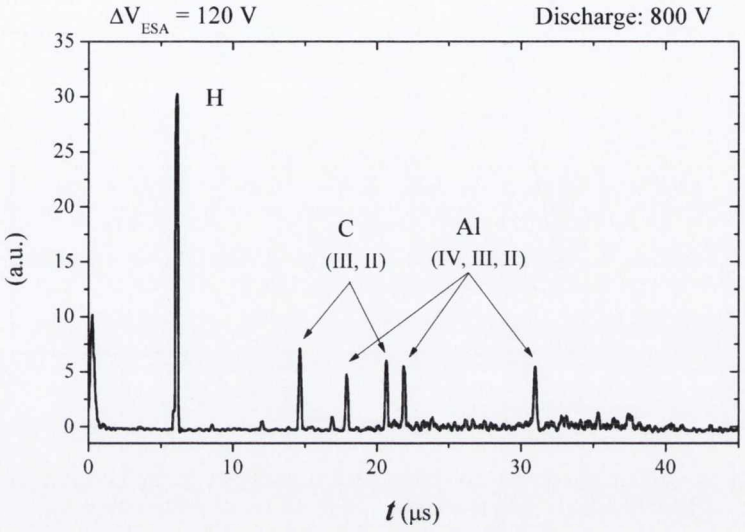

Figure 3.33: ESA t_f peaks for $\Delta V = 120$ V plate potential during -800 V discharge.

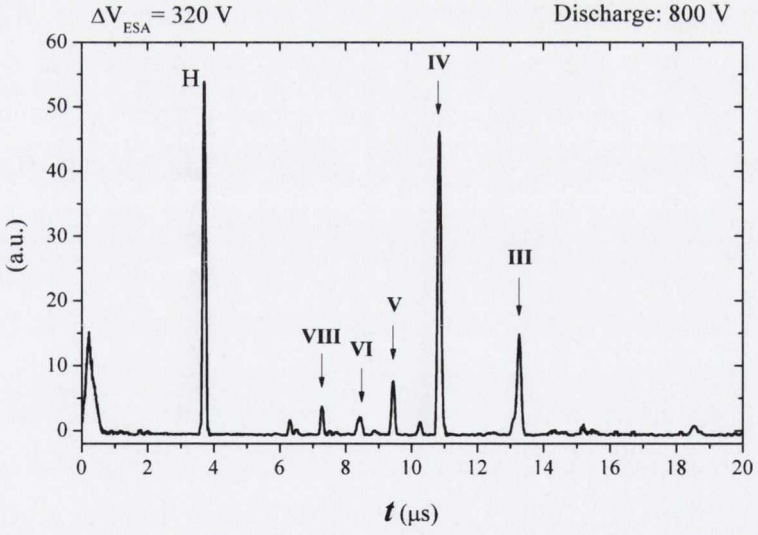

Figure 3.34: t_f peaks for $\Delta V = 320$ V plate potential during -800 V discharge.

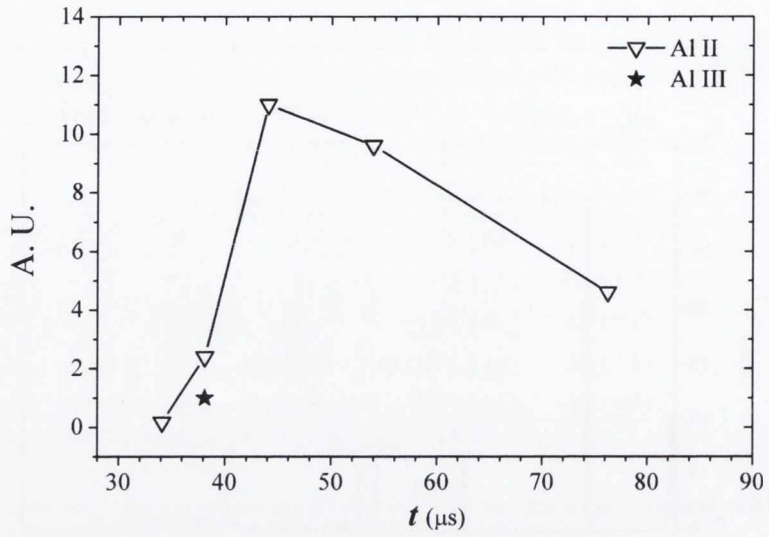

Figure 3.35: Time of flight distribution at MCP detector.

assumption of inertial plume expansion, the time of flight can be scaled down from the original distance of the ESA (140 cm) to the distance of the probe (45 cm) by simply scaling the time as (45/140). A superposition of the time-scaled plot and the ion signal is shown in Fig. 3.36, where it can be seen that both signals are in close agreement. Note that in order to match the contribution of ions from the ESA peak to that of the probe, one must consider the amount of charge deposited by each ion species. In other words, singly-ionised species deposit one unit of charge, doubly-ionised species deposit two units, etc. Therefore, in this case, the integrated ESA peak corresponding to Al III should be multiplied $\times 2$. Furthermore, multiply-charged ions having the same time of flight will have an additive contribution; for instance, both the Al II and Al III points occurring at t_f =38 μs must be added, as shown with the filled triangle in Fig. 3.36.

In addition to the time of flight, an energy spectrum can also be plotted based on the ion energies, as shown in Table 3.3. By once again integrating the Al II ion peaks, which are proportional to the ion number N, a plot of dN/dE vs. E for each peak in the spectrum can be obtained; these are plotted in Fig. 3.37. Note that 'dN/dE' is only a proportional term, since the exact value of density is not known. By the same

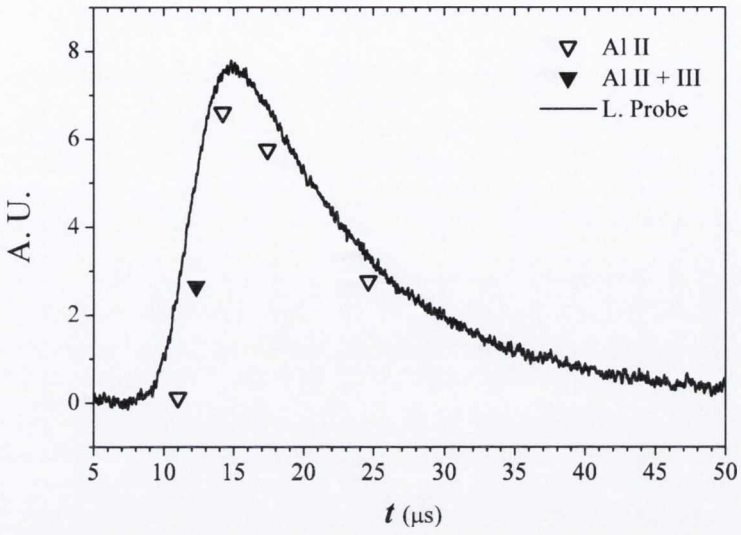

Figure 3.36: Superposition of Langmuir probe signal and ESA time of flight spectrum at 45 cm from plasma gun. The Al II and Al III points have been added to represent the charge contribution to the probe.

token, this spectrum can be compared to the energy distribution obtained from the ion probe. Figure 3.38 shows the superposition of ESA data with the ion energy distribution obtained from the probe signal (cf. Section 2.3.2).

Based on the technique described, it is therefore possible to infer the nature of more complex ion signals such as those observed with the discharge. Indeed, analysis of the plasma plume by comparing the ESA and Langmuir probe signals was done for a -600 V discharge. Figure 3.39 shows the probe signal along with a sample of the data from the ESA (Fig. 3.40), taken at $\Delta V = 320$. The probe signal is similar in character to those shown in previous sections, although the faster components between 1 and 4 μs appear more pronounced. The ESA signal shows lines corresponding to aluminium ions from Al II up to Al IX, along with contaminant ions: C III and O III.

By applying the technique described above, a plot of the time of flight distribution for each ion species (Al II-IV plus H) vs. the time of flight is shown figure 3.41. In order to infer the behaviour of the plasma at the probe position (45 cm), the ESA timescale was multiplied by the distance ratio (45/140). In addition to this, the signal counts of each ion species were multiplied by their respective charge state

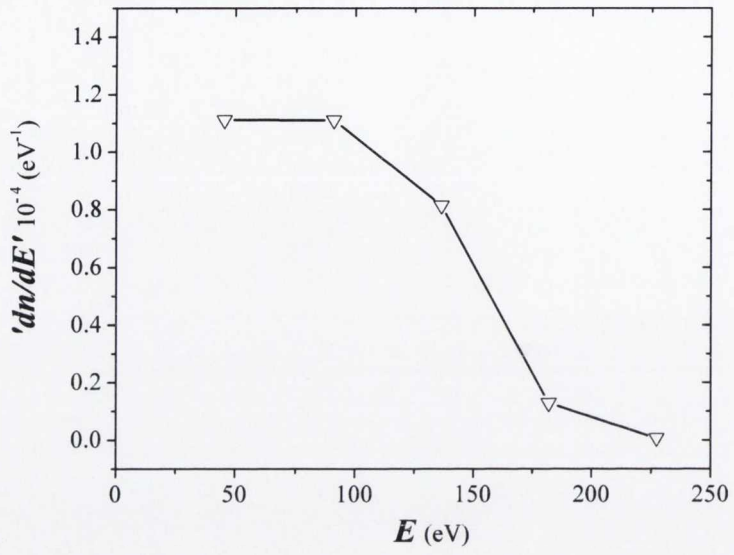

Figure 3.37: Energy spectrum of Al II ions in ablation plasma.

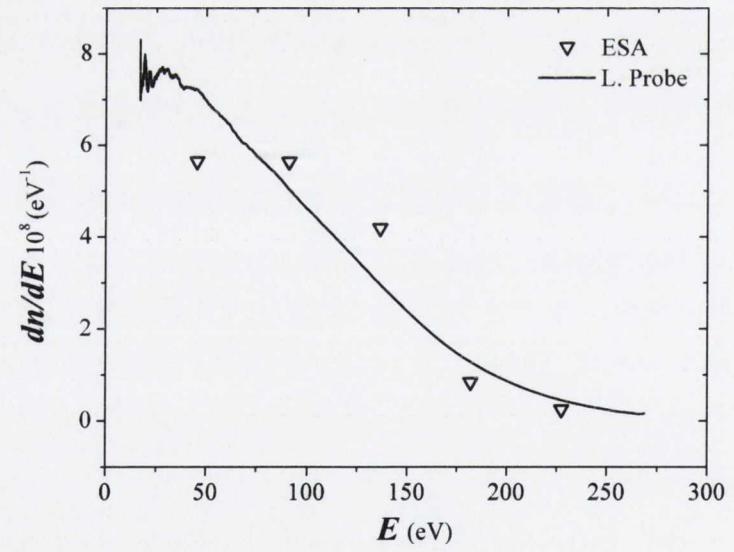

Figure 3.38: Energy spectrum comparing Langmuir probe and ESA data. Ordinate scale from probe data.

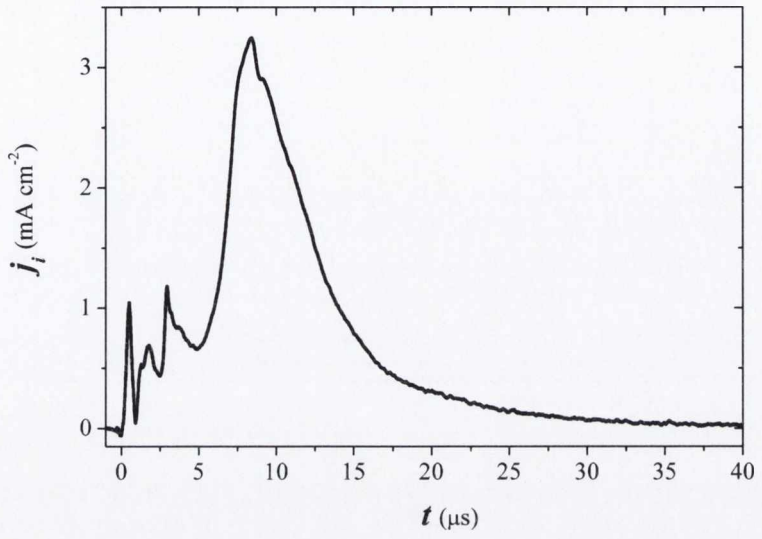

Figure 3.39: Ion probe signal at V = -600 volts discharge.

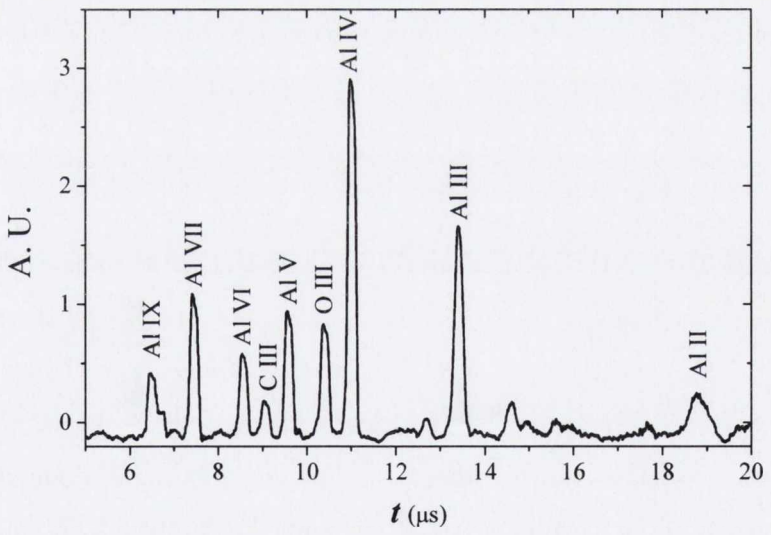

Figure 3.40: ESA time-of-flight peaks for at V = -600; ΔV = 320.

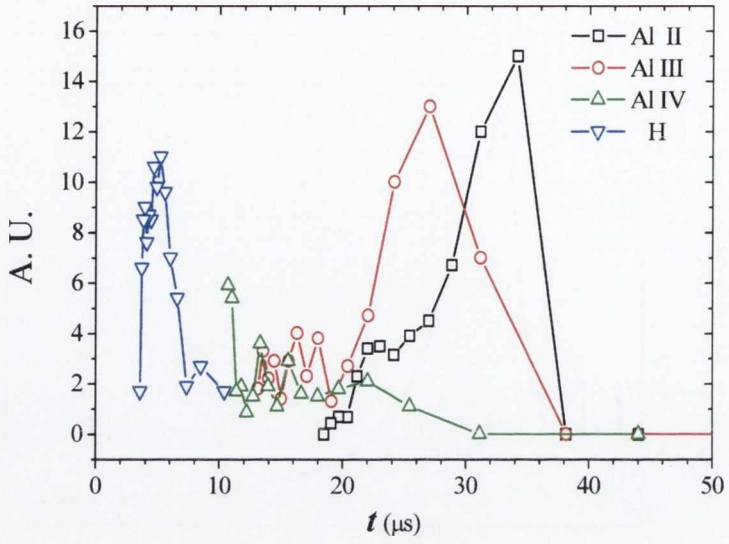

Figure 3.41: Time of flight distribution for H*, Al II, Al III and Al IV ions; -600 V discharge.

* Hydrogen points are multiplied by 0.10

in order to obtain a correlation with the ion probe signal; both signals are shown superimposed in Fig. 3.42. An exception to this operation was hydrogen, which had a disproportionately large signal, and was thus divided by 10 in both plots. The behaviour exhibited by the hydrogen ions is likely due to the MCP's sensitivity to ion mass and charge, which for this particular instrument is not fully characterised.

In spite of the lack of absolute calibration of the ESA, the relative ionic contributions to the ion probe can be inferred in general terms, where the greater part of the ion signal is dominated by Al III ions followed by Al II. This is the same result observed in spectroscopy, where the lines of highest irradiance during the discharge were indeed mostly from Al III transitions. The faster components in the ion signal are due to a combination of highly ionised aluminium as well as the O, C, N and H contaminants, the latter peaking at $\sim 2\mu$s. The lack of time of flight information at the tail end of the ion signal is due to the lower limit of the ESA voltage across the plates, where the lowest possible value was $\Delta V = 20$ V. A notable feature in the ion probe signal, which is not accounted for in the ESA distribution, is the fast peak observed at ~500 ns. This peak was observed on many occasions, not only

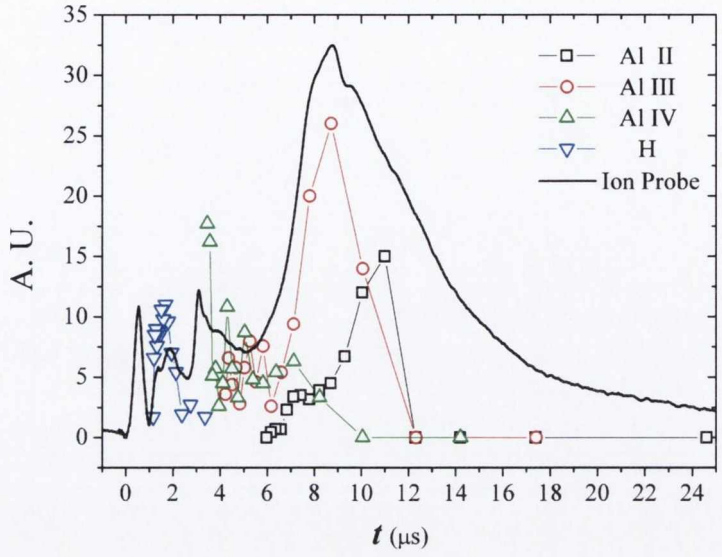

Figure 3.42: Superposition of ion probe signal and time of flight ion distributions at 45 cm; -600 V discharge.

* Hydrogen points are multiplied by 0.10

during these experiments at UCD, but also in the TCD lab. It is likely this peak is produced by EUV light generated during the discharge, especially given that the peak appears at the time the discharge current reaches its first maximum (Fig. 3.43). The mechanism behind this peak is similar to the so-called photopeak observed in probe signals during conventional laser ablation.

This peak occurs as the laser impinges on the target surface and the bright continuum due to Bremsstrahlung emission is produced. This emission includes photons with sufficient energy to remove electrons from the probe surface, whereby the removal of negative charge produces a positive current signal. Likewise, this emission of high energy photons is thought to occur via the additional heating of the plasma due to a current-induced magnetic pinch.

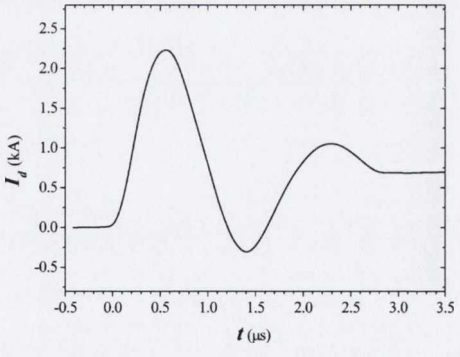

Figure 3.43: Discharge current; -600 V .

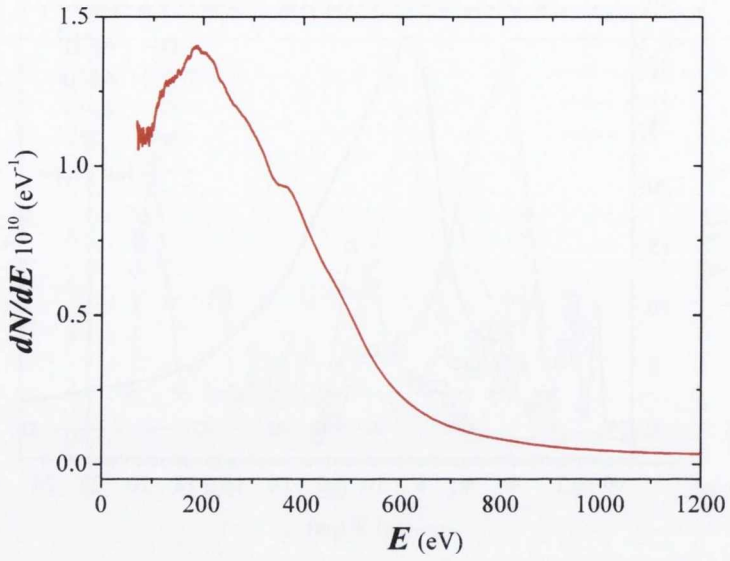

Figure 3.44: Ion energy distribution taken from Langmuir probe signal.

The energy spectrum obtained from the ESA data when analysing the -600 V discharge can also be compared to the ion energy distribution from the probe; similar to Fig. 3.38 for no discharge. Figure 3.44 shows the energy distribution dN/dE taken from the probe signal, whilst Fig. 3.45 shows a superposition of both the energy distribution and energy spectra taken from the analyser peaks of Al II, III and IV. Note that although the signals show good agreement in certain features, this comparison is only an approximation. Because the electrostatic probe is sensitive to charged states, the contribution of each ion species will affect the magnitude of the dN/dE signal, therefore, the curve shown in Fig. 3.44 is actually an over-estimate of the actual value, especially at higher energies.

3.6 Thin Film Depositions

Material distribution exiting the plasma gun at varying discharge voltages was analysed by placing a substrate directly in front of the gun. After a few thousand shots/discharges, a thin film will form on the substrate as the ejected material aggregates on the slide. Following these depositions, the total mass removed from

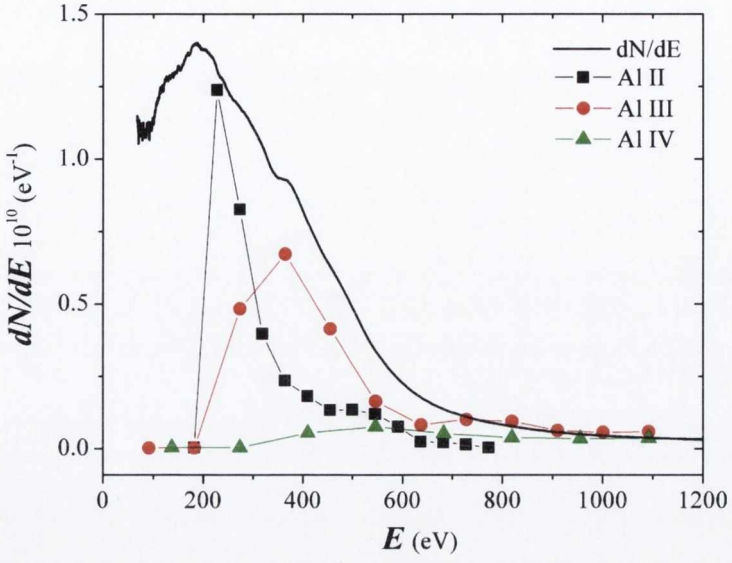

Figure 3.45: Superposition of ion energy distribution from Langmuir probe and energy spectra of Al II, III and IV.

the ablated target was measured using a precision balance. Depositions were done using copper targets on glass substrates placed 2.5 cm from the gun. The thickness of the deposited films following 1000 shots was determined using a transmission-mode scanner. The image from the scanned substrates was processed to determine a thickness profile across the film. The technique of going from a scanned image to a thickness profile relies on calibrating the scanner intensity output to get an equivalent transmission, a task carried out elsewhere using a set of neutral density filters [2]. Once the substrate is scanned, the image output is set to record a .TIFF image file. This type of file can be read using Matlab as an RGB file, i.e. a three-colour matrix with red, green and blue channels. The green channel (~515 nm) was found to have the most reliable output, and was therefore used to calculate film and substrate transmission. The final step in determining equivalent thickness from the transmission was done using the bulk absorption properties of copper (calculated using the optical properties software XOP) [63, 66]. Trials were taken for 0, ±400 and ±800 V discharges, i.e. depositions were done having the central electrode charged both

[2]Calibration done in University of Naples, Federico II.

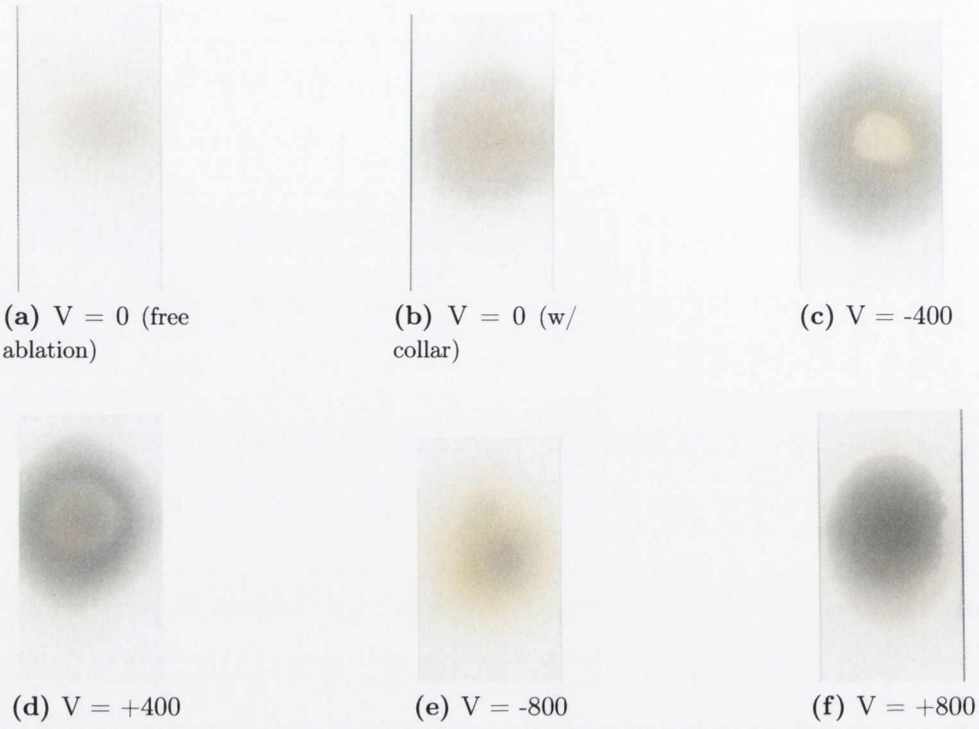

(a) V = 0 (free ablation)

(b) V = 0 (w/ collar)

(c) V = -400

(d) V = +400

(e) V = -800

(f) V = +800

Figure 3.46: Scanned film depositions; 1000 shots; Cu on glass.

positively and negatively, which allowed the current to flow inwards or outwards. The image sequence in Fig. 3.46 shows the scans taken for each deposition.

Thickness profiles across the centre of each thin film are shown in Fig. 3.47 for varying discharge conditions. From these plots it is evident that the collar has a collimating effect on the expanding plasma, even without a discharge. Once the discharge is applied, as in the 400V case, certain features emerge where the central part of the film appears thinner than the edges. Furthermore, the raised edges, which are the thickest part of the film, are actually of the same width as the collar (1 cm). It would seem that at this voltage, whether positive or negative, some mechanism is removing material from the center of the film and/or inhibiting growth. Another feature of interest is that when the central electrode is positively-charged the total material deposited is greater than in the negative case.

To explain the shallow centers on some of these films, attention is drawn to the ion energy distribution found in Fig. 3.8 (b). When no discharge is present, the laser

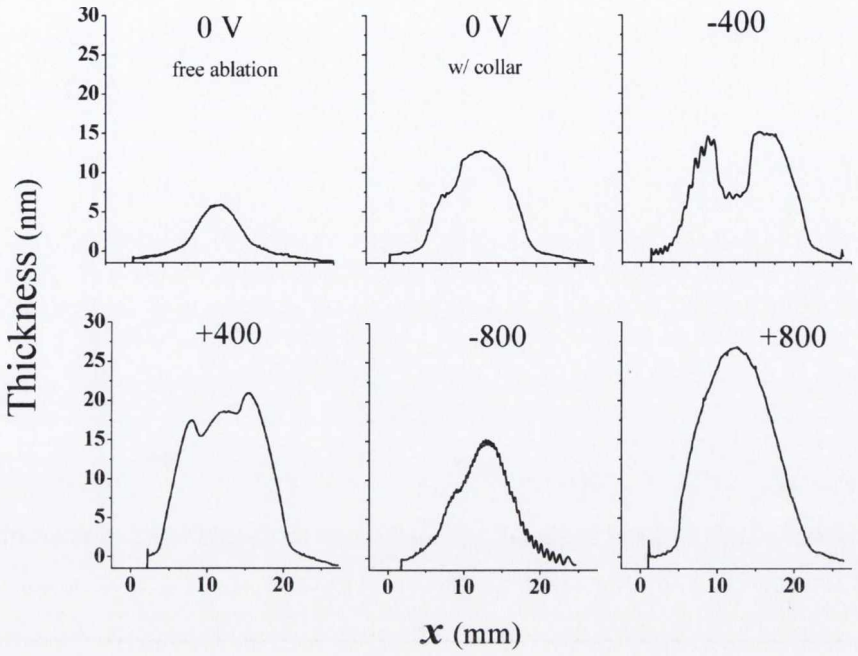

Figure 3.47: Film thickness profiles for Cu depositions on glass.

produced plasma ions have an energy distribution where the majority of ions are found between 1 eV and 20 eV, an energy regime where deposition is the predominant process when particles arrive at the substrate. However, at ion energies greater than 50 eV the effect of sputtering begins to play an important part in the removal of atoms from the film surface. As particle energy increases, so does the yield of sputtered ions, and depending on the projectile ion mass, the sputter yield reaches a maximum at ~100 eV [67, 68]. Looking at the ion energy distribution of the 600 V discharge in Fig. 3.44, it is evident ions are in the range 100-400 eV, which would easily produce sputtering of the film.

Table 3.4 shows the mass removal rate calculated following each deposition. As mentioned, this was calculated by weighing the targets before and after the experiment. In this same table are estimates of the mass deposited on the substrates shown in Fig. 3.46 and the ratio of mass deposited to mass removed.

Table 3.4: Mass removal rate following depositions; m_r mass removed from target; m_d mass deposited on films.

V (volts)	$Rate$ (ng/shot)	m_r (μg) [$\pm$0.5]	m_d (μg)	m_d/m_r
0^+	110	110	4	4 %
0	110	110	9	8 %
-400	190	190	26	13 %
+400	120	120	30	25 %
-800	220	220	11	5 %
+800	160	160	38	24 %

$^+$Free ablation (no collar).

3.7 Discussion

Discharges in LPP's at increasing voltages show a significant increase in ion and electron signals. A characteristic signature is the appearance of a second ion peak as the discharge current is increased. Further increase in current sees this peak moving to earlier times with further peaks appearing as well.

By performing energy spectrum analysis and matching this to the ion probe signals, it was found that these peaks actually correspond to the formation of ionised species (AL II and Al III), as well as to the appearance of contaminant species, most notably ions of oxygen, hydrogen, carbon and nitrogen. This technique also revealed the presence of ions up to Al VIII at the higher discharge voltages.

Spectroscopic analysis shows an increase in electron temperature from 0.8 eV up to 4 eV (at -800 V discharge and 3 kA of current) and the appearance of significant emission from Al II and Al III ion transitions. This analysis also shows the higher temperatures are found towards the edge of the collar.

There is good agreement between the features observed with the Langmuir probe and time-resolved plume imaging. The latter shows the development of a mushroom-like structure with the onset of the discharge; this structure evolves into a slug of plasma that is expelled at $\sim 2\times10^6\ cm\ s^{-1}$. When comparing this to the ion probe signal at -400 V (Fig. 3.6), there are two notable peaks at 9 μs and 13 μs. The first corresponds to a velocity of $3\times10^6\ cm\ s^{-1}$ which is the expansion velocity of

the original laser produced plasma. The second, propagating at 2.1×10^6 cm s^{-1} matches the propagation velocity of the slug. Furthermore, the velocity spectrum dN/dv (Fig. 3.8) shows two peaks at 2 and 3.5 $\times 10^6$ cm s^{-1}as well. The first, which has a greater magnitude, matches the velocity of the slug, whilst the second peak matches the laser produced plasma velocity. One could, therefore, conclude that at moderate discharge voltages (-400 V), the current mostly affects the tail-end of the laser plasma plume, further heating and ionizing it. As the magnitude of the current is increased, practically the entire ablation plume is heated in the process.

Analysis of the cathode surface shows a growing erosion area stemming from the ablation pit, and which grows with increasing discharge current. Concentric rings and radial streaks suggest the propagation of vacuum arc spots from the center to the edge of the cathode.

Mass removal and film deposition results show an increase in deposited material when the central electrode is charged positively, whilst when charged negatively there appears to be some mechanism that prevents material deposition. One possibility is the presence of high energy ions sputtering the substrate.

The structure observed on the deposited films in the form of a ring with a nearly empty center suggests another possible mechanism could be *plasma focusing*. Although no strong evidence was found for this, it may very well explain this structure, as well as the often fluctuating ion probe signals, which often appeared to decrease at higher potentials. As detailed in Section 1.5, the azimuthal self-magnetic field can deflect ions at an angle proportional to charge. Therefore, for a given current, ions will have a focal length given by:

$$f = \frac{1}{\sqrt{K} sin(\phi)} \tag{3.1}$$

where ϕ is the phase and K is the focusing strength. Because the focusing strength depends on the current density, particle charge and ion momentum, plots showing the focusing distance as a function of current are shown in figure 3.48.

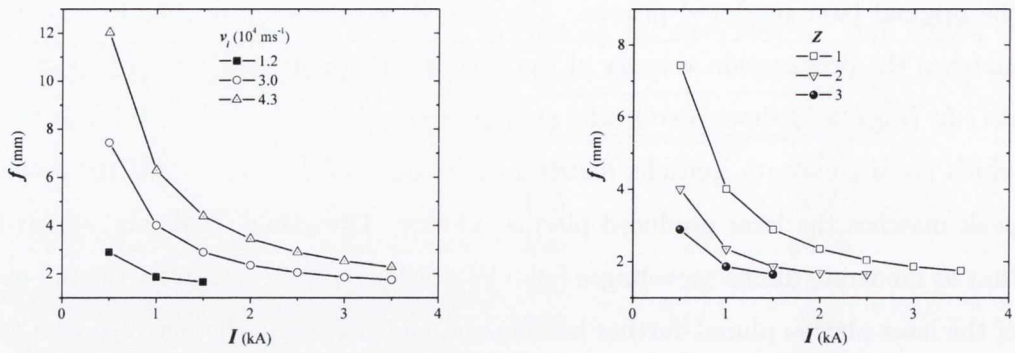

(a) (b)

Figure 3.48: Plasma self-focusing: focal length as a function of current for changing ion velocity (a) and ion charge (b).

The velocities used in Fig. 3.48(a) were taken from the velocity distribution of ions obtained from the Langmuir probe. Also, from the discharge structure inside the cell seen in Figs. 3.13 and 3.11, the above plots assume the current flows through a 1 mm conductor having a length of 3 mm.

An alternate effect that could be present in this (cylindrically-symmetric) geometry is the so-called hollow-charge, whereby a self-induced magnetic pinch is produced at the base of the cathode and *squeezes* the ions out the free end at high velocities [69].

Chapter 4

The Conical Nozzle Geometry

A coaxial geometry similar to the open collar was used, whereby a collar with a conical cross-section was placed over an inner cylindrical electrode (see Section 2.1). The laser pulse was focused along the axis via a 3 mm orifice onto an inner copper electrode having a 4 mm diameter and charged to both positive and negative potentials. Analysis techniques included ICCD imaging and spectroscopy, as well as simultaneous discharge monitoring and ion probe measurements.

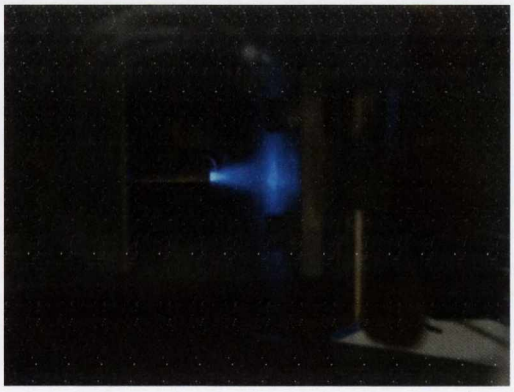

Figure 4.1: Plasma jet from conical nozzle discharge

4.1 The Discharge

Discharge voltage and current signals for this collar geometry are shown in Fig. 4.2(a-d) for both positively- and negatively-charged central electrode. Note these are very similar to the open-ended discharge signals (cf. Figs. 3.2 and 3.3). Indeed, the peak voltage and current values are equal both in time and in magnitude. This similarity is expected in the first instance, since the discharge path length (inter-electrode gap) is approximately the same in both cases.

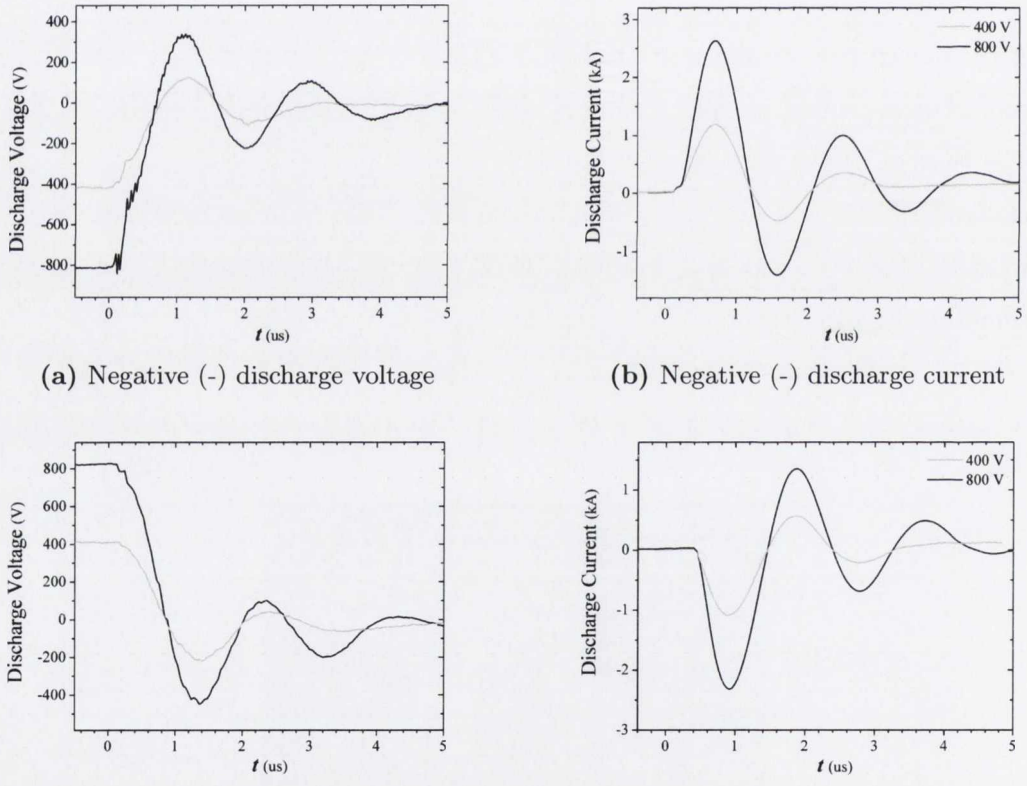

(a) Negative (-) discharge voltage

(b) Negative (-) discharge current

(c) Positive (+) discharge voltage

(d) Positive (+) discharge current

Figure 4.2: Voltage and current signals for ±400 and ±800 V discharge potentials. Central Al electrode was charged positive (+) or negative (-) as indicated (a-d).

4.2 Langmuir Probe Analysis

Probes were used both to monitor the plasma for the various diagnostic techniques as well as for the study of the plume expansion as a function of angle. The latter study was achievable due to the null disturbance of the discharge with a nearby probe, as opposed to the open collar case. The plots in Fig. 4.3(a-b) compare the probe signals for the positively- and negatively-charged cases at 10° from the gun axis. In the same figure are plots for the open case at positive and negative potentials as well.

In both cases the overall behaviour of the plume is similar to that observed in the open collar. Indeed, at 400 V the signal shows a similar characteristic second peak appearing at later times. At 800 V there is a strong increase in flux, with the signal becoming strongly peaked, especially when applying a positive potential. Note that the probe in the open case was placed at more than twice the distance z_p, and yet the signals are similar in duration. Although the plumes cannot be considered inertial in the strict sense, this is indicative of a longer-lasting event in the conical case.

In order to investigate the plume behaviour as a function of angle, ion signals were taken using a rotating probe, which scanned the plume at a constant radius (15 cm) from 10° to 90°. Figures 4.4, 4.5, 4.6 and 4.7 show the ion probe signals for increasing probe angle for a freely expanding plume, as well as for 0, -800 V and +800 V discharging. In order to compare the ionic distribution of the different discharge regimes, these signals were integrated to obtain an ion flux and are shown in Fig. 4.8 for 0 volts with -and without - the collar in place, as well as for ±400, ±800 V.

Figure 4.4 shows the angular behaviour of the plasma plume expected from a freely expanding plume, whereby the time of arrival of the ion peak moves to later times as the angle increases due to the semi-ellipsoidal expansion dynamics. When the collar is placed in front of the target (Fig. 4.5), the temporal distribution of the plume is observed to increase two-fold. Additionally, the magnitude of the ion current is observed to increase significantly and the signal drops off rapidly as the angle

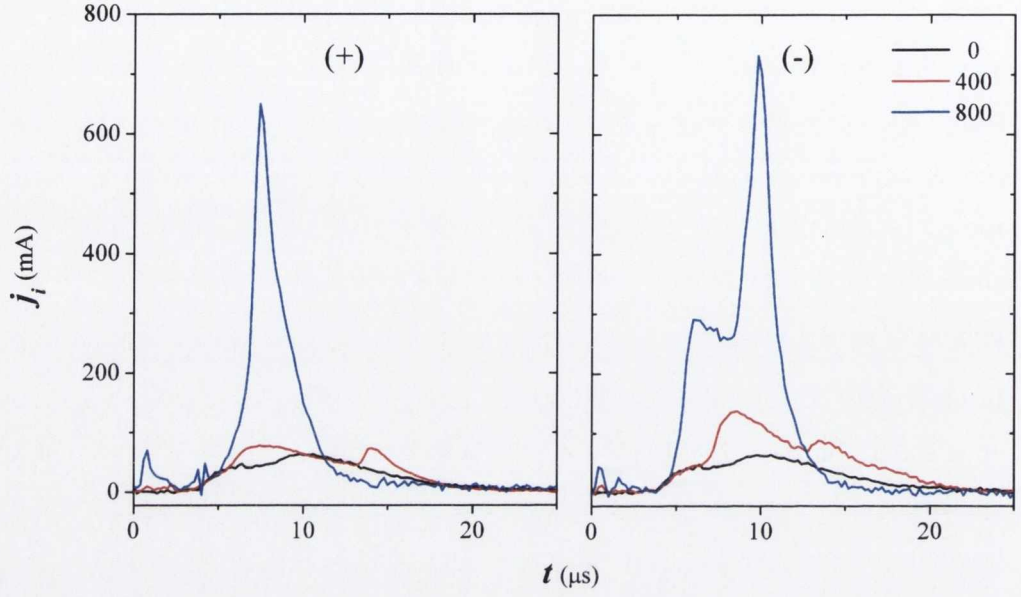

(a) Conical

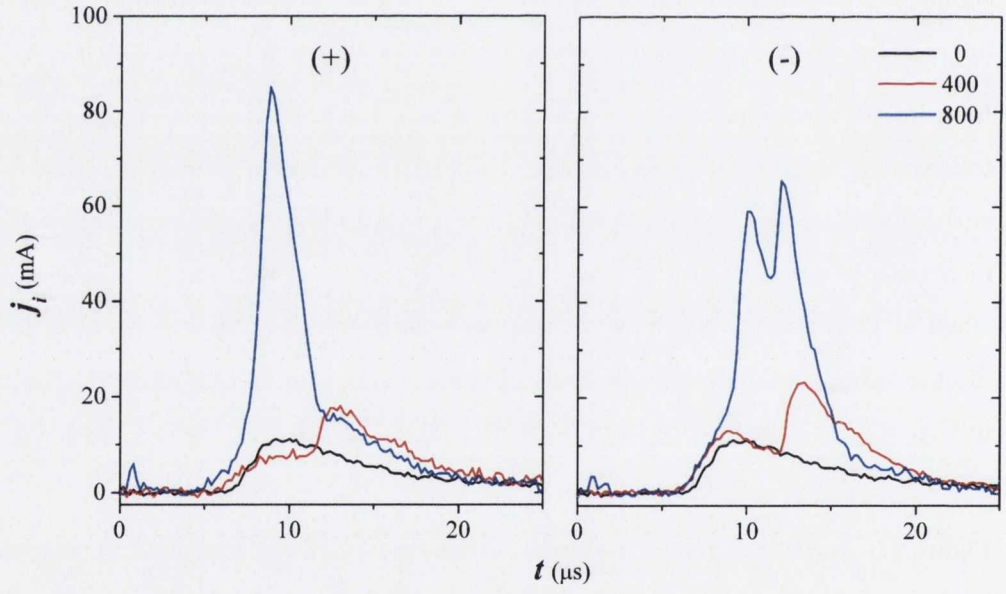

(b) Open

Figure 4.3: Ion probe signal comparison for positive and negative discharge configurations. (a): Conical; $z_p = 12$ cm. (b): Open; $z_p = 30$ cm.

increases. When comparing the two voltage cases (±800 V; Figs. 4.6 and 4.7) , the most striking feature is the peak separation observed at -800 V indicating possible 'fast' and 'slow' components of the plume. Conversely, at +800 V, only a single peak is observed throughout the scan.

From Fig. 4.8, it can be seen that the ions acquire a higher integrated flux when the collar is put in place, showing a three-fold increase in flux compared to free ablation. As the discharge potential is increased, the plume acquires an increasingly greater flux, an effect that is more notable with the negative case. Indeed, at 10° the negative discharges have twice the flux as their positive counterparts.

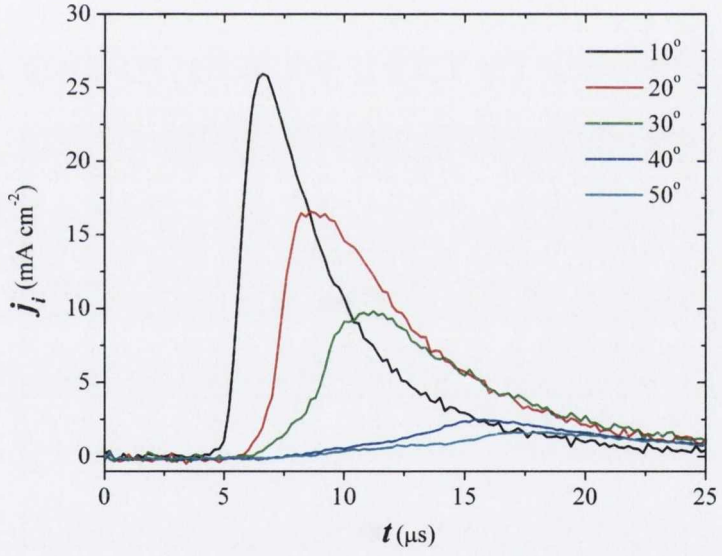

Figure 4.4: Ion current signals for increasing probe angle; 0 V free expansion.

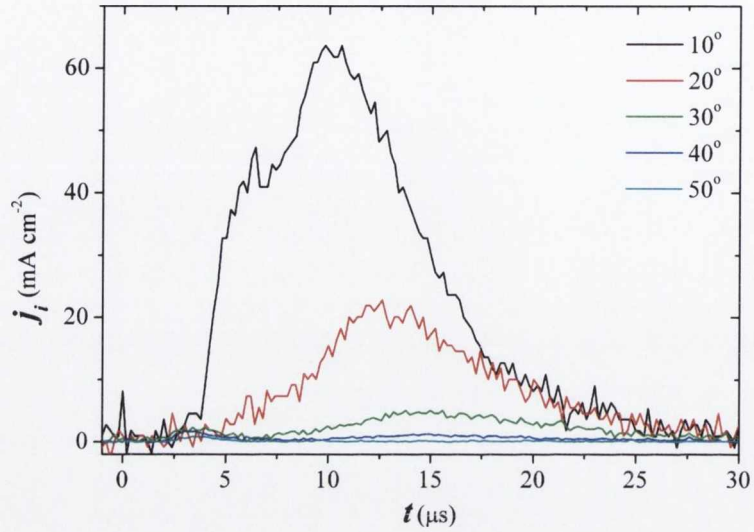

Figure 4.5: Ion current signals for increasing probe angle; 0 V.

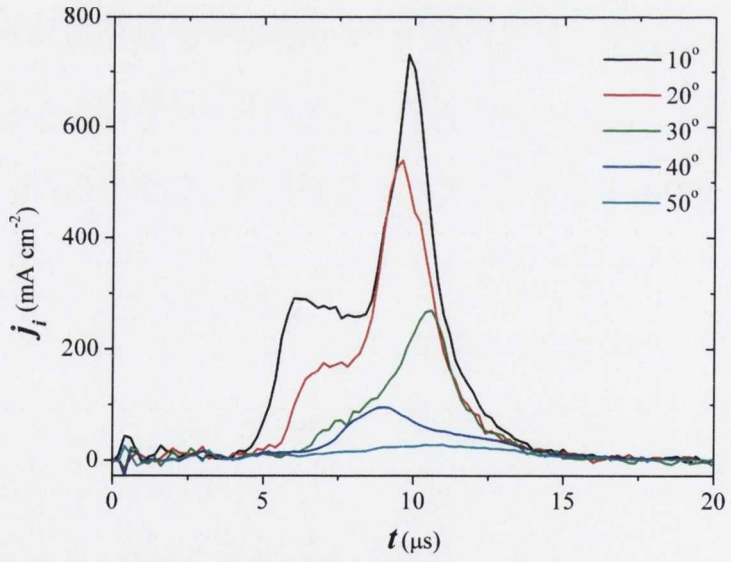

Figure 4.6: Ion current signals for increasing probe angle; -800 V

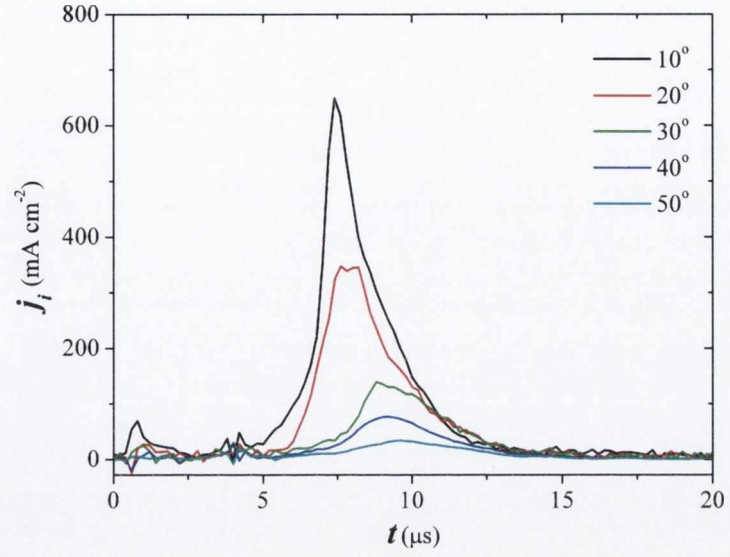

Figure 4.7: Ion current signals for increasing probe angle; 800 V.

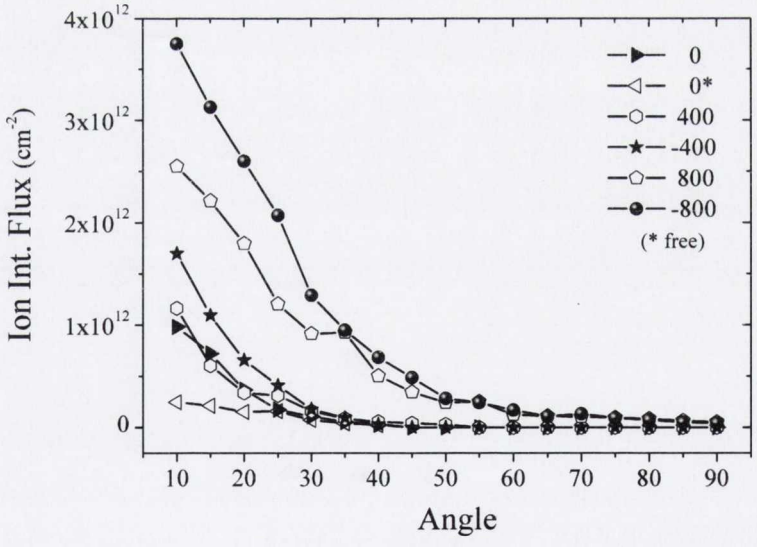

Figure 4.8: Ion angular distribution for conical collar. (* indicates free ablation with no collar)

4.3 ICCD Imaging

As with the open collar, simultaneous imaging and spatially-resolved spectra of the expanding plume were taken for varying time delay (Δt). Since there was no slit cut into the side of the collar, the plume was only observable once it exited the gun via the 3 mm orifice at the end. In addition to this, the plasma was relatively tenuous compared to the open case, and therefore, a longer gate time on the ICCD's was used ($\Delta\tau = 100$ ns). For this reason, although the analysis was done for 0, -400 and -800 V, the images shown in Figs. 4.9 and 4.10 will correspond to 0 V, +800 V and -800 V only, given the greater emission.

It can be noted in the sequence that images are shown after 800 ns. This is because a tenuous plasma barely begins to appear after 500 ns, which accounts for the time it takes to expand inside the collar and exit through the orifice. As shown in the previous section, the plasma has a higher flux with the collar in place even without the discharge, appearing as a thin emitting column in the images beyond 1 μs delay. The effects of the discharge also begin to show around 1 μs, where a highly forward-directed plume is observed. Figure 4.10 shows the sequence of images at later time delays where features characteristic of this geometry are observed; the most striking being a mushroom-shaped gas cloud seen at $\sim$3 μs. Presumably, the initial ablation plume begins to expand and as the discharge ensues, a second, faster plume is expelled which overtakes the first. This interaction produces the mushroom-like structure often seen in hydrodynamic phenomena, e.g. the expansion of a plasma plume within a background gas [70].

As noted previously, the central electrode was also charged positively. The difference in plume expansion between positive and negative discharges appears to be in the timing of the events previously described. The images show the development of an initial plasma jet to be at 1.2 μs for the negative case, whilst for the positive it occurs around 2 μs. Likewise, the shockwave structure appears at the rightmost area of the images at 3.5 μs (negative) and 4 μs (positive). This retarding effect of 500-700 ns can be explained by the central electrode being initially 'hot', i.e. being

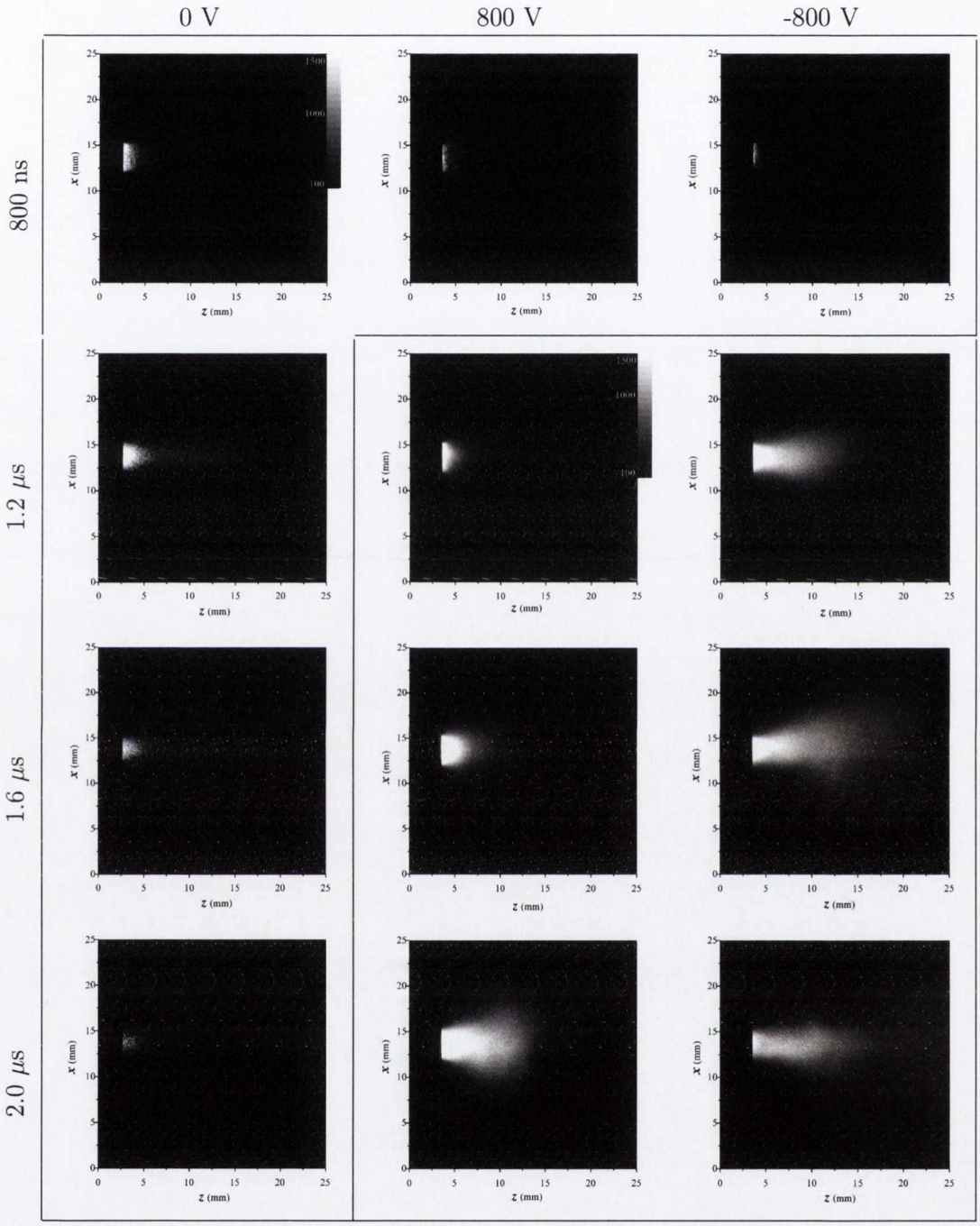

Figure 4.9: Time-resolved image sequence comparing 0 and -800 V discharge potentials in conical collar. Regions indicate two different (logarithmic) intensity scales.

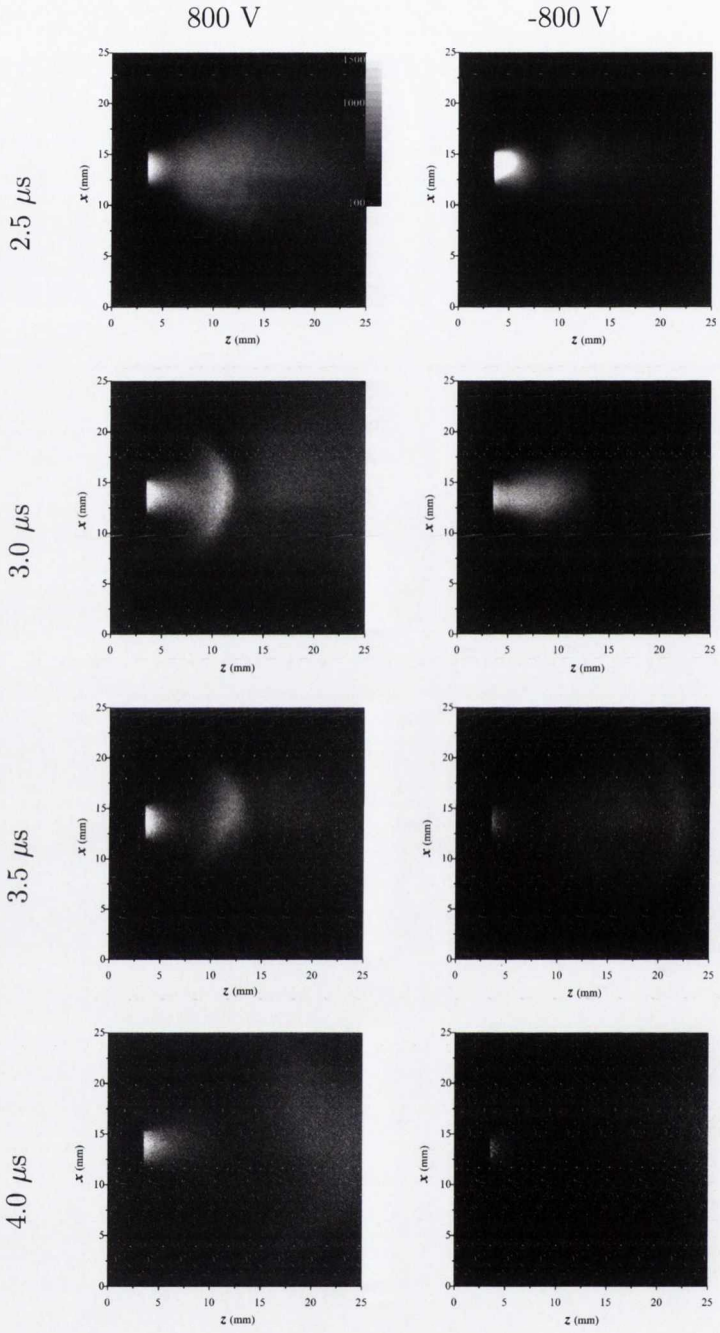

Figure 4.10: Time-resolved image sequence comparing 0 and -800 V discharge potentials in conical collar. Logarithmic intensity scale.

the source of electrons when the laser plume begins expanding and the discharge ensues. Conversely, when the central electrode is 'cold', i.e. electrons are drawn from a more diffuse source (the collar) and there are less available electrons as the discharge begins.

4.4 Spectroscopy

Images showing the spatial evolution of the spectral lines are displayed in Figs. 4.11 and 4.12, comparing 0, +800 V and -800 V. These images were taken simultaneously with the ICCD images, and are roughly on the same scale.

One can note once again that the temporal evolution of plume expansion is different in both polarity cases, with the positive case lagging by ~500 ns; furthermore, the spectral lines are quite different as well. At zero volts only three lines in the 450 nm region can be observed, belonging to neutral copper. On the other hand, as the discharge is applied, a series of lines corresponding to both aluminium and copper transitions appear (recall the inner electrode is copper and the outer collar is aluminium). When comparing both polarity cases, distinctive transitions are noted depending on the direction of current flow. The main lines seen in both polarity cases are tagged in the spectra shown in Figs. 4.13, 4.14 and 4.15.

Note that the majority of lines in both discharge cases are neutral and singly-ionised Al and Cu, with the exception of a couple of tenuous Al III lines. This is in stark contrast with the open collar case, where -800 V discharges produced doubly ionised species of aluminium. The energy diagram for Cu I is shown in Fig. 4.16 [33, 71].

Determination of electron temperatures using the copper transitions from lines in Figs. 4.14 and 4.15 proved difficult, given the limited information on copper spectroscopic data. Exceptions to this were the transitions appearing without a discharge, corresponding to the lines at 510, 515 and 521 nm. Since the latter two lines come from the same transition, i.e. the energy difference of the upper levels is much less than 1 eV, only the ratio of the 515 nm line with the 510 nm line was taken when

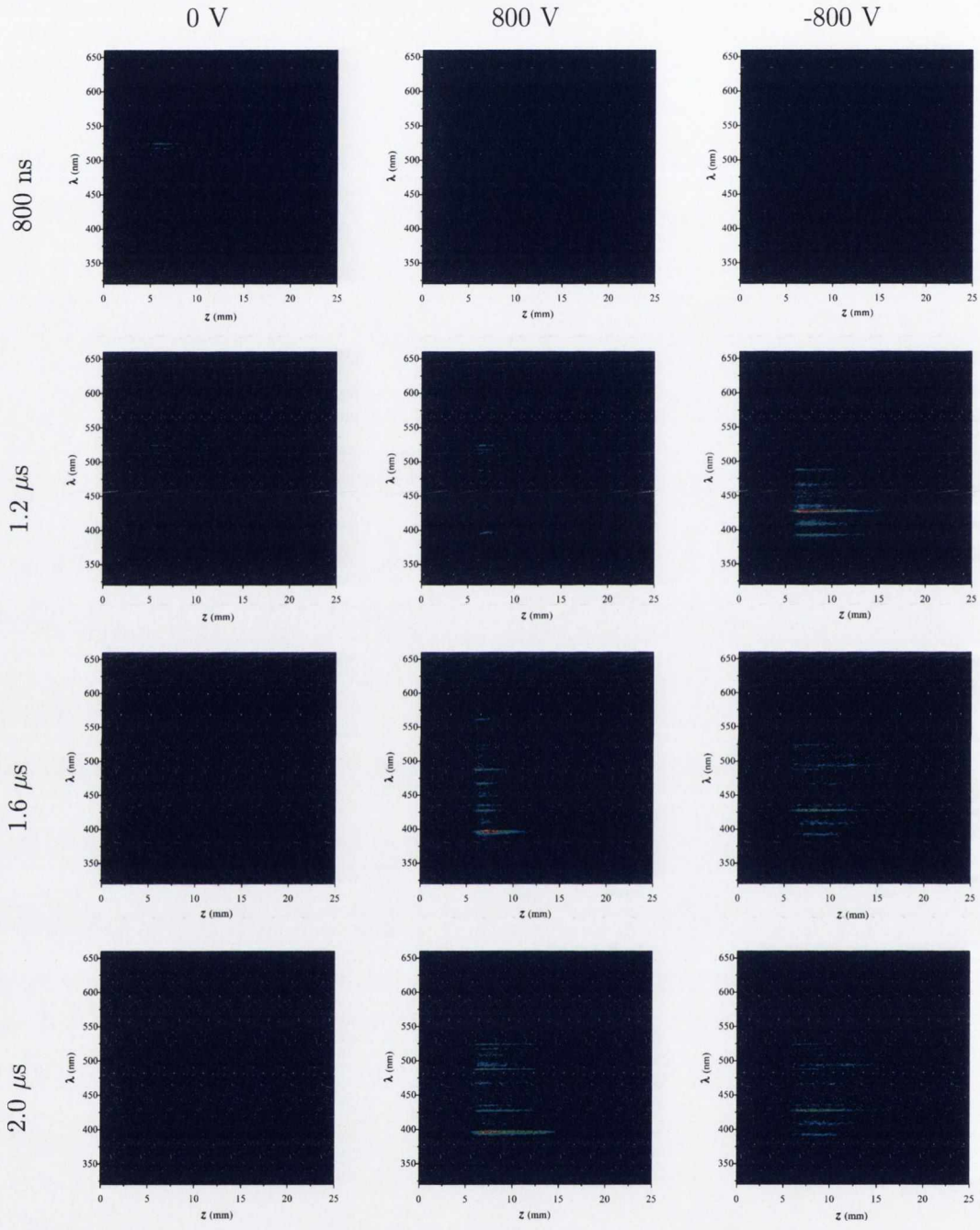

Figure 4.11: Time-resolved image sequence comparing 0 and -800 V discharge potentials in conical collar.

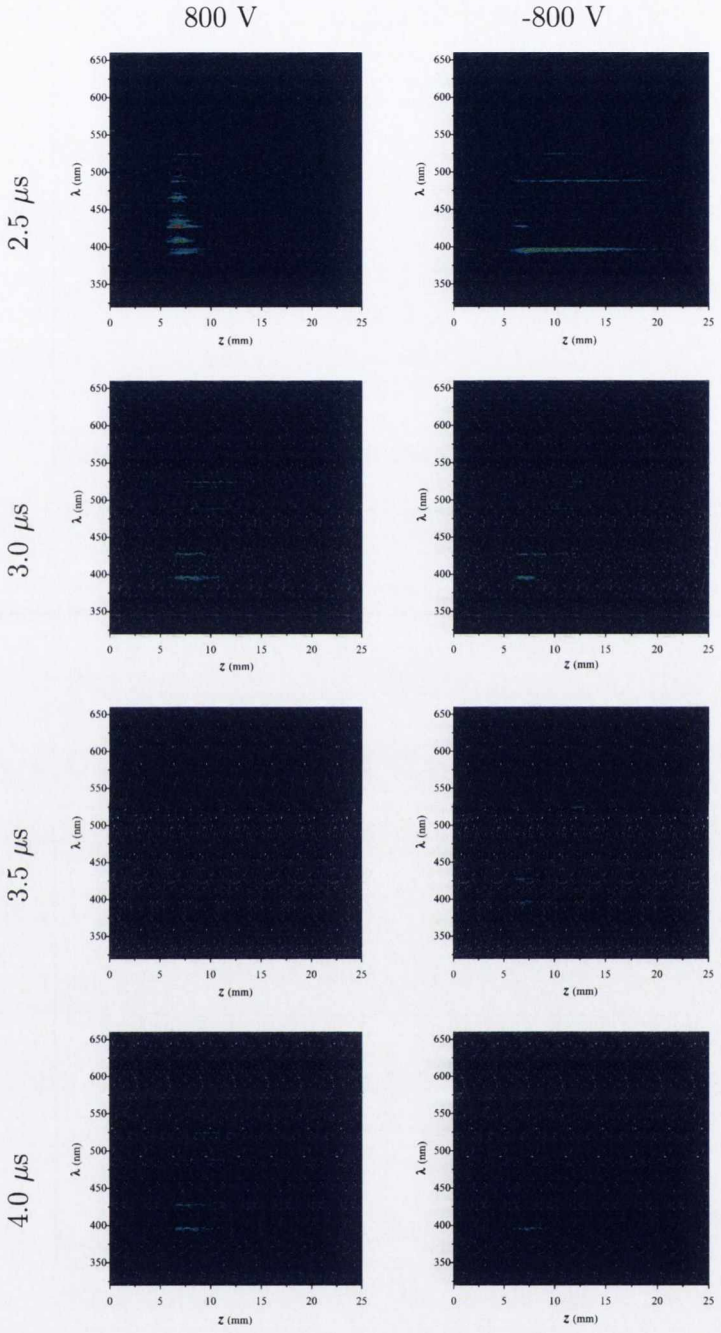

Figure 4.12: Time-resolved image sequence comparing 800 and -800 V discharge potentials in conical collar.

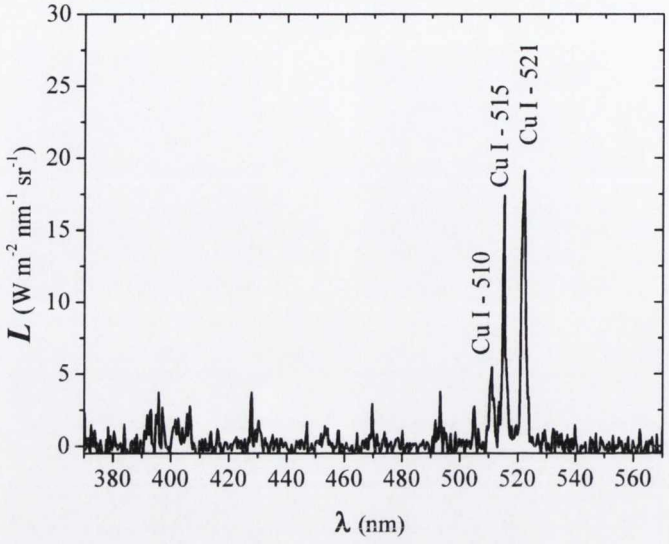

Figure 4.13: Spectral line identification for 0 V discharge potential

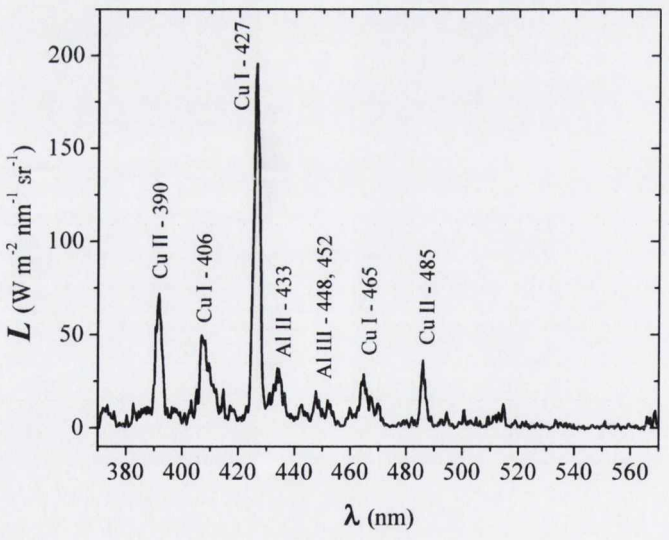

Figure 4.14: Spectral line identification for -800 V discharge potential

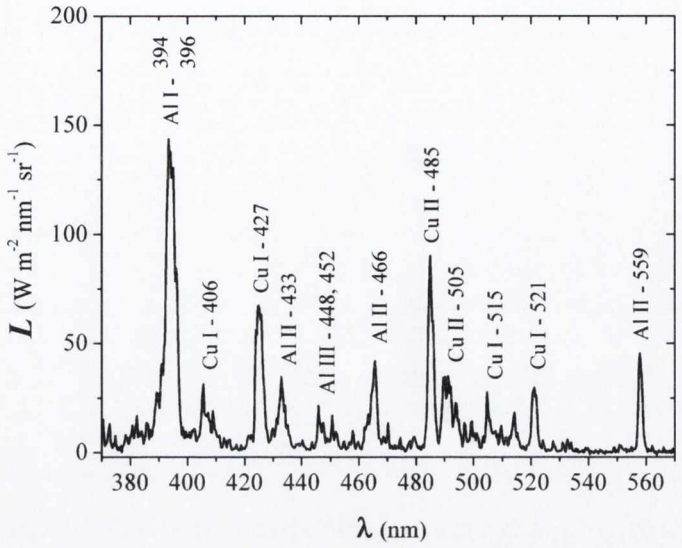

Figure 4.15: Spectral line identification for +800 V discharge potential

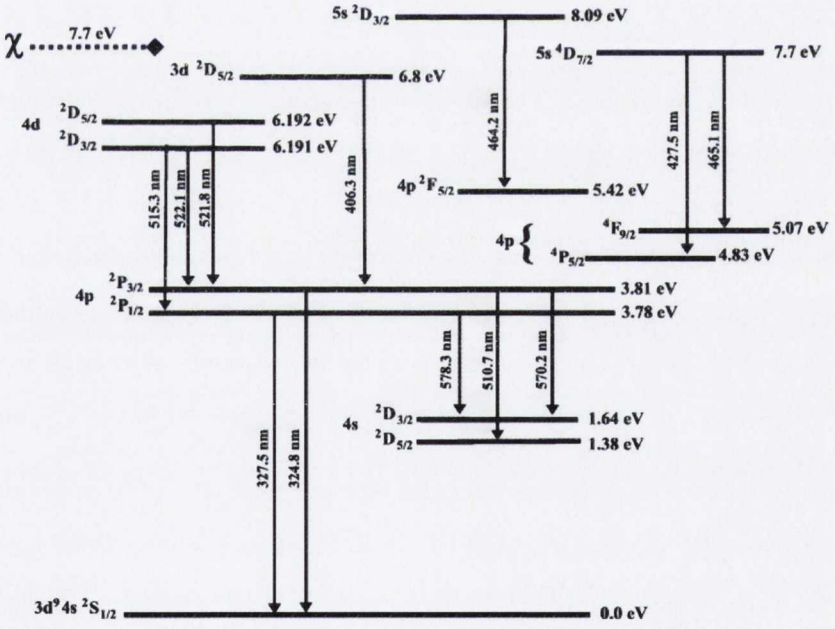

Figure 4.16: Cu I energy level diagram; (χ- ionisation potential)

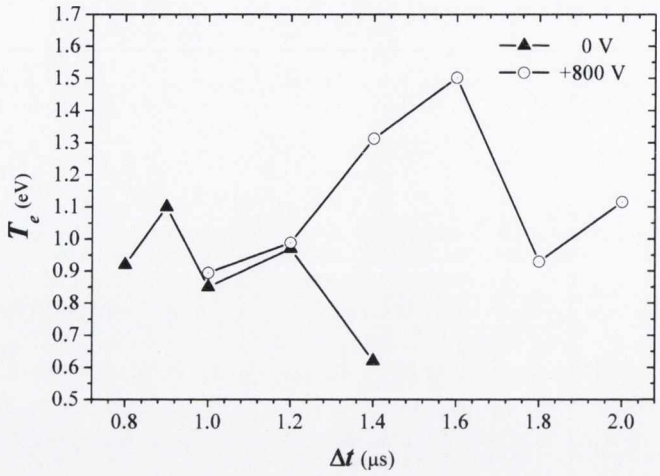

Figure 4.17: Electron temperature at nozzle exit as a function of time delay. Cu I line ratios were used for 0 V (-△-); Al II line ratios were used for +800 V (-○-).

calculating T_e. For the +800 V discharge case, on the other hand, aluminium transitions at 466 and 559 nm (Al II) were used to estimate the plasma temperature at the nozzle exit for different time delays. Thus, using copper lines for zero volts and aluminium lines for the discharge, a plot of temperature as a function of time delay (Δt) is obtained (Fig. 4.17).

The maximum temperature at the nozzle exit, when no discharge is present, reaches 1.1 eV after 900 ns time delay from the arrival of the laser pulse. As the discharge ensues, the plasma temperature increases, reaching a maximum of 1.5 eV at 1.6 μs. Note that this maximum temperature is lower than the one recorded in the open case for the same discharge potential (2.5 eV). Plasma ion density estimates using Stark broadening were also calculated for this experiment. Although in the open case no aluminium lines were visibly broadened, the Cu I line at 427 nm showed significant broadening during the discharge.

Computing the broadening calculations from Section 1.2.4, an estimate of ion density at the nozzle exit was obtained as a function of time delay. The Stark width parameter was taken from the literature, which at 10,000 K (~1 eV) is: $w = 0.8$ [33]. In the density calculations, the instrumental width was subtracted from the Stark widths as: $\Delta\lambda_F = \Delta\lambda_S - \Delta\lambda_I$ to obtain a final result [72]. Although dispersion

estimates for the spectrometer resolution (300 l/mm grating) give 0.65 nm, experiments suggested an instrumental broadening of $\Delta\lambda_I = 1$ nm. Table 4.1 shows the measured widths in the experiments, the values after subtracting $\Delta\lambda_F$ and the estimated densities. As discussed previously, other broadening terms such as Doppler and Van Der Waals are negligible.

To show the increase in density when the discharge is present, the data from Table 4.1 is plotted in Fig. 4.18 and compared with the free ablation density profile of the LPP; this signal was taken from ion probe measurements and scaled to 1 cm from the target using self-similar theory. As the plots show, the density exceeds 10^{17} cm^{-3} when computing the Stark measurements, whilst the ion probe in free ablation gives an estimate of 6×10^{16} cm^{-3} maximum , showing an almost two-fold increase in density with the discharge. In order to determine the extent of hydrodynamic compression alone (forcing an expanding gas through a reducing cross-section), it would be advantageous to determine how the density is affected by placing the nozzle in place with no discharge. This measurement, however, was not done, and although probe measurements were taken for the angular distribution measurements, self-similar theory cannot be used. Some conjectures will be drawn in the conclusion of this chapter.

Table 4.1: Stark widths of Cu I: 427 nm line (measured- $\Delta\lambda_S$; final- $\Delta\lambda_F$) and electron densities n_i as a function of time after laser arrival.

t (μs)	$\Delta\lambda_S$ (Å)	$\Delta\lambda_F$ (Å)	n_i ($\times 10^{16}$ cm^{-3})
1.0	25.6	15.6	9.7
1.2	26.0	16.0	10
1.4	24.0	14.0	8.9
1.6	30.3	20.3	13
1.8	26.7	16.7	10
2.0	23.0	13.0	8.1

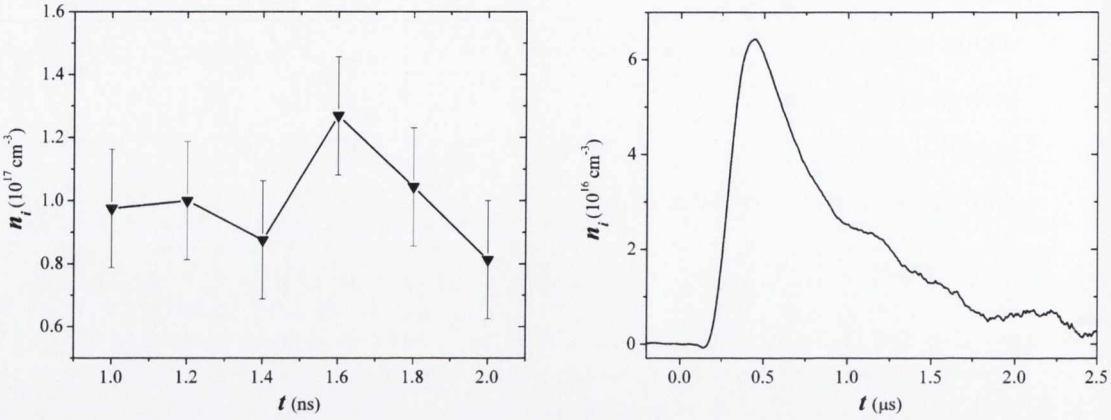

Figure 4.18: Comparison of ion density from Stark broadening as a function of time delay; +800 V (a) and LPP density at 1 cm from target (b).

4.5 Mass Removal

Thin film deposition trials were largely unsuccessful, mostly due to geometrical constraints. Because the gun axis and incoming laser pulse were colinear, placing a substrate in front of the gun exit proved difficult. By cutting a 5 mm hole in an acetate slide it was possible to bring the laser through into the gun, however, very little material made it to the substrate. Notwithstanding, mass removal rates were measured for the different polarity cases (0, ±400 V and ±800 V) following 1000 shots and using the same weighing technique described in the open geometry. These results are shown in Table 4.2 and are compared to the mass loss measurements from the open collar geometry.

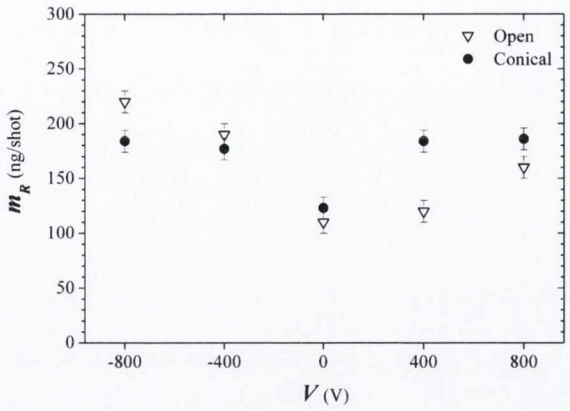

Figure 4.19: Comparison of mass removal rates using conical and open-ended collar geometries.

Table 4.2: Mass removal rate of Cu targets for varying discharge voltage; m^c- conical; m^o- open.

V (volts)	m_r^c (ng/shot)	m_r^o (ng/shot)
0	163	110
-400	177	190
+400	184	120
-800	184	220
+800	186	160

The plot in Fig. 4.19 shows the mass removal rates from Table 4.2. This plot shows an increase in removal rate when applying the discharge, presumably via arcing. A greater uniformity in the mass removal is observed when using the conical collar, with values between 160 - 180 ng/shot. On the other hand, mass removal in the open case shows a greater difference between positive and negative potentials at the central electrode. The higher rates being observed for the latter case.

4.6 Discussion

The characteristics of the discharge are much the same as with the open case, where the current and voltage drop across the capacitor have the same temporal behaviour

and peak values. Again, the current has a period of ~1 μs and a peak value of 2.8 kA.

Ion signals behave much the same as well, having an increase in ion current and the appearance of multiple, sharp peaks with the onset of the discharge. Probe measurements were also carried out as a function of angle, comparing both polarity cases for a range of voltages. Results show similar peak distributions in all cases, with the particular feature that the negatively-charged centre electrode produces an overall higher flux than the positive case. This same plot also shows that the plume has a higher flux when the collar is in place (as opposed to free ablation), which suggests collimation.

ICCD imaging shows a jet-like structure exiting the nozzle with no discharge present having a width similar to the nozzle exit (3 mm). This, again, suggests collimation of the LPP. The onset of the discharge shows a brightly-emitting plume, although this doesn't show the same high collimation observed without a discharge. In this case, the plume appears to expand at the angle of the inner cone, which subtends $\sim 40°$. As the discharge evolves, a shockwave develops as a second slug of plasma expands at a higher velocity than the first. The source of electron emission during the discharge, i.e. whether the central electrode is initially *hot* or *cold* also bears on the time these features appear. An initially *cold* electrode seems to inhibit the initial plume expansion, and the main plasma jet appears around 1.2 μs after the discharge onset ($\Delta t = 2$ μs), presumably when the current reverses. On the other hand, having a *hot* central electrode at the initial discharge stage means the plasma jet appears around 400 ns after the discharge onset ($\Delta t = 1.2$ μs).

Comparing the ICCD images to probe measurements, there is good agreement between the plume and shockwave front velocities with the peaks in the ion probe signals.

1. Discharge 0 V: Plume expansion through the nozzle is seen in the images (Fig. 4.9 $\Delta t = 1.6$ and 2.0 μs) as a thin jet expanding at a velocity $v_p \approx 2 \times 10^6 cm\ s^{-1}$. The probe signal corresponding to these images (Fig. 4.5[10°])

has two features at 6 and 11 μs, which translates to velocities of 2 and $1\times10^6 cm\ s^{-1}$ respectively; this implies that the jet observed is actually the first peak in the probe signal. Seemingly, the second feature is not captured by the ICCD.

2. Discharge -800 V: The probe signal (Fig. 4.6[10°]) has two main peaks appearing at 6 and 9 μs. Referring to the ICCD images, the first jet of plasma expelled from the gun has a plume front velocity of $v_p \approx 2 \times 10^6 cm\ s^{-1}$(Fig. 4.9 $\Delta t = 1.2$ and 1.6 μs), which matches the velocity of the first peak of the probe. The second peak is due to the shockwave observed in Fig. 4.10 at $\Delta t = 3.5\mu$s, which is also observed to propagate at $v_p \approx 2 \times 10^6 cm\ s^{-1}$.

3. Discharge +800 V: This case does not agree as well as the previous two. The probe signal seen in Fig. 4.7[10°] has a single peak appearing at $\sim7\mu$s. On the other hand, the initial plasma jet, as observed by the ICCD, expands at $v_p \approx 1.2 \times 10^6 cm\ s^{-1}$, and furthermore, is seen to be expelled about 800 ns later than the in the negative case. Based on these assumptions of velocity and temporal delay, the peak would be expected to appear in the ion signals at $\sim$11 μs. There is also no sign of the shockwave signal observed in Fig. 4.10 ($\Delta t = 3.5\mu$s).

Spectroscopic studies show a different emission spectrum for the positive and negative cases (recall central electrode was Cu and outer collar was Al):

1. In the -800 V case, which was difficult to follow up with temperature and density measurements, shows the appearance of new Cu I species (when comparing to the LPP spectrum). As seen on the energy level diagram, the transitions of these new species correspond to higher lying transitions; some above the ionisation potential.

2. The +800 V case, on the other hand, appears to have a complex combination of aluminium and copper ions, the former having up to Al III and the latter up to Cu II. Electron temperature calculations from Al line irradiance ratios

show a slight increase from 0.9 eV to 1.5 eV; the peak value occurring at 1.6 μs. Density calculations from Stark broadening show an almost two-fold increase in density, when compared with the peak density calculated via probe data. There are various mechanisms which may be responsible for this increase, such as current flow and reversal, electrode erosion, heating and the reducing cross section (which is inversely proportional to density via the mass flow equation [73]). Also note that both the density and temperature maxima occur at 1.6 μs, which is the time of maximum current in the reverse direction.

When comparing the mass removal with the open case, the conical nozzle has a slightly greater removal rate in the positive polarity, as opposed to the open case, which has a higher removal rate when negatively charged.

Chapter 5

Z-Pinch in Collimated Plasma

The main objective of these experiments was to characterise the laser produced plasma going through an aperture, in an attempt to produce a Z-pinch. By passing a fast, high-current discharge through a column of plasma, the Lorentz force in the induced magnetic field will collapse the radius within a given time-frame. As detailed in Section 1.4, a Z-pinch depends on the balance between the magnetic and plasma pressures, as seen in Bennett's condition. Recall equation 1.51: $8\pi(Z+1)N_i^l kT = \mu_0 I_a^2$ where N_i^l is the ion line density, kT the electron temperature and I_a is the current flowing through a column of radius a.

This experiment consists of driving a LPP through an aperture of fixed diameter in order to collimate the plasma. This same aperture serves as the plasma intake for the discharge cell, having a cylindrically-symmetric geometry (see Fig. 5.1), which as in the previous cases, is charged up to 1 kV. Using self-similar theory, the laser ablation plasma was characterized *a priori* in order to determine the plume density as a function of time and distance in the region of the cell. This same theory allowed the estimation of the ion line density N_i^l, required for Bennett's

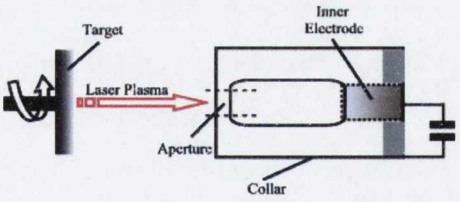

Figure 5.1: Collimating plasma collar

relation. The experimental setup is detailed in Section 2.1. The cell aperture, having an aperture of 3 mm, was placed at 1 cm from a rotating Al target. The cylindrical cell had a diameter of 1 cm and an inter-electrode gap of 1 cm; the anode on the side opposite the aperture was copper. The discharge circuit was the same one used in the previous cases.

The LPP was characterized by Langmuir probe analysis. As seen in Fig. 5.2(a), the original ion signal was recorded at 11.5 cm from the rotating target. By using the relations discussed in Section 2.3, the density as a function of time as this same distance is shown in Fig. 5.2(b).

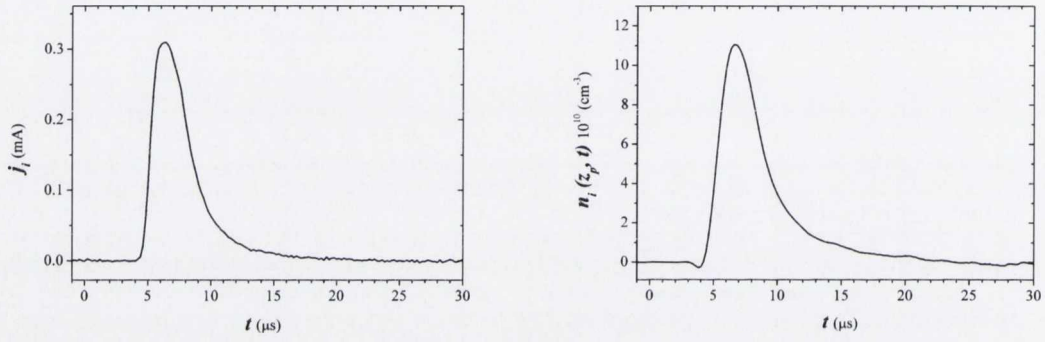

Figure 5.2: Ion probe signal (a) and resulting ion density (b) of LPP at 11.5 cm from target.

Using self-similar theory, density as a function of time can be calculated for the distance of the aperture and cell interior; which are between 1 and 2 cm from the target. Therefore density calculations are shown for 1 cm, 1.5 cm and 2 cm (Fig. 5.3(a). As mentioned in Section 2.3, ion densities derived from the probe signals can also be plotted in the form of density as a function of distance z. By using Eqs. 2.13 and 2.14, whilst choosing the time t' when maximum density is attained, one obtains the plots shown in Fig. 5.3(b). From this plot it can be inferred that the most uniform plasma density inside the discharge cell (between 1 and 2 cm) will occur at $\sim$1 μs, having an ion density of $\sim 5 \times 10^{13}$ cm^{-3}.

From the density profiles, the ion *line* density N_i^l as a function of distance can be estimated. Taking into account the aperture size A and aperture distance from the

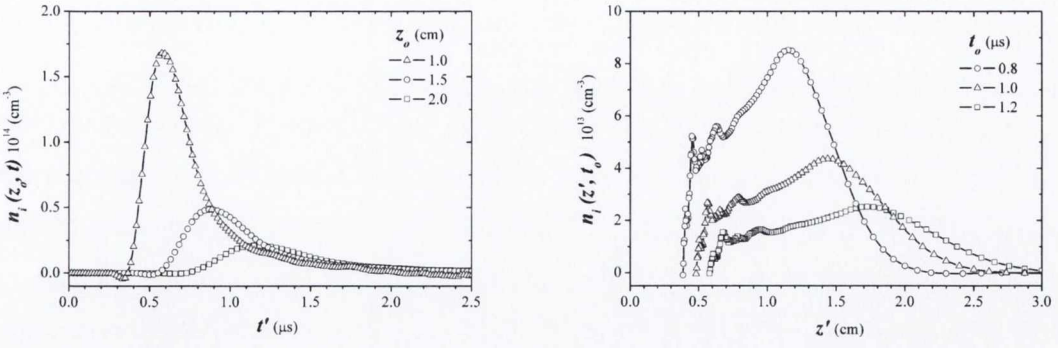

(a) (b)

Figure 5.3: Self-similar estimates of ion density as a function of time t' (a) and as a function of distance z' (b).

target z_A, the following relation gives the line density:

$$N_i^l(z', t_0) = n' A \left(\frac{z'}{z_A} \right) \tag{5.1}$$

Figure 5.4 shows a plot of the line densities as a function of distance z' and for varying times t_0 as in Fig. 5.3(b). This figure implies the line density is most uniform around 1 μs, having a peak density of 7×10^{12} cm^{-1}.

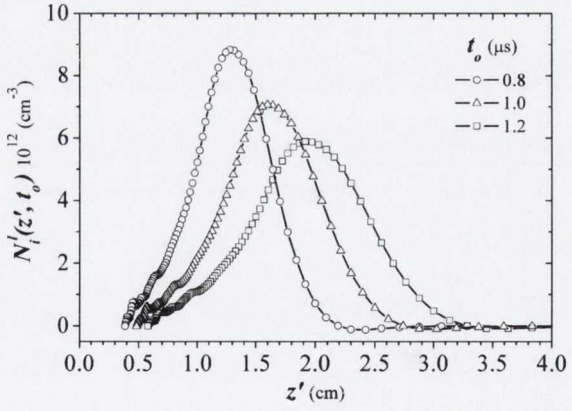

Figure 5.4: Ion line density estimates for 3 mm aperture at z_A =1 cm plotted as a function of distance from target.

5.1 ICCD Imaging

As described above, the distance from the rotating target to aperture was 1 cm, whilst the distance from aperture to anode was also 1 cm. This entire space was captured with the imaging ICCD, providing information on the dynamics of both the expanding laser produced plasma as well as the discharge within the cell. A composite image is shown in Fig. 5.5, indicating where the target, aperture and anode are observed within each image.

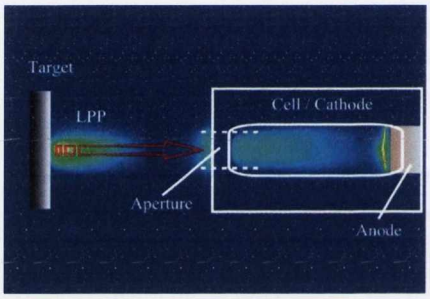

Figure 5.5: Composite image/schematic showing target and cell position in ICCD image.

Figure 5.6(a-f) shows an image sequence for changing time delay of the laser produced plasma and 400 V discharge. The left column (Figs. 5.6(a-c)) shows the initial LPP plume expansion up to 400 ns, where the plasma is seen to start off as a thin layer of plasma at 0 ns, and reaching out to ~8 mm from the target. The right hand column of images (Figs. 5.6(d-f)) shows the discharge onset starting at 900 ns in 100 ns increments. Initially, the plasma column has the diameter of the aperture, and appears contracted towards the anode. As the discharge evolves, the entire plasma column appears to contract, becoming unstable at at 1.1 μs, and displaying characteristic kink and sausage instabilities; from this time onward, the anode is seen to be responsible for most of the emission up to ~1.8 μs.

The current and voltage signals are shown in Figs. 5.7(a-b), where it is clear from the signal that the current begins to flow at approximately 1 μs, with the 800 V case beginning ~100 ns later than at 400 V. This can likewise be seen in the voltage onset, which begins ~150 ns later for the higher voltage. This same temporal difference was also observed in imaging, where evidence of the discharge through the plasma was seen at a later time for the higher voltage. It must be noted that the temporal

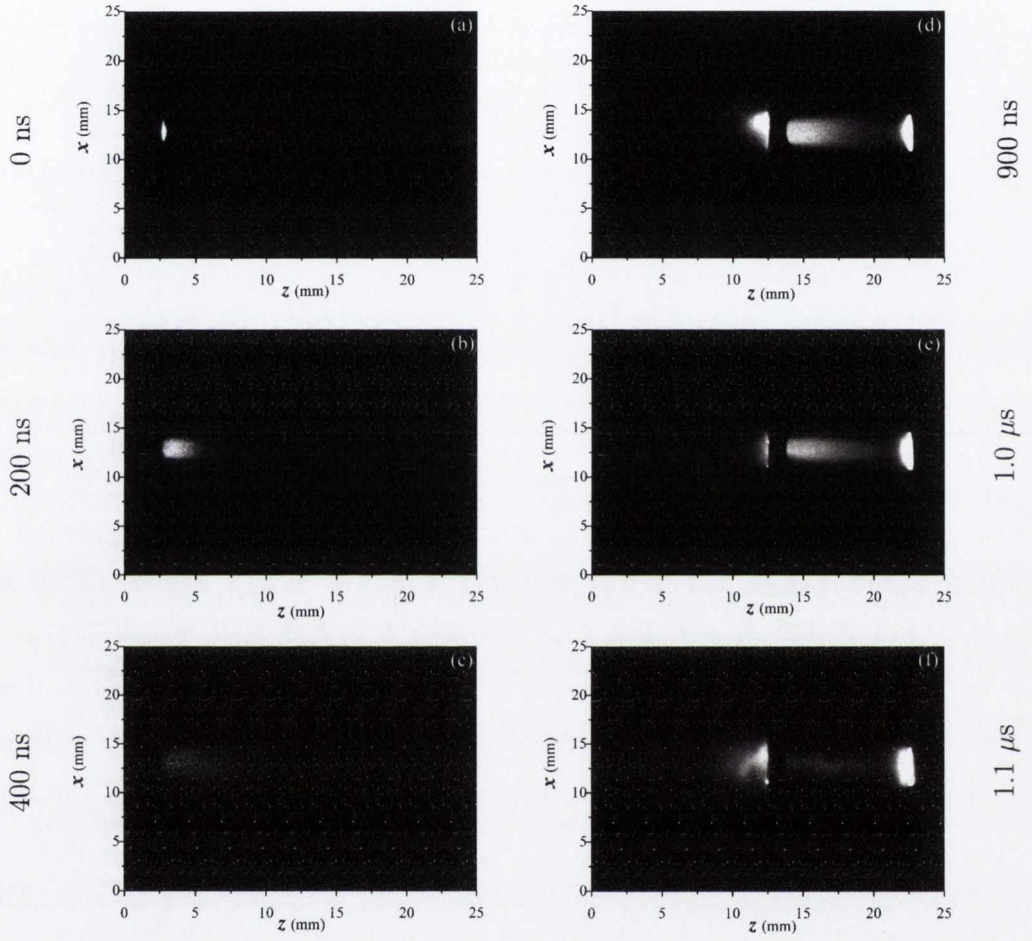

Figure 5.6: Images of the emission from the laser ablation plasma (left), and 400 volt Z-pinch plasma (right) at various time delays after the laser pulse (a) 0; (b) 200 ns; (c) 400 ns; (d) 900 ns; (e) 1 μs; (f) 1.1 μs. Gate time $\Delta\tau = 50$ ns.

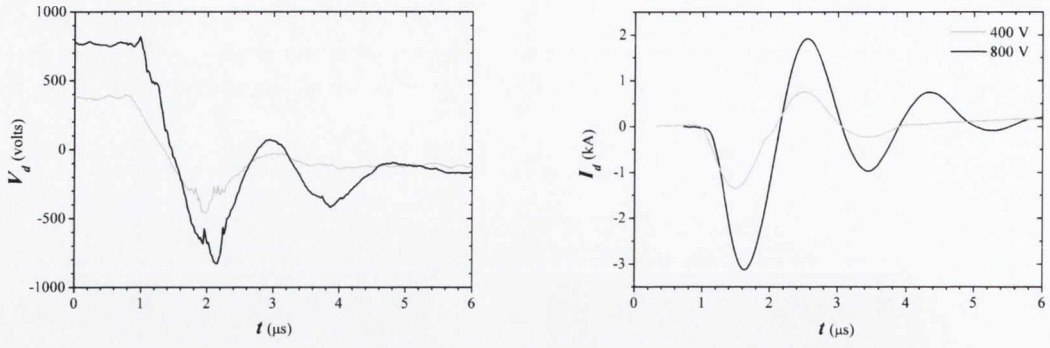

(a) (b)

Figure 5.7: Discharge signals for 400 V and 800 V. (a) Voltage drop across capacitor. (b) Current from live anode.

jitter in these experiments was high compared to the other two geometries studied herein, having a value of: ±80 ns. It is likely that this is due to the larger distance from the plasma source (target) to the discharge cell, where factors such as target morphology will affect the shot-to-shot plume expansion. In both cases the period of the damped current waveform is the same ($T = 1.9$ μs).

From the images at 400 V, it is apparent that the magnetic constriction of the plasma column actually occurs at the very start of current flow. A series of images was taken using the sub-image feature of the ICCD. This technique allows the capture of regions with lower emission, which are generally invisible when the camera software integrates the minimum and maximum intensities. The image sequence shown in Fig. 5.8(a-d) shows contour plots of the normalized emission from the plasma column, just as current begins to flow and magnetic constriction (Z-pinch) occurs. The images show the plasma as it enters the cell (Fig. 5.8(a)) with an initial width equal to the aperture diameter (3 mm). As the plasma reaches the anode at the opposite end of the cell and current begins to flow, evidence of self-magnetic constriction is seen where the rightmost part of the column is less than 2 mm wide (Fig. 5.8(b)). Further temporal evolution shows the development of an MHD sausage instability with a column diameter ranging between 1 and 2.5 mm (Fig. 5.8(c)); this instability is thought to dissipate rapidly as the plasma in the plume largely accumulates at the anode surface (Fig. 5.8(d)). This phenomenon of plasma 'piling up' on the anode is

not unexpected; estimates in Fig. 5.4 show that at 1.2 μs nearly half of the plasma has propagated to a plane 2 cm from the target, which is the actual position of the anode. Indeed, from the ICCD images shown previously, one notes strong emission coming from the anode surface, even at the early stages of the discharge. This issue will be further discussed in the following section.

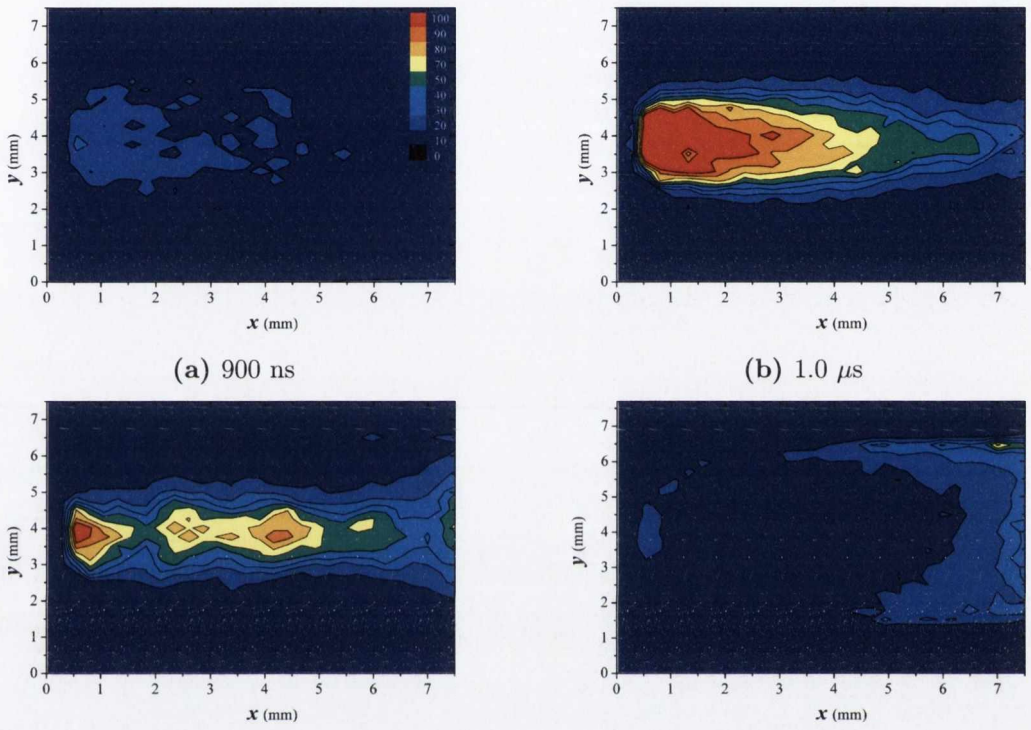

(a) 900 ns (b) 1.0 μs

(c) 1.1 μs (d) 1.2 μs

Figure 5.8: Normalised emission contour plots of Z-pinch evolution; 600 V discharge.

5.2 Spectroscopy

In order to capture the evolution of both the laser produced plasma and the effect of the discharge inside the cell, both were imaged onto the spectrometer slit, having a spatial de-magnification of $\sim 1/7$. In this particular experiment a different ICCD camera attached to the spectrometer was used, having a 1024×1024 pixel area (instead of 1024×256). The schematic in Fig. 5.9 shows how the images are to be

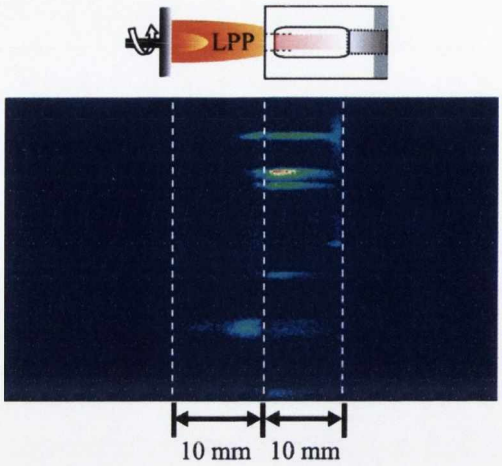

Figure 5.9: Composite image/schematic showing target and cell position in spectrum image.

interpreted, with the expanding LPP on the LHS and the discharge cell window on RHS. Following the ICCD images shown previously (Fig. 5.6(a-f)), spectral images are shown for the same time delays, with and without discharging, in Fig. 5.10(a-f). The images shown in Figs. 5.10(a-c) show the continuum produced at the arrival of the laser on the target and subsequent evolution of the neutral Al lines at 394, 396 nm. As the 400 volt discharge is triggered (at ~800 ns) the original LPP spectral line (394, 396 nm) increases in irradiance at first (5.10(d)) and then gives way to much more intense lines of Al II (466 nm) and Al III (371, 415, 448 and 452 nm) inside the cell. Some of these same lines are also seen at the outer edge of the cell, showing greater irradiance for certain time delays (e.g. Fig. 5.10(f) at 1.1 μs); this effect is likely due to the interaction of the outgoing discharge plasma with the still-incoming LPP. The images show this effect as well, where a shockwave develops at the aperture and expands back towards the target (Fig. 5.6(f)).

Given the complexity of this discharge system, where lines at different times and regions show widely varying behaviour, different sections were taken separately in order to analyse the spectral information, namely, the target (3 mm from surface), the central area of cell and the anode. Figures 5.11, 5.12 and 5.13 show time-dependent lineouts at relevant intervals for each of these regions.

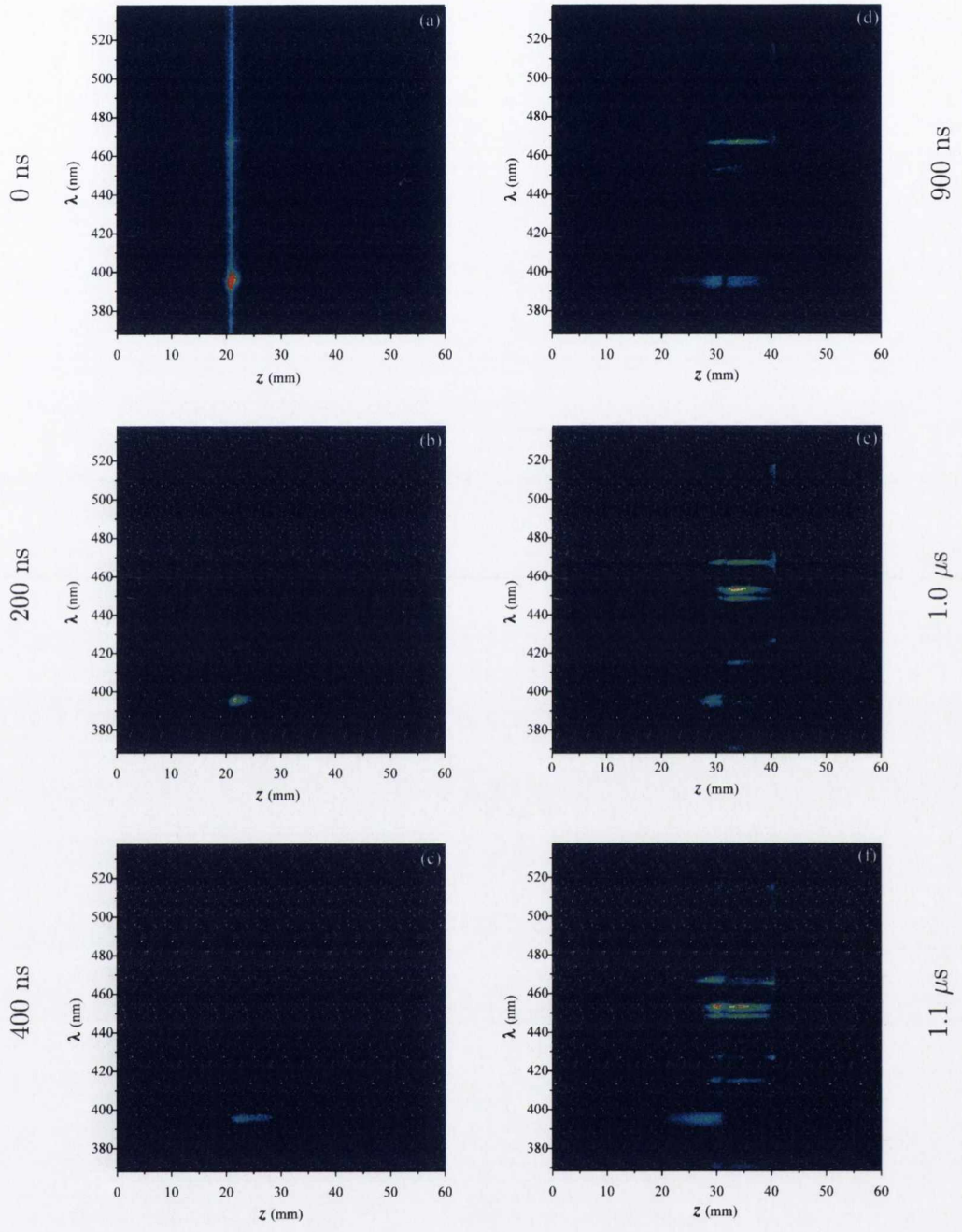

Figure 5.10: Images of the emission lines from the laser ablation plasma (a-c), and 400 volt Z-pinch plasma (d-f) at various time delays after the laser pulse. (a) 0; (b) 200 ns; (c) 400 ns; (d) 900 ns; (e) 1 μs; (f) 1.1 μs. Gate time $\Delta\tau$ = 50ns.

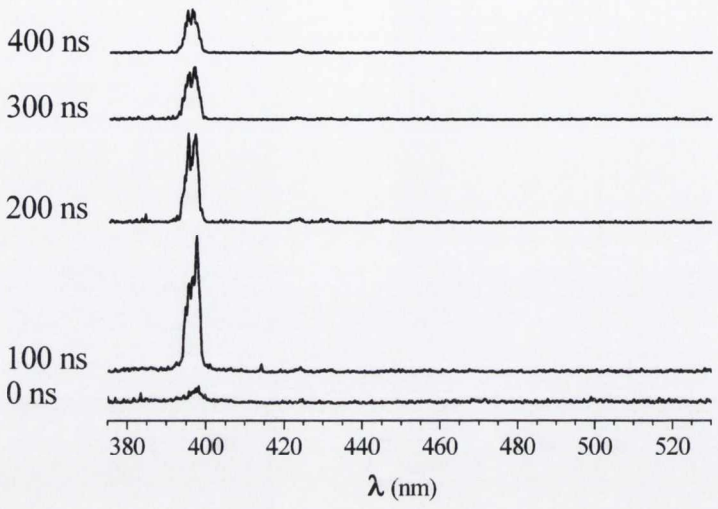

Figure 5.11: Time resolved spectra at Al target (3 mm)

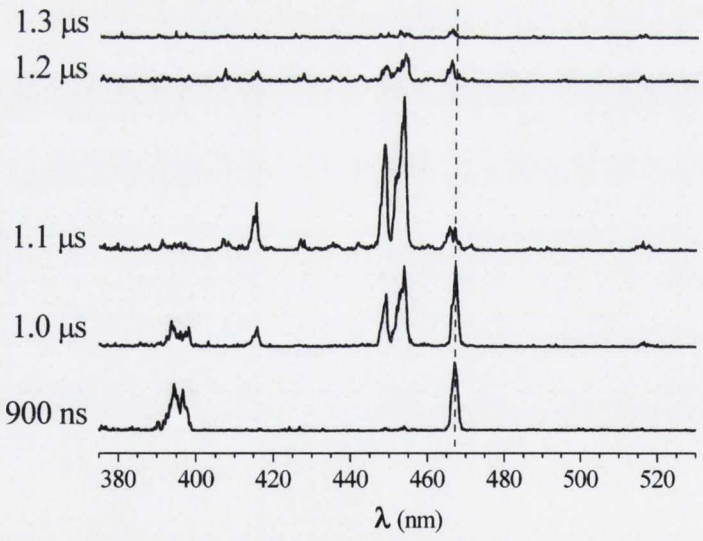

Figure 5.12: Time resolved spectra at centre of discharge cell

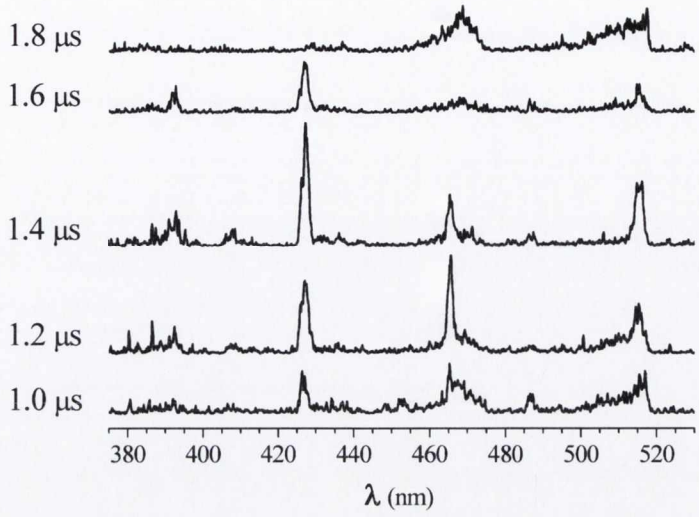

Figure 5.13: Time resolved spectra at Cu anode

Looking at the plots, Fig. 5.11 shows the temporal evolution of the initial LPP as it crosses the 3 mm mark where the lineout was taken. The only line observed is that reported previously, pertaining to the Al I doublet at 394/396 nm. Figure 5.12, on the other hand, shows the emission at the centre of the discharge cell as current first flows through the plasma; the first line at 900 ns shows both the aforementioned Al I doublet as well as the 466 nm Al II line. As time progresses further, the relative irradiance of the Al I and II lines decreases with respect to the Al III lines at 414, 448, 452 nm. The dotted line is drawn marking the 466 nm line, and as as the image shows, the 466 nm spectral line seems to shift to a shorter wavelength at later times; this is actually the appearance of the 465 Cu I line, which is shown to be very intense in Fig. 5.13. In addition to the Cu I 465 nm line, other Cu I lines also appear at 427 nm and 515 nm, between 1.2 and 1.4 μs. Indeed, it seems material is eroded from the Cu anode at later times, following the initial Al plasma being heated as it traverses the cell; a process lasting up to $\sim$1.5 μs (see Fig. 5.3(a)). It should also be noted that the 465 and 515 nm Cu lines appear to be strongly broadened both at 1 μs and 1.8 μs.

Figure 5.14 shows fits of two of the spectra in Fig. 5.11; 200 ns and 400 ns, using

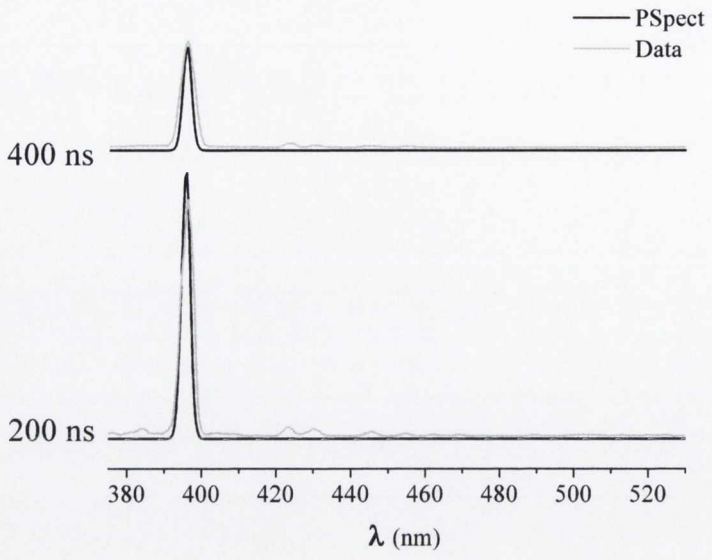

Figure 5.14: PrismSPECT fits for temperature estimation of LPP plasma at $z = 3$ mm from target, for two time delays: **200 ns**: $T_e = 0.85$ eV, $n_i = 5.3 \times 10^{15}$ cm^{-3}, $y_p = 2$ mm; **400 ns**: $T_e = 0.5$ eV, $n_i = 5 \times 10^{14}$ cm^{-3}, $y_p = 3$ mm.

PrismSPECT. As mentioned previously, the software allows the selection of parameters such as ion density, electron temperature and plasma thickness when performing simulations. Therefore, to find the temperature at a specific time delay and distance, the ICCD images were used as a guide for the transverse thickness y_p, whilst the self-similar Langmuir probe signals were used to obtain a density estimate; i.e. only T_e was a free parameter in these fits. Figure 5.15 shows a lineout taken at roughly 1.2 cm from the target, at the inner edge of the cell, thus showing the spectrum of the collimated plasma around the time the discharge begins.

This same fitting technique was also used for the plasma within the cell after the discharge onset, and the results are shown in Fig. 5.16 (cf. 5.12). The parameters used in these fits are shown in Table 5.1.

Note that for the spectrum shown in Fig. 5.16(b) at 1 μs there are two lines applied to the fitting, one having the Al II line at 466 nm and the other having the Al III lines at 414, 448 and 452 nm. These are shown in Table 5.1 as highlighted rows. Also note that the fits for each time delay were done for a collapsing column radius, thus, the plasma thickness values were for column diameters of 3, 2 and 1 mm for

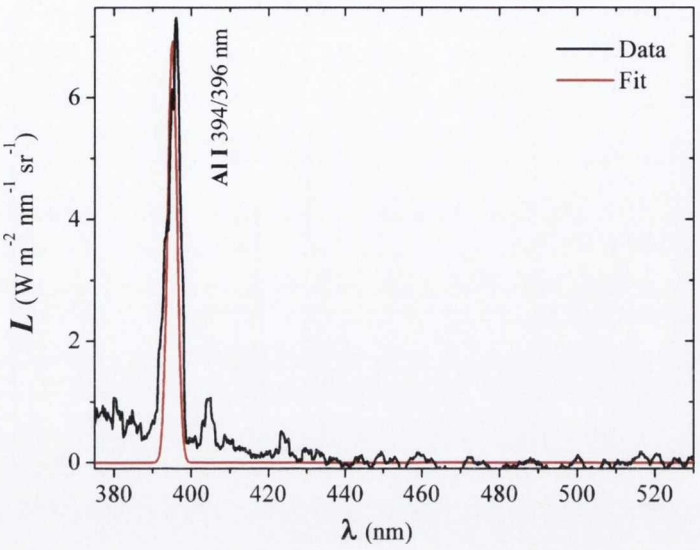

Figure 5.15: PrismSPECT fits for temperature estimation of LPP plasma at $z = 1.2$ cm from target: $T_e = 0.35$ eV, $n_i = 6.5 \times 10^{13}$ cm^{-3}, $y_p = 3$ mm, $\bar{Z} = 0.6$.

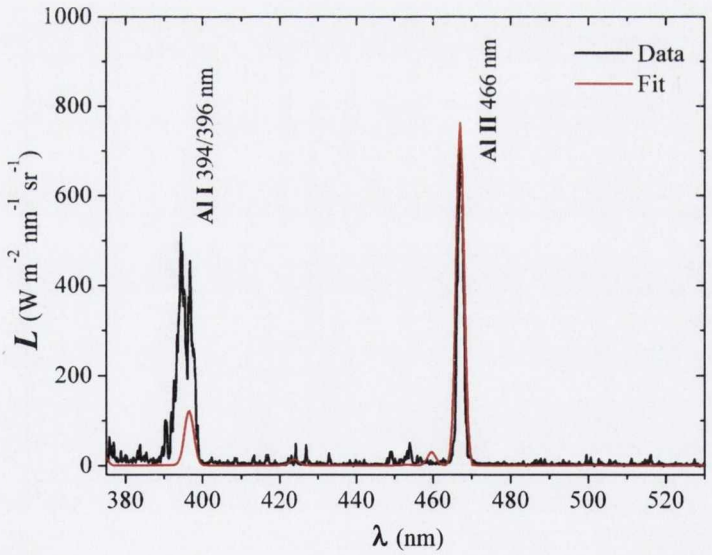

Figure 5.16: PrismSPECT fits of plasma emission inside discharge cell (Fig. 5.12) at Δt =900 ns time delay. (Fitting parameters in Table 5.1)

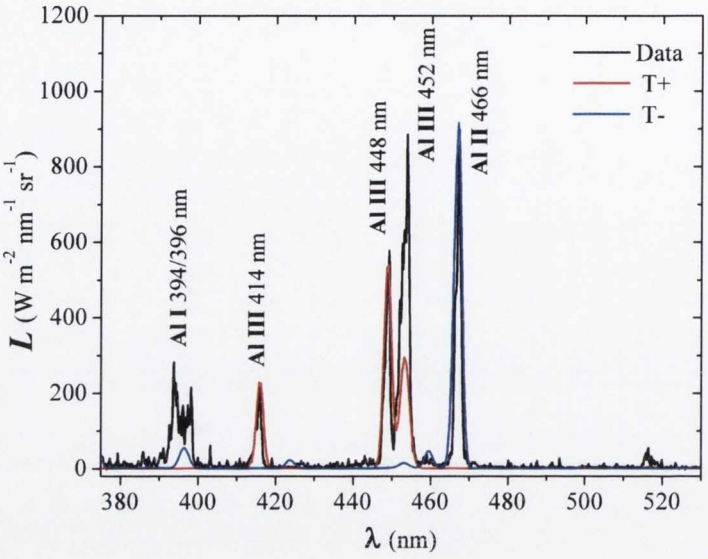

Figure 5.17: PrismSPECT fits of plasma emission inside discharge cell (Fig. 5.12) at Δt =1.0 μs time delay (dual fit T+ and T-). (Fitting parameters in Table 5.1)

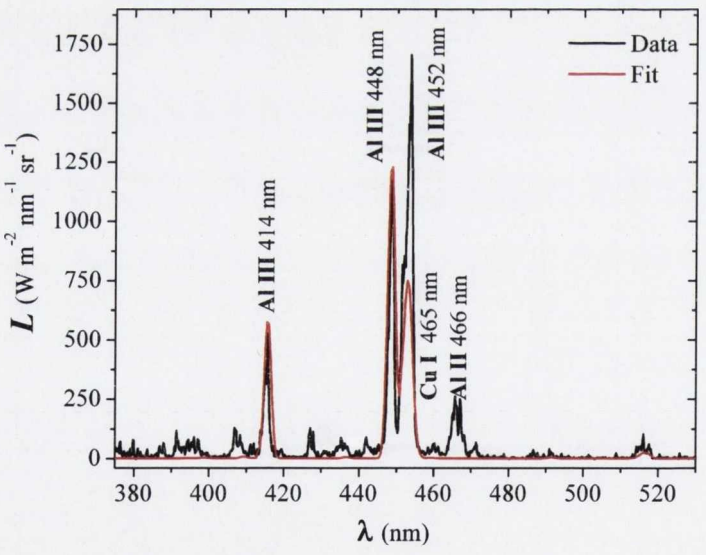

Figure 5.18: PrismSPECT fits of plasma emission inside discharge cell (Fig. 5.12) at Δt =1.1 μs time delay. (Fitting parameters in Table 5.1)

delays of 0.9, 1.0 and 1.1 μs respectively. The electron temperature is also observed to increase as time progresses. As shown in Fig. 5.15(b), the initial LPP has an electron temperature of 0.3 eV as it enters the cell, yet as the discharge begins, this temperature is driven up to 1.2 eV at 900 ns, progressing to 2.2 eV at 1.1 μs. The ion density also increases from $n_i = 5.0 \times 10^{13}\ cm^{-3}$ inside the cell at 0 V, to above 10^{15} cm^{-3}. Note that an attempt to fit the spectra using the initial density gave poor results, therefore, n_i had to be increased almost two orders of magnitude in order to fit the spectra during the discharge. This will be discussed further in the concluding remarks.

Δt (μs)	y_p (mm)	n_i ($\times 10^{15}\ cm^{-3}$)	T_e (eV)	n_e* ($\times 10^{15}\ cm^{-3}$)	$\bar{Z}$*
0.9	3.0	3.2	1.2	4.3	1.4
1.0 (T-)	2.0	3.4	1.3	6.3	1.6
1.0 (T+)	2.0	0.9	2.0	2.6	2.7
1.1	1.0	2.7	2.2	7.3	2.7

Table 5.1: Fitting parameters for PrismSPECT simulations shown in Fig. 5.16 (400 V discharge). Δt- time delay; y_p- plasma thickness; n_i- ion density; T_e- electron temperature; n_e- electron density; $\bar{Z}$- mean ionisation. * Result from simulation.

It is worth mentioning the spectra emitted from the anode in Fig. 5.13. The transitions from the lines observed are similar to those reported in the conical nozzle section, and as such, proved difficult to simulate in PrismSPECT. It is notable, however, that the surface of the anode shows higher emission than the plasma inside the cell when observing the ICCD images. The spectra, however, shows the lines inside the cell as being much more intense than the emission from the anode. It is possible that the highly broadened lines on the anode surface contribute to a quasi-continuum emission; being distributed over a larger spectral range, the line radiance will seem smaller.

5.3 Z-Pinch Analysis

The above images and spectra describe the dynamics of the plasma column as it enters the discharge cell, as well as the first moments of radial collapse. Using the equation based on the snowplow model, as discussed in Section 1.4.2, the time of radial collapse is predicted by:

$$\tau_{imp}^{t} = \left(\frac{\rho_0}{\mu_0}\right)^{1/4} \left(\frac{2R_0^2}{dI/dt}\right)^{1/2} \tag{5.2}$$

Based on the observations in previous sections, the mass density ρ_0[1] and initial radius R_0 are taken from the values at 900 ns (Table 5.1). The rate of current rise, on the other hand, is based on the signal recorded by the Rogowski coil. Equation 5.2 gives, therefore:

$$\tau_{imp}^{t} = \left(\frac{1.4 \times 10^{-4}}{12.5 \times 10^{-7}}\right)^{1/4} \left(\frac{2(1.5 \times 10^{-3})^2}{3.5 \times 10^{9}}\right)^{1/2} = 120 \ ns$$

For the minimum pinch radius R_{min} one may turn to Potter's thermodynamic treatment which predicts this value based on the relation: $R_{min} = R_0 \left(\gamma/\gamma - 1\right)^{\gamma/\gamma - 1} = 0.38 R_0$ for $\gamma = 5/3$. This means the final pinch radius will be:

$$R_0 = 0.38(1.5 \ mm) = 0.57 \ mm$$

Potter's analysis also includes a final pinch temperature and density, based on the following relations:

$$T_{max} = 0.032 \frac{\mu_0 I^2}{k n_i R_0^2} = 67 \ eV$$

$$\rho_{max} = 16.4 \rho_0 = 5 \times 10^{16} \ cm^{-3},$$

[1] $n_i = 3.2 \times 10^{15}$ cm^{-3}

however, these numbers do not appear to agree with the values obtained by spectroscopic means.

5.4 Discussion

Initial laser plasma conditions were estimated using Langmuir probe signals. By applying self-similarity transforms, the total ion densities and ion line densities were estimated for a range of time delays and distances, allowing an approximate prediction of these values in the area of the cell aperture and interior.

The incoming aluminium plasma entering the discharge cell is observed to increase significantly in temperature. Using the ion probe density estimates, spectral line fits using the software PrismSPECT show that at the time the discharge begins (~900 ns), the electron temperature has an initial value of 0.35 eV. This temperature increases to 1.9 eV with the onset of the discharge, reaching a maximum of 2.2 eV at the time the magnetic instability occurs (1.1 μs). The rise in temperature involves an increase in ionisation as well, going from a partially ionised plasma having a mean value of 0.6 to an almost triply-ionised plasma with a mean value of 2.7. This is evident with the appearance of Al II and Al III emission lines in the spectra as the discharge evolves.

When no discharge is present, self-similar analysis is in good agreement with software simulations. However, for the discharge the software did not match the density results from the self-similar predictions. In first instance, as the laser produced plasma arrives at the cell and the discharge ensues, no significant increase in density would be expected, however, when comparing the density at Δt =900 ns delay with and without a discharge, the densities required to match the experimental spectra using the software were 3.2×10^{15} cm^3 (400 V) and 6.5×10^{13} cm^3 (0 V). It is not understood why this occurs. These density values will also reflect on the Z-pinch estimates discussed below.

Multiple spectrum fits, such as those observed in Fig. 5.16(b), seem to suggest an

inhomogeneous plasma. Indeed, as seen in Table 5.1, singly-ionised lines were fit using low temperature and high density values, which were different to those for doubly-ionised lines, having relatively lower density but higher temperature. This inhomogeneity is reported in the literature, where the collapsing plasma column is shown to increase in temperature and decrease in density as the radius becomes smaller [46]. This model therefore suggests that the plasma may have a hot, tenuous core with a colder, more dense exterior shell.

The final pinch radius predicted by the slug model is in good agreement with the column width observed in the ICCD images. This shows a radial contraction from 1.5 mm to ~0.5 mm.

There is relatively good agreement with the time to pinch, at τ= 120 ns. However, this value is proportional to the ion density and is based on the assumption that $n_i = 3.2 \times 10^{15}$ cm^{-3}. As mentioned above, it is not clear if this is the correct density value (as estimated by the spectroscopy software). The other possibility arises when taking $n_i = 6.5 \times 10^{13}$ cm^{-3} which is the value predicted by Langmuir probe measurements, which results in an implosion time of: τ= 88 ns.

Chapter 6

Conclusions and Future Work

A novel technique for laser plasma characterisation was used throughout this work. By exploiting the self-similar character of plume expansion, Langmuir probe signals were used to infer the ion density/line density profiles at changing distances from the ablated target.

Plume expansion dynamics was successfully modified using both an open-ended and a conical collar. A variety of methods, including Langmuir probe, spectroscopy, energy spectrum analysis and film deposition were used to demonstrate these effects.

By placing a cylindrical or conical collar around the ablated target, significant increases in ion flux and material deposition were observed. In the open-ended case, material copper films deposited on glass substrates showed a 2-fold increase in film thickness. On the other hand, by using a conical collar of known expansion ratio (the ratio of the cone throat and aperture), Langmuir probe measurements show ion flux was observed to increase considerably. The cone expansion ratio used herein was 1/10, resulting in a three-fold increase in density.

The density increase observed with the conical collar is further enhanced with a fast, low-inductance discharge. Ion flux was observed to increase by a factor of 12 at -800 V, an effect likely due to the combination of a reducing cross section, enhanced material erosion during the vacuum arc and electron impact ionisation within the cell.

Coaxial electric discharges in an open-ended configuration showed considerable increase in ion flux. Additionally, the distribution of ion kinetic energies is increased significantly, as are the electron temperature and overall ionization. Film thickness measurements suggest an increase in deposition rate with voltage, however, sputtering is evident when certain discharge voltages and polarities are used.

It was observed that ion flux increases with discharge voltage in most cases, however, there were certain experiments where the highest discharge currents showed a very low flux. The possibility of an MHD focusing effect is discussed as the source of this ion probe signal variation.

The Z-pinch effect was observed by discharging a fast electric pulse through a collimated LPP. Within a time of ~200 ns the original plasma column is observed to reduce in radius and subsequently develop an MHD instability. Temperature measurements of the inner collapsing column were estimated by spectroscopic measurements, as well as by the collisional-radiative simulation software PrismSPECT. Multiple temperature and density fits for a single spectrum indicate the an inhomogeneous plasma during the contraction phase, as predicted by the slug model theory of D. Potter [46].

Future Work

One of the main efforts in this work, both in the open-ended collar and in the collimated plasma, was to obtain a Z-pinch. In the former case, it was determined that the current density within the plasma was not high enough for significant compression, therefore leading to the design of the collimated plasma experiment. Although successful in producing radial compression and magnetohydrodynamic instability, it was not sufficient to produce the Z-pinches capable of generating highly energetic photons. Therefore, the following is suggested:

1. Lower inductance. Although the inductance in the circuit used was low, there is still room to improve the circuit in order to reduce it further. By completely

eliminating the current loop between the capacitor and current delivery to the plasma, estimates show the inductance can be reduced by a factor of two or three. By reducing the inductance, higher peak currents can be achieved whilst reducing the return-current oscillations.

2. Efficient discharge timing/slower plasma. It was noted that the plasma propagating into the discharge cell was piling up on the anode. Even though this setup was timed to discharge when the most dense part of the plume is in the cell, this problem still persists due to a rapidly-propagating plume. A means of slowing down the ions is being investigated, whereby colliding two laser produced plasmas expanding towards each other could cause the plumes to slow down [74]. An adequately timed circuit should be used as well.

3. Higher voltage/current. The energy delivered to the plasma can be increased significantly by raising the discharge voltage. Increased current will result in higher magnetic fields; meaning faster radial compression and higher axial temperature.

4. Improved photon detection. The capability of detecting energetic photons in the deep UV and extreme UV will be necessary. This may imply collaboration with the Atomic and Molecular Physics group in UCD, who have the necessary spectrometers and detectors capable of observing these wavelength regimes.

Laser produced plasmas have a well defined and characterised profile, and the limitations of deposition rate related to laser energy, distance, etc are well known. It would be of interest to further explore other collar geometries, since depositions seem to benefit from placing a collar or cone to manipulate the expanding plasma. Although high currents seem to generate undesirable fast ions, low or null currents could be used in conjunction with a collar to manipulate the plasma hydrodynamically. The main problem to address would be that of target erosion and pitting. Since the setup used herein implied repeated laser pulses on the same spot, some form of target rotation or translation would need to be implemented.

References

[1] R. L. Boxman, S. Goldsmith, and A. Greenwood. Twenty-five years of progress in vacuum arc research and utilization. *Plasma Science, IEEE Transactions on*, 25(6):1174–1186, 1997. 0093-3813.

[2] Anand Moorti, Bobbili Sanyasi Rao, Brasad Anant Naik, Parshotam Dass Gupta, Igor Vladimirovich Romanov, Yuriy Vasilievich Korobkin, and Alexander Alexandrovich Rupasov. Cathode plasma jet pinching and intense x-ray emission in a moderate-current laser-triggered vacuum discharge. *IEEE Transactions on Plasma Science*, 34:2419–2425, 2006.

[3] M. E. Foord, Y. Maron, G. Davara, L. Gregorian, and A. Fisher. Particle velocity distributions and ionization processes in gas-puff z pinches. *Physical Review Letters*, 72(24), 1994.

[4] Panel on the Physics of Plasma and Fluids. *Plasmas and Fluids.* Physics through the 90's. National Academies Press, 1986.

[5] A. Cummings, G. O'Sullivan, P. Dunne, E. Sokell, N. Murphy, J. White, P.Hayden, P. Sheridan, M. Lysaght, and F. O'Reilly. A spatio-temporal study of variable composition laser-produced sn plasmas. *Journal of Physics D: Applied Physics*, 39:73, 2006.

[6] T. Krucken, K. Bergmann, L. Juschkin, and R. Lebert. Fundamentals and limits for the euv emission of pinch plasma sources for euv lithography. *Journal of Physics D: Applied Physics*, 37:3213–3224, 2004.

[7] E. Sterling, C. Pagano, and J. Lunney. Influence of fast electrical discharge on expansion of laser produced plasma. *Applied Physics A: Materials Science & Processing*, 92(4):1031–1035, September 2008.

[8] A. M. Fox. *Optical Properties of Solids.* Oxford Master Series in Condensed Matter Physics. Oxford University Press, 2001.

[9] John D. Jackson. *Classical Electrodynamics.* John Wiley & Sons, 1999.

[10] Terry M. Tritt. *Thermal Conductivity: Theory, Properties and Applications.* Springer, 2005.

[11] B. Chichkov, C. Momma, S. Nolte, F. von Alvensleben, and A. Tünnermann. Femtosecond, picosecond and nanosecond laser ablation of solids. *Applied Physics A*, 63:109–115, 1996.

[12] S. Amoruso, R. Bruzzese, N. Spinelli, and R. Velotta. Characterization of laser-ablation plasmas. *Journal of Physics B: Atomic, Molecular and Optical Physics*, 32:R131, 1999.

[13] A. M. Prokhorov, V. I. Konov, I. Ursu, and I. N. Mihailescu. *Laser Heating of Metals.* Adam Hilger, Bristol, 1990.

[14] D. B. Chrisey and G. K. Hubler. *Pulsed Laser Deposition of Thin Films.* John Wiley and Sons, New York, 1994.

[15] R. Kelly, A. Miotello, A. Mele, and G. A. Giardini. *Laser Ablation and Desorption.* Academic Press, 1998.

[16] D. Bauerle. *Laser Processing and Chemistry.* Springer-Verlag, Heidelberg, 3rd edition, 2000.

[17] S. I. Anisimov, D. Bauerle, and B. S. Lukyanchuk. Gas dynamics and thin film deposition of materials. *Physical Review B*, 48:16, 1993.

[18] S. I. Anisimov, B. S. Luk'yanchuk, and A. Luches. An analytical model for three-dimensional laser plume expansion into vacuum in hydrodynamic regime. *Applied Surface Science*, pages 24–32, 1996.

[19] Tue N. Hansen. *Ion outflow and soft X-ray radiation from a micro capillary discharge.* PhD thesis, Trinity College Dublin, 2001.

[20] J. Schou, S. Amoruso, and J.G. Lunney. *Laser Ablation and its Applications.* Springer, 2007.

[21] C. Sánchez Aké, H. Sobral, E. Sterling, and M. Villagrán-Muniz. Time of flight of dual-laser ablation carbon plasmas by optical emission spectroscopy. *Applied Physics A: Materials Science & Processing*, 79:1345–1347, 2004.

[22] A. P. McKiernan and J. P. Mosnier. Study of expansion of laser ablation plumes of ga and gan in various n2 atmospheres using stigmatic emission spectroscopy. *Applied Surface Science*, 197-198:325–330, 2002.

[23] A. Thorne, U. Litzen, and S. Johansson. *Spectrophysics.* Springer-Verlag, Heidelberg, 1999.

[24] Y. B. Zel'dovich and Y. P. Raizer. *Physics of Shock Waves and High-Temperature Hydrodynamic Phenomena.* Dover, Mineola, 2002.

[25] R. W. P. McWhirter. *Plasma Diagnostic Techniques*, volume 21 of *Pure and Applied Physics.* Academic Press, 1965.

[26] Takashi Fujimoto. *Plasma Spectroscopy.* Oxford University Press, 2004.

[27] William T. Silfvast. *Laser Fundamentals.* Cambridge University Press, New York, 2nd edition, 2004.

[28] B. Y. Man, Q. L. Dong, A. H. Liu, X. Q. Wei, Q. G. Zhang, J. L. He, and X. T. Wang. Line-broadening analysis of plasma emission produced by laser ablation of metal cu. *Journal of Optics: Pure and Applied Optics*, 6:17–21, 2004.

[29] W. L. Wiese. *Plasma Diagnostic Techniques*, volume 21 of *Pure and Applied Physics*. Academic Press, 1965.

[30] M Ortiz and R Mayo. Measurement of the stark broadening for several lines of singly ionized gold. *Journal of Physics B: Atomic, Molecular and Optical Physics*, 38(22):3953–3961, 2005.

[31] H. R. Griem. *Plasma Spectroscopy*. McGraw-Hill, New York, 1964.

[32] A. Lesage. Experimental stark widths and shifts for spectral lines of neutral and ionized atoms a critical review of selected data for the period 2001-2007. *New Astronomy Reviews*, 52(11-12):471 – 535, 2009.

[33] N. Konjevic and W. L. Wiese. Experimental stark width and shifts for spectral lines of neutral and ionized atoms. *Journal of Physical and Chemical Reference Data*, 19(6), 1990.

[34] H. R. Griem. Stark broadening by electron and ion impacts of na hydrogen lines of large principal quantum number. *Astrophysical Journal*, 148:547, 1967.

[35] R. L. Boxman, D. M. Sanders, and P. J. Martin. *Handbook of Vacuum Arc Science & Technology: Fundamentals and Applications*. William Andrew, Park Ridge, NJ, 1997.

[36] G. A. Mesyats. Ecton mechanism of the vacuum arc cathode spot. *IEEE Transactions in Plasma Science*, 23(No. 6), 1995.

[37] I. Paulus, R. Holmes, and H. Edels. Vacuum arc response to current transients. *Journal of Physics D: Applied Physics*, (1):119, 1972.

[38] I. A. Krinberg and V. L. Paperny. Pinch effect in vacuum arc plasma sources under moderate discharge currents. *Journal of Physics D: Applied Physics*, (6):549, 2002.

[39] J. C. Sherman, R. Webster, J. E. Jenkins, and R. Holmes. Cathode spot motion in high current vacuum arcs on copper electrodes. *Journal of Physics D: Applied Physics*, (6):696, 1975.

[40] H. Craig Miller. Vacuum arc anode phenomena. *Plasma Science, IEEE Transactions on*, 11(2):76–89, 1983. 0093-3813.

[41] Markus J. Aschwanden. *Physics of the solar corona: an introduction.* Springer, 2004.

[42] L. C. Woods. *Physics of Plasmas.* Wiley-VCH, Weinheim, 2004.

[43] Hans Goedbloed and Stefaan Poedts. *Principles of Magnetohydrodynamics.* Cambridge University Press, 2004.

[44] Michael A. Liberman, John S. de Groot, A. Toor, and Rick B. Spielman. *Physics of High-Density Z-Pinch Plasmas.* Springer, 1999.

[45] Nicholas A. Krall and Alvin W. Trivelpeice. *Principles of Plasma Physics.* McGraw-Hill, 1973.

[46] D. Potter. The formation of high-density z-pinches. *Nuclear Fusion*, 18(6):813–823, 1978.

[47] B. Autin, H. Riege, E. Boggasch, K. Frank, L. de Menna, and G. Milano. Z-pinch plasma lens for focusing high-energy particles in accelerator. *IEEE Transactions in Plasma Science*, PS-15(2), 1987.

[48] Michael A. Lieberman and Allan J. Lichtenberg. *Principles of Plasma Discharges and Materials Processing.* John Wiley & Sons, New York, 2006 1994.

[49] A. E. Robson. Anomalous resistivity and the pease-braginski current in a z-pinch. *Physical Review Letters*, 63(26):2816–2818, 1989.

[50] D. A. Gurnett and A. Bhattacharjee. *Introduction to Plasma Physics.* Cambridge University Press, Cambridge, UK, 2005.

[51] Andreas Dinklage, Thomas Klinger, Gerrit Marx, and Lutz Schweikhard. *Plasma physics: confinement, transport and collective effects.* Springer, 2005.

[52] K. U. Riemann. The bohm criterion and sheath formation. *Journal of Physics D: Applied Physics*, 24:493, 1991.

[53] Brendan Doggett and James G. Lunney. Langmuir probe characterization of laser ablation plasmas. *Journal of Applied Physics*, 105:033306, 2009.

[54] Y. Franghiadakis, C. Fotakis, and P. Tzanetakis. Energy distribution of ions produced by excimer-laser ablation of solid and molten targets. *Applied Physics A*, 68:391–397, 1999.

[55] D. A. Ward and J. La T. Exon. Using rogowski coils for transient current measurements. *Engineering Science and Education Journal*, 2(3):105–113, 1993. Excellent introductory to rogowski coils, physics and circuitry inclusive.

[56] P. Hayden, A. Cummings, N. Murphy, G. O'Sullivan, P. Sheridan, J. White, and P. Dunne. 13.5 nm extreme ultraviolet emission from tin based laser produced plasma sources. *J. Appl. Phys*, 99(093302), 2006.

[57] N. Bowering, M. Martins, W. N. Partlo, and I. V. Fomenkov. Extreme ultraviolet emission spectra of highly ionized xenon and their comparison with model calculations. *J. Appl. Phys.*, 95(16), 2004.

[58] E. L. Antonsen, K. C. Thompson, M. R. Hendricks, D. A. Alman, B. E. Jurczyk, and D. N. Ruzic. Ion debris characterization from a z-pinch extreme ultraviolet light source. *Jour. Appl. Phys*, 99(063301), 2006.

[59] P. Gasior, J. Badziak, A. Czarnecka, P. Parys, J. Wolowski, M. Rosinski, M. Rubel, and V. Philipps. Characterization of laser-irradiated co-deposited layers on plasma facing components from a tokamak. *Physica Scripta*, page 99, 2006.

[60] E. de Hoffman and V. Stroobant. *Mass Spectrometry: Principles and Applications.* John Wiley & Sons, 2001.

[61] Aodh O'Connor. *Ion spectroscopy of laser produced plasmas with potential for extreme ultraviolet sources.* PhD thesis, University College Dublin, 2009.

[62] E. H. Eberhardt. Gain model for microchannel plates. *Applied Optics*, 18(9), 1979.

[63] T. Donnelly. *Plume dynamics in nanosecond and femtosecond laser ablation of metals.* PhD thesis, Trinity College Dublin, 2009.

[64] C. Colon, G. Hatem, E. Verdugo, P. Ruiz, and J. Campos. Measurement of the stark broadening and shift parameters for several ultraviolet lines of singly ionized aluminum. *Journal of Applied Physics*, 73(10):4752–4758, 1993.

[65] S. S. Harilal, Beau O'Shay, Mark. S. Tillack, and Manoj V. Mathew. Spectroscopic characterization of laser-induced tin plasma. *Journal of Applied Physics*, 98(1):013306, 2005.

[66] I. Weaver and C. L. S. Lewis. Polar distribution of ablated atomic material during the pulsed laser deposition of cu in vacuum: Dependence on focused laser spot size and power density. *Journal of Applied Physics*, 79:7216, 1996.

[67] P. Sigmund. Theory of sputtering. i. sputtering yield of amorphous and polycrystalline targets. *Physical Review*, 184(2), 1969.

[68] L.S. Dorneles, D. O'Mahony, C.B. Fitzgerald, F. McGee, M. Venkatesan, I. Stanca, J.G. Lunney, and J.M.D. Coey. Structural and compositional analysis of transition-metal-doped zno and gan pld thin films. *Applied Surface Science*, 248(1-4):406 – 410, 2005. 4th International Conference on Photo-Excited Processes and Applications.

[69] I. A. Krinberg. The hollow-charge effect in the cathodic plasma jet under vacuum breakdown. *Journal of Physics D: Applied Physics*, 29:2049–2051, 1996.

[70] S. S. Harilal, C. V. Bindhu, M. S. Tillack, F. Najmabadi, and A. C. Gaeris. Internal structure and expansion dynamics of laser ablation plumes into ambient gases. *J. Appl. Phys.*, 93(5):2380–2388, 2003.

[71] K. Fu, M. Jogwich, M. Knebel, and K. Wiesemann. Atomic transition probabilities and lifetimes for the cu i system. *Atomic and Nuclear Data Tables*, 61:1–30, 1995.

[72] J. Thomas Knudtson, William B. Green, and David G. Sutton. The uv-visible spectroscopy of laser-produced aluminum plasmas. *Journal of Applied Physics*, 61:4771, 1987.

[73] R. C. Dykhuizen and M. F. Smith. Gas dynamic principles of cold spray. *Journal of Thermal Spray Technology*, 7:205–212, 1998.

[74] P. Hough, McLoughlin C, Kelly T J, Hayden P, Harilal S, Mosnier J P, and Costello J T. Colliding laser produced plasmas as novel sources: Optical diagnostics. *Journal of Physics: Conference Series*, 194(6):062003, 2009.